TURBULENT MIXED CONVECTION FLOW IN RECTANGULAR ENCLOSURES

A NUMERICAL INVESTIGATION OF TURBULENT MIXED CONVECTION FLOW IN RECTANGULAR ENCLOSURES

By

J. ADAM LOGAN, B.ENG.

A Thesis
Submitted to the School of Graduate Studies in Partial Fulfilment of the Requirements for the Degree
Masters of Engineering

McMaster University

(c) Copyright by J. Adam Logan, September 1996

MASTERS OF ENGINEERING (1996)

McMASTER UNIVERSITY Hamilton, Ontario

(Mechanical Engineering)

A Numerical Investigation of Turbulent Mixed Convection

Flow In Rectangular Enclosures

AUTHOR:

TITLE:

J. Adam Logan, B.Eng. (McMaster University)

SUPERVISORS:

Dr. M. Shoukri

Dr. P. Wood

NUMBER OF PAGES:

xii, 116

ABSTRACT

This study involves a numerical investigation of turbulent, mixed convection flow within a rectangular enclosure. Previous numerical and experimental research conducted at McMaster University, Hamilton (Canada) found that the influence of buoyancy was generally overpredicted when the standard k-ɛ low-Reynolds number turbulence model was employed. The main purpose of this study is to determine the effect of representing the turbulent heat flux components using the more physically realistic Algebraic Heat Flux Model (AFM). The AFM model is shown to have a significant effect on the turbulence parameters involved leading to even higher rates of heat transfer and buoyant influence than the standard eddy viscosity representation for all test cases.

As a secondary study, the sensitivity of the predicted results to the choice of inlet turbulence conditions is considered. The results show that the choice of inlet conditions can have a significant effect on the predicted flow field and therefore must be accurately selected when dealing with this type of flow.

ACKNOWLEDGEMENTS

I would like to express sincere thanks to the following individuals who have contributed to the successful completion of this study:

- Dr. M. Shoukri for providing me with several great opportunities throughout my university career as well as supervising and supporting this project
- Dr. P. Wood for his supervision, support, and considerable insight
- Dr. G. Nurnberg for his instruction and for patiently answering all of my questions during the past three years
- Dr. R.L. Judd and Dr. G.F. Round for serving on my review committee
- Miss Heather Thompson for being Heather Thompson
- Finally, to Mr. Bob Dylan and Mr. Jack Kerouac for their unending words of encouragement

TABLE OF CONTENTS

				Page
ABS	TRACT	•		iii
ACK	NOWL	EDGEM	ENTS	iv
TAB	LE OF	CONTE	NTS	v
NON	MENCL.	ATURE		viii
LIST	OF FIG	GURES		x
LIST	OF TA	BLES		xii
1	INTR	ODUC	ΓΙΟΝ	1
	1.1			1
	1.2	Object		2
	1.3			2
2	LITE	RATUR	E SURVEY	4
	2.1	Turbu	lence Modelling	4
		2.1.1	Time-Averaged Governing Equations	4
		2.1.2	Effective Viscosity Concept	6
			Zero-Equation Models	8
			One-Equation Models	8
			Two-Equation Models	10
		2.1.6	Near-Wall and Low Reynolds Number Flows	12
		2.1.7	Second-Order Differential Reynolds Stress/Flux Models	13
		2,1.8	Algebraic Stress/Flux Models	16
	2.2	Previo	ous Numerical Studies	18
		2.2.1	Two-Equation Models	18
		2.2.2	Differential and Algebraic Stress/Flux Models	20
	2.3		em History	23
			Experimental Results	26
			Numerical Desults	27

TABLE OF CONTENTS (continued)

			Page	
3		THEMATICAL FORMULATION	38	
	3.1	Introduction	38	
	3.2	Governing Equations	38	
		3.2.1 Dimensional Governing Equations	38	
		3.2.2 Dimensionless Variables	41	
		3.2.3 Dimensionless Governing Equations	42	
	3.3	•	45	
	3.4	Boundary Conditions	47	
		3.4.1 Velocity and Temperature Boundary Conditions	47	
		3.4.2 Turbulence Boundary Conditions	48	
4	NUM	MERICAL FORMULATION	51	
	4.1	Introduction	51	
	4.2	Solution Strategy	51	
		4.2.1 General Conservation Form	51	
		4.2.2 Discretization of the Governing Equations	53	
		4.2.3 Solution Algorithm	54	
	4.3	Algebraic Heat Flux Model	54	
		4.3.1 Explicit Algebraic Heat Flux Calculation	54	
		4.3.2 Fluctuating Temperature Variance	55	
•		4.3.3 Modified Energy Equation Formulation	56	
5	RES	ULTS AND DISCUSSION	58	
	5.1	Introduction		
	5.2	Inlet Viscosity Study	58	
		5.2.1 Case 1	59	
		5.2.2 Case 2	60	
		5.2.3 Case 3	68	
		5.2.4 Case 4	73	
		5.2.5 Inlet Viscosity Study Summary	7 9	
	5.3	Algebraic Flux Model (AFM) Study	7 9	
		5.3.1 Case 2	81	
		5.3.2 Case 3	86	
		5.3.3 Case 4	92	
		5.3.4 AFM Study Summary	92	
	5.4	Final Results	97	
		5.4.1 Case 1	98	
		5.4.2 Case 2	100	
		5.4.3 Case 3	103	
		5.4.4 Case 4	106	
		5.4.5 Final Results Summary	109	
6	CON	ICLUSIONS AND RECOMMENDATIONS	110	
		Purnose	110	

TABLE OF CONTENTS (continued)

		Page
6.2	Conclusions	110
6.3	Recommendations	112
REFEREN	CES	114

NOMENCLATURE

а	Inlet ratio (D/H) of the cavity
C	Empirical turbulence model constant (see Table 2.1)
D	Inlet height (see Figure 2.1)
f	Low Reynolds number model damping function (see Equation 3.34)
g	acceleration due to gravity
G	Generation of turbulence
Gr	Grashof number
\mathbf{H}	Cavity height (see Figure 2.1)
k	Dimensional turbulence kinetic energy
1	Mixing length
L	Turbulence length scale
p	Dimensional fluid pressure
P	Dimensionless fluid pressure
Pr	Prandtl number
R	Time scale ratio (see Equation 2.27)
Re	Reynolds number
Ri	Richardson number (see Equation 2.30)
S	Source term
t	Fluctuating temperature
T	Dimensional fluid temperature
u	Velocity component in the x - direction
U	Dimensionless u - velocity
v	Velocity component in the y - direction
\mathbf{v}	Dimensionless v - velocity
W	Cavity width (see Figure 2.1)
x	Dimensional horizontal component
X	Dimensionless horizontal component
y	Dimensional vertical component
Y	Dimensionless vertical component

Greek Variables

α Thermal diffusivity of the fluid

NOMENCLATURE (continued)

- β Coefficient of thermal expansion of the fluid
- Γ Eddy diffusivity of heat (see Equation 2.8)
- δ Kronecker delta
- ε Dimensional rate of dissipation of turbulent kinetic energy
- η AFM constant
- θ Dimensionless temperature
- v Kinematic viscosity
- ξ AFM constant
- ρ Fluid density
- σ Turbulent Prandtl-Schmidt number (see Table 2.1)
- τ Time, Shear stress (see Equation 2.5)
- φ General flow variable (see Equation 2.1)
- Ψ Turbulent intensity (see Equation 3.37)

Subscripts

AFM Algebraic Flux Model

C Constant part

in Inlet boundary condition

jet Inlet jet
l Laminar

out Outlet boundary condition

P Variable part

pen Penetration location

R Reference value

sep Separation location

SGD Simple Gradient Diffusion

t Turbulent

w Wall boundary condition

Superscripts

- Average quantity
- Fluctuating quantity
- Dimensionless quantity

LIST OF FIGURES

		Page
2.1	Problem Specification	25
2.2	Case 1 - LDA Results	28
2.3	Case 2 - LDA Results	29
2.4	Case 3 - LDA Results	30
2.5	Case 4 - LDA Results	31
2.6	Case 1 - Low Reynolds Number Turbulence Model Predictions	33
2.7	Case 2 - Low Reynolds Number Turbulence Model Predictions	34
2.8	Case 3 - Low Reynolds Number Turbulence Model Predictions	35
2.9	Case 4 - Low Reynolds Number Turbulence Model Predictions	36
5.1	Inlet Viscosity Study (Case 1): Streamlines	61
5.2	Inlet Viscosity Study (Case 1): Turbulent Viscosity Contours	61
5.3	Inlet Viscosity Study (Case 1): Turbulent Viscosity Profile (Y=0.5)	62
5.4	Inlet Viscosity Study (Case 2): Streamlines	64
5.5	Inlet Viscosity Study (Case 2): Turbulent Viscosity Contours	65
5.6	Inlet Viscosity Study (Case 2): Turbulent Viscosity Profile (Y=0.5)	66
5.7	Inlet Viscosity Study (Case 2): Temperature Profiles (Y=0.5)	67
5.8	Inlet Viscosity Study (Case 3): Streamlines	69
5.9	Inlet Viscosity Study (Case 3): Turbulent Viscosity Contours	70
5.10	Inlet Viscosity Study (Case 3): Temperature Profile (Y=0.5)	7 1
5.11	Inlet Viscosity Study (Case 3): Turbulent Viscosity Profile (Y=0.5)	72
5.12	Inlet Viscosity Study (Case 4): Streamlines	74
5.13	Inlet Viscosity Study (Case 4): Turbulent Viscosity Contours	75
5.14	Inlet Viscosity Study (Case 4): Temperature Profiles (Y=0.5)	76
5.15	Inlet Viscosity Study (Case 4): Turbulent Viscosity Profile (Y=0.5)	77
5.16	AFM Study (Case 2): Streamlines	82
5.17	AFM Study (Case 2): Turbulent Heat Flux Profiles (Y=0.5)	83
5.18	AFM Study (Case 2): Temperature Profiles (Y=0.5)	84
5.19	AFM Study (Case 2): Turbulent Viscosity Profiles (Y=0.5)	85
5.20	AFM Study (Case 3): Streamlines	87
5.21	AFM Study (Case 3): Turbulent Heat Flux Profiles (Y=0.5)	88
5.22	AFM Study (Case 3): Temperature Profiles (Y=0.5)	89

LIST OF FIGURES (Continued)

		Page
5.23	AFM Study (Case 3): Turbulent Viscosity Profiles (Y=0.5)	90
5.24	AFM Study (Case 4): Streamlines	93
5.25	AFM Study (Case 4): Turbulent Heat Flux Profiles (Y=0.5)	94
5.26	AFM Study (Case 4): Dimensionless Temperature Profiles (Y=0.5)	95
5.27	AFM Study (Case 4): Turbulent Viscosity Profiles (Y=0.5)	96
5.28	Final Results (Case 1): Streamline Comparison	99
5.29	Final Results (Case 1): Predicted Turbulent Viscosity Contours	99
5.30	Final Results (Case 2): Streamline Comparison	101
5.31	Final Results (Case 2): Predicted Turbulent Viscosity Contours	101
5.32	Final Results (Case 2): Nusselt Number Comparison	102
5.33	Final Results (Case 3): Streamline Comparison	104
5.34	Final Results (Case 3): Predicted Turbulent Viscosity Contours	104
5.35	Final Results (Case 3): Nusselt Number Comparison	105
5.36	Final Results (Case 4): Streamline Comparison	107
5.37	Final Results (Case 4): Predicted Turbulent Viscosity Contours	107
5.38	Final Results (Case 4): Nusselt Number Comparison	108

LIST OF TABLES

		Page
2.1	k-E Model Constants	12
2.2	Summary of Test Cases	24
2.3	Separation Locations	32
4.1	Governing Equations in General Form	52
4.2	Dimensionless Temperature Variance in General Form	55
5.1	Inlet Viscosity Study (Case 1)	60
5.2	Inlet Viscosity Study (Case 2)	63
5.3	Inlet Viscosity Study (Case 3)	68
5.4	Inlet Viscosity Study (Case 4)	78
5.5	AFM Study (Case 2)	81
5.6	AFM Study (Case 3)	91
5.7	Final Results: Inlet Turbulence Conditions	98

CHAPTER ONE

INTRODUCTION

1.1 Background

The development of computational approaches to fluid mechanics and heat and mass transfer has had an immeasurable effect on these fields in recent years. Numerical solutions can now be generated for complicated problems once considered impossible to solve. As a result, the need for elaborate experimentation has been reduced or entirely removed in many instances, translating to savings of time and money.

One of the most difficult problems in computational fluid dynamics (CFD) has been and continues to be the incorporation of turbulent effects within a numerical formulation. Many turbulence models have been proposed, with varying degrees of success associated with each. The most popular turbulence models currently employ a two-equation k- ϵ model based on a simple eddy viscosity/diffusivity hypothesis. Such models have demonstrated an ability to predict the solution to a wide variety of fluid flow problems.

There are, however, certain types of flows which have not been well-predicted by this type of model. Among these are turbulent flows induced by thermal buoyancy. Such flows have many applications within the engineering field including space heating and

cooling, nuclear reactor components, electronic equipment, and solar collectors. Despite the practical importance, many of these problems have not and cannot be successfully solved using the current industrial standard models.

The modelling of the turbulent heat flux components, which is considered by some to be at the root of the problem, has received attention in the recent CFD literature. While some success has been attained, it is clear that more work is required before a suitable model is developed.

1.2 Objective

The present study involves the numerical investigation of turbulent mixed convective flow within an enclosure. The main objective is to determine the effect on the predicted results when an algebraic turbulent heat flux model is incorporated into the governing equations. As a secondary study, the sensitivity of the predicted results to inlet turbulence conditions is also examined. While this topic does not normally receive a great deal of attention, it is believed that this may be an important factor when dealing with this type of flow.

The final results are compared with detailed velocity, temperature, and heat transfer data obtained previously at McMaster University, Hamilton (Canada).

1.3 Outline

The study is comprised of six chapters. The following chapter reviews previous related research in buoyancy-induced flows and turbulence modelling. Chapter Three

details the mathematical formulation of the problem while Chapter Four deals with the numerical approach. Chapter Five presents the results and compares them to previous experimental and numerical values. The final chapter contains conclusions and suggestions for further study.

CHAPTER TWO

LITERATURE SURVEY

This chapter is intended to serve as a concise review of the topics directly related to this study. Other, exhaustive review articles and books on these subjects are referenced where appropriate.

Section 2.1 provides an introduction to turbulence modelling, with the focus on models which are most commonly used today. Section 2.2 contains an examination of previous numerical studies of buoyancy-induced cavity flows. Finally, Section 2.3 describes the particular flow geometry and summarizes the previous results.

2.1 Turbulence Modelling

2.1.1 Time-Averaged Equations

Turbulent flow is governed by the same set of instantaneous conservation equations which govern laminar flow. For the problem considered, these include the continuity equation, the Navier-Stokes equations, and the energy equation. However, due to the small-scale nature of turbulence it is generally impractical to deal with these equations in their instantaneous form. Instead, the instantaneous variables are separated into mean and fluctuating quantities as in Equation (2.1),

$$\phi = \overline{\phi} + \phi' \tag{2.1}$$

where ϕ represents the dependent variables u, v, T, etc. The overbar denotes the time averaged value of the component while the prime refers to the fluctuating value. After substitution into the instantaneous equations and the subsequent averaging of the individual terms, the time-averaged governing equations for turbulent flow are derived.

Continuity

$$\frac{\partial \overline{u_i}}{\partial x_i} = 0 \tag{2.2}$$

Momentum

$$\frac{\partial \overline{u_i}}{\partial \tau} + \overline{u_j} \frac{\partial \overline{u_i}}{\partial x_j} = -\frac{1}{\rho} \frac{\partial \overline{p}}{\partial x_i} + \frac{\partial}{\partial x_j} \left[v_l \frac{\partial \overline{u_i}}{\partial x_j} - \overline{u'_j u'_i} \right] - g_i \beta (\overline{T} - T_R)$$
 (2.3)

Energy

$$\frac{\partial \overline{T}}{\partial \tau} + \overline{u_j} \frac{\partial \overline{T}}{\partial x_j} = \frac{\partial}{\partial x_j} \left[\frac{\mathbf{v}_l}{\mathbf{\sigma}_T} \frac{\partial \overline{T}}{\partial x_j} - \overline{u'_j t'} \right]$$
 (2.4)

It should be noted that the Boussinesq approximation has been introduced to

account for density fluctuations. Thus the influence of variable density appears only in the last term on the right hand side of Equation (2.3). For convenience, the overbars will be dropped from all terms containing only mean quantities from this point on.

The terms involving correlations of fluctuating components make this equation set different from the laminar equation set. Specifically, these include the mean Reynolds stresses and the turbulent heat fluxes. These terms are responsible for the effect of turbulence on the mean flow.

For a two-dimensional flow (i = 1, 2), there are nine unknowns but only four equations. To close this equation set, relationships for the turbulent stress and flux terms must be developed.

2.1.2 Effective Viscosity Concept

Turbulent flows involve rapid mixing and, therefore, increased rates of momentum and heat transfer. One approach then, is to attempt to mimic these turbulent effects through the use of artificial or 'eddy' viscosity and diffusivity coefficients.

Boussinesq proposed this concept in 1877 in analogy to the existing relationship for viscous stresses in laminar flow [1]. Boussinesq suggested that the turbulent stresses could be expressed as,

$$\tau_t = -\overline{u'_i u'_j} = v_t \left(\frac{\partial u_i}{\partial x_j} + \frac{\partial u_j}{\partial x_i} \right) - \frac{2}{3} k \delta_{ij}$$
 (2.5)

where v_t represents the turbulent or 'eddy' viscosity. The turbulence kinetic energy, k,

defined as,

$$k = \frac{1}{2} \left(\overline{u_1'^2} + \overline{u_2'^2} + \overline{u_3'^2} \right) \tag{2.6}$$

is incorporated to insure that the relationship also holds for the normal stresses (where i = j).

In direct analogy to the eddy viscosity concept, the turbulent heat flux is expressed as,

$$\overline{u'_i t'} = -\Gamma \frac{\partial T}{\partial x_i} \tag{2.7}$$

where Γ is the eddy diffusivity of heat. The Reynolds analogy is often used to relate this diffusivity to the eddy viscosity,

$$\Gamma = \frac{v_t}{\sigma_T} \tag{2.8}$$

where $\sigma_{\scriptscriptstyle T}$ is the turbulent Prandtl number.

Equations (2.5) and (2.7) can be used to eliminate the turbulent stresses and heat fluxes from the mean flow equations. It is still necessary to determine the turbulent viscosity at all points in the flow field before the equation set is closed.

Many methods have been proposed for the determination of eddy viscosity within a flow field. In general this quantity can be expressed as the product of a length scale, L, and a velocity scale, V, such that,

$$v_t \propto LV$$
 (2.9)

These scales can be prescribed algebraically based on an *a priori* knowledge of the flow field but it has become popular to use differential relationships which attempt to account for the transport and history of the turbulence. Models of the eddy viscosity type are often characterized by the number of additional differential equations which must be solved to close the equation set.

2.1.3 Zero-Equation Models

The first turbulence model was proposed by Prandtl [1] who related the eddy viscosity to the transverse velocity gradient and a prescribed length scale, l_m , which Prandtl called the mixing length:

$$v_t = l_m^2 \left| \frac{\partial u}{\partial y} \right| \tag{2.10}$$

Despite its simplicity, Prandtl's mixing length model has been applied successfully to many types of flows. The model works very well in situations where a single velocity scale governs the flow and the mixing length, which is related to the size of the largest eddies, can be predicted accurately. This prescription becomes very difficult as the complexity of a problem and the number of relevant length and velocity scales increases.

2.1.4 One-Equation Models

Attempting to account for the transport of turbulence, one-equation models

determine the velocity scale from its own transport equation. The most common velocity scale used is the square root of turbulence kinetic energy, \sqrt{k} . When substituted into Equation (2.9), the Kolmogorov-Prandtl expression [1] results,

$$v_t = C_u^{\prime} \sqrt{k} L \tag{2.11}$$

where C_u' is an empirical constant.

The exact equation for the transport of k can be derived from the Navier-Stokes equations [1],

$$\frac{\partial k}{\partial \tau} + u_i \frac{\partial k}{\partial x_i} = -\frac{\partial}{\partial x_i} \left[\overline{u'_i (\frac{u'_j u'_j}{2} + \underline{p'})} \right] - \overline{u'_i u'_j} \frac{\partial u_i}{\partial x_j} - \beta g_i \overline{u'_i t'} - v_i \overline{\frac{\partial u'_i \partial u'_i}{\partial x_j} \partial x_j}$$
(2.12)

The left hand side of the equation describes the time rate of change and convection of turbulence kinetic energy, while the first term on the right hand side is responsible for the diffusive transport of k due to pressure and velocity fluctuations. Since the diffusion term is a function of unknown correlations this term must be modelled. The second and third terms on the right hand side represent the generation of kinetic energy due to shear and buoyancy respectively. The last term on the right is always negative and thus represents the viscous dissipation of k. This term also requires modelling.

In analogy to the diffusion of temperature and other scalar quantities, the diffusion flux of k is often expressed as [1],

$$\frac{\overline{-u'_{i}\left(\frac{u'_{j}u'_{j}}{2} + \frac{p'}{\rho}\right)} = \frac{v_{t}}{\sigma_{k}} \frac{\partial k}{\partial x_{i}}$$
 (2.13)

where σ_k is an empirical constant.

The dissipation of turbulence kinetic energy, ε , is usually modelled as [1],

$$\varepsilon = v_l \frac{\partial u_i^{\prime} \partial u_i^{\prime}}{\partial x_i \partial x_i^{\prime}} = C_D \frac{k^{3/2}}{L}$$
 (2.14)

following from dimensional arguments employing k and L as the scales for the dissipation of kinetic energy.

The final modelled form of the turbulence kinetic energy equation is,

$$\frac{\partial k}{\partial \tau} + u_i \frac{\partial k}{\partial x_i} = \frac{\partial}{\partial x_i} \left(\frac{v_t}{\sigma_k} \frac{\partial k}{\partial x_i} \right) + v_t \left(\frac{\partial u_i}{\partial x_j} + \frac{\partial u_j}{\partial x_i} \right) \frac{\partial u_i}{\partial x_j} + \beta g_i \frac{v_t}{\sigma_T} \frac{\partial T}{\partial x_i} - \epsilon$$
 (2.15)

where Equations (2.5) and (2.7) have been substituted for the turbulent stresses and heat fluxes.

The one-equation model is comprised of Equation (2.15) and the Kolmogorov-Prandtl relationship (Equation (2.11)). Although some account of the transport of turbulence is introduced, it remains necessary to define an appropriate length scale. Thus the one-equation model is limited by the same restriction as Prandtl's mixing-length model. For this reason, researchers have moved on to a two-equation formulation in which the length scale is determined from a second transport equation.

2.1.5 Two-Equation Models

Although some models employ a transport equation for the length scale L itself, it

is not necessary or even most convenient to do so. Several two-equation models have been proposed including the k-L, k-kL, and k- ω (vorticity) models, but it is the k- ε model which has been the most popular to date. Although all of the models are similar, the ε equation has a practical advantage over the others because it requires one less source term [1].

The exact equation for ϵ can be derived from the Navier-Stokes equations, but the inherent complexity leads to dramatic modelling requirements. As a result, a form of the ϵ equation based on physical arguments is employed,

$$\frac{\partial \varepsilon}{\partial \tau} + u_i \frac{\partial \varepsilon}{\partial x_i} = \frac{\partial}{\partial x_i} \left(\frac{v_t}{\sigma_{\varepsilon}} \frac{\partial \varepsilon}{\partial x_i} \right) + C_{\varepsilon_1} \frac{\varepsilon}{k} P_k + C_{\varepsilon_3} \frac{\varepsilon}{k} G_k - C_{\varepsilon_2} \frac{\varepsilon^2}{k}$$
 (2.16)

where P_k is the generation of turbulence kinetic energy by shear and G_k is the generation of k by buoyancy,

$$P_{k} = v_{t} \left(\frac{\partial u_{i}}{\partial x_{j}} + \frac{\partial u_{j}}{\partial x_{i}} \right) \frac{\partial u_{i}}{\partial x_{j}}$$
 (2.17)

$$G_k = \beta g_i \frac{v_t}{\sigma_T} \frac{\partial T}{\partial x_i}$$
 (2.18)

Substitution for L in terms of k and ε in the Kolmogorov-Prandtl relationship (Equation (2.11)) yields the following expression for eddy viscosity,

$$v_t = \frac{C_{\mu}k^2}{\varepsilon} \tag{2.19}$$

This expression, along with the two transport equations (2.15 and 2.16) make up the standard k- ϵ turbulence model. The generally adopted constants are listed in Table 2.1.

С _µ	C _i	C ₂	C ₃	$\sigma_{\!\scriptscriptstyle E}$	$\sigma_{\mathbf{k}}$	$\sigma_{_{ m T}}$
. 0.09	1.44	1.92	1.44	1.3	1.0	1.0

Table 2.1: k-E Model Constants

This model has been used to predict several types of flows and has to be recognized as the most popular turbulence model to date. More complete reviews of turbulence modelling can be found in references [1], [2], and [3].

2.1.6 Near-Wall and Low-Reynolds Number Flows

The preceding models are restricted to situations where the local Reynolds number is high enough that viscous effects are unimportant. Near boundaries and in other low-Reynolds number regions, the effects of molecular viscosity must be accounted for.

In dealing with wall effects, one of the more popular approaches has been the use of 'wall functions' which relate surface boundary conditions to points outside the low-Reynolds number region based on experimental data. This insures the correct distribution of mean flow and turbulent quantities in the near-wall region. While researchers have had some success using this approach, the use of wall functions in connection with buoyancy-induced flows has been ineffective in many instances. This has led some to suggest that wall functions must be abandoned when dealing with such flow phenomena [22].

Another proposed method is the extension of the turbulence model such that it still applies within the low-Reynolds number region. This is accomplished through the use of damping functions which attempt to mimic the effects of the wall and molecular viscosity. These functions, derived from numerical and experimental data, are incorporated as modifications to the already existing model constants.

Several low-Reynolds number turbulence models have been proposed with varying degrees of success associated with each. The models of Jones and Launder [4], Launder and Sharma [5], and Lam and Bremhorst [6] have become popular in the CFD community.

A complete review of near-wall and low-Reynolds number flows is presented by Patel et al. [7].

2.1.7 Second - Order Differential Reynolds Stress/Flux Models

Perhaps the most obvious approach to the closure problem is to derive exact transport equations for the turbulent stresses and heat fluxes. The exact Reynolds stress equation was first derived by Chou [1] in 1945, while the analogous turbulent heat flux

equation followed shortly thereafter.

Exact Reynolds Stress Equation

$$\frac{\partial \overline{u'_{i}u'_{j}}}{\partial \tau} + u_{k} \frac{\partial \overline{u'_{i}u'_{j}}}{\partial x_{k}} = -\frac{\partial}{\partial x_{k}} (\overline{u'_{k}u'_{i}u'_{j}}) - \frac{1}{\rho} \left(\frac{\partial \overline{u'_{j}p'}}{\partial x_{i}} + \frac{\partial \overline{u'_{i}p'}}{\partial x_{j}} \right) - \overline{u'_{i}u'_{k}} \frac{\partial u_{j}}{\partial x_{k}} \quad (2.20)$$

$$-\overline{u'_{j}u'_{k}}\frac{\partial u_{i}}{\partial x_{k}}-\beta(g_{l}\overline{u'_{j}t'}+g_{l}\overline{u'_{i}t'})+\overline{\frac{p'}{\rho}\left(\frac{\partial u'_{i}}{\partial x_{j}}+\frac{\partial u'_{j}}{\partial x_{i}}\right)}-2\nu_{l}\overline{\frac{\partial u'_{i}}{\partial x_{k}}\frac{\partial u'_{j}}{\partial x_{k}}}$$

Exact Turbulent Heat Flux Equation

$$\frac{\partial \overline{u'_{i}t'}}{\partial \tau} + u_{k} \frac{\partial \overline{u'_{i}t'}}{\partial x_{k}} = -\frac{\partial}{\partial x_{k}} \left(\overline{u'_{i}u'_{k}t'} + \frac{1}{\rho} \delta_{ik} \overline{p't'} \right) - \overline{u'_{i}u'_{j}} \frac{\partial t}{\partial x_{j}} - \overline{u'_{j}t'} \frac{\partial u_{i}}{\partial x_{j}}$$

$$-\beta g_{i} \overline{t'^{2}} + \frac{1}{\rho} \overline{p'} \frac{\partial t'}{\partial x_{i}} - (\alpha_{i} + \nu_{i}) \frac{\partial u'_{i}}{\partial x_{k}} \frac{\partial t'}{\partial x_{k}}$$
(2.21)

Both equations contain complicated higher order terms involving double and triplecorrelations of fluctuating quantities. These terms must be approximated if the equation set is to be closed at this level.

Launder et al. and Gibson and Launder proposed [1], respectively, the following modelled forms for the transport of the Reynolds stress and the turbulent heat flux:

Modelled Reynolds Stress Equation

$$\frac{\partial \overline{u'_{i}u'_{j}}}{\partial \tau} + u_{l} \frac{\partial \overline{u'_{i}u'_{j}}}{\partial x_{l}} = c_{s} \frac{\partial}{\partial x_{l}} \left(\frac{k}{\varepsilon} \overline{u'_{k}u'_{l}} \frac{\partial \overline{u'_{i}u'_{j}}}{\partial x_{k}} \right) - \overline{u'_{i}u'_{l}} \frac{\partial u_{i}}{\partial x_{l}} + P_{ij}$$
 (2.22)

$$-c_{1}\frac{\varepsilon}{k}\left(\overline{u'_{i}u'_{j}}-\frac{2}{3}\delta_{ij}k\right)-c_{2}\left(P_{ij}-\frac{2}{3}\delta_{ij}P_{k}\right)-c_{3}\left(G_{ij}-\frac{2}{3}\delta_{ij}G_{k}\right)+G_{ij}-\frac{2}{3}\varepsilon\delta_{ij}$$

Modelled Turbulent Heat Flux Equation

$$\frac{\partial \overline{u'_{i}t'}}{\partial \tau} + u_{l} \frac{\partial \overline{u'_{i}t'}}{\partial x_{l}} = c_{3\theta} \frac{\partial}{\partial x_{l}} \left(\frac{k}{\varepsilon} \overline{u'_{k}u'_{l}} \frac{\partial \overline{u'_{t}t'}}{\partial x_{k}} \right) - \overline{u'_{i}u'_{j}} \frac{\partial T}{\partial x_{j}} - \overline{u'_{j}t'} \frac{\partial u_{i}}{\partial x_{j}} - \beta g_{i} \overline{t'^{2}}$$

$$- c_{1\theta} \frac{\varepsilon}{k} \overline{u'_{i}t'} + c_{2\theta} \overline{u'_{l}t'} \frac{\partial u_{i}}{\partial x_{j}} + c_{3\theta} \beta g_{i} \overline{t'^{2}}$$
(2.23)

where stress production, P_{ij} , and buoyancy production, G_{ij} , are given by:

$$P_{ij} = -\overline{u'_{i}u'_{l}}\frac{\partial u_{j}}{\partial x_{l}} - \overline{u'_{j}u'_{l}}\frac{\partial u_{i}}{\partial x_{l}}$$
(2.24)

$$G_{ij} = -\beta \left(g_i \overline{u'_j t'} + g_j \overline{u'_i t'} \right) \tag{2.25}$$

The differential stress/flux model is comprised of Equations (2.22) and (2.23), transport equations for k and ϵ , and an expression for temperature variance. The inherent complexity and immense computing power requirement has limited the popularity of this model thus far.

2.1.8 Algebraic Stress/Flux Models

For practical applications, researchers have attempted to simplify the Reynolds stress and turbulent heat flux transport equations without a significant loss of physical accuracy. As gradients of the dependent variables occur only in the rate of change, convection, and diffusion terms, these equations can be rendered algebraic with appropriate modelling.

Rodi [8], and Gibson and Launder [1] proposed relationships for the transport of turbulent stresses and heat flux, respectively. Both use the assumption that this transport is proportional to the transport of turbulence kinetic energy:

$$\frac{D\overline{u'_{i}u'_{j}}}{Dt} - Diff(\overline{u'_{i}u'_{j}}) = \frac{\overline{u'_{i}u'_{j}}}{k} \left(\frac{Dk}{Dt} - Diff(k)\right) = \frac{\overline{u'_{i}u'_{j}}}{k} \left(P_{k} + G_{k} - \varepsilon\right)$$
(2.26)

$$\frac{D\overline{u'_{i}t'}}{Dt} - Diff(\overline{u'_{i}t'}) = \frac{\overline{u'_{i}t'}}{2k} \left(\frac{Dk}{Dt} - Diff(k)\right) = \frac{\overline{u'_{i}t'}}{2k} \left(P_{k} + G_{k} - \varepsilon\right)$$
(2.27)

Substituting these relationships into the modelled transport equations (Equations (2.22) and (2.23)) gives simpler, algebraic forms for the Reynolds stress and turbulent heat flux:

Algebraic Reynolds Stress Equation

$$\overline{u'_{i}u'_{j}} = \frac{\frac{k}{\varepsilon} \left[(1 - C_{2}) \left(P_{ij} - \frac{2}{3} \delta_{ij} P_{k} \right) + (1 - C_{3}) \left(G_{ij} - \frac{2}{3} \delta_{ij} G_{k} \right) \right]}{\frac{P_{k} + G_{k}}{\varepsilon} - 1 + C_{1}} + \frac{2}{3} k \delta_{ij} \qquad (2.28)$$

Algebraic Turbulent Heat Flux Equation

$$\frac{\overline{u'_{i}t'}}{\overline{u'_{i}t'}} = \frac{-\frac{k}{\varepsilon} \left[\overline{u'_{i}u'_{j}} \frac{\partial T}{\partial x_{j}} + (1 - C_{2\theta}) \overline{u'_{i}t'} \frac{\partial u_{i}}{\partial x_{j}} + (1 - C_{3\theta}) \beta g_{i}^{\overline{t'}^{2}} \right]}{\frac{1}{2} \left(\frac{P_{k} + G_{k}}{\varepsilon} - 1 \right) + C_{1\theta}}$$
(2.29)

These equations are often simplified further by assuming that the turbulence is in a state of local equilibrium $(P_k + G_k = \varepsilon)$.

The algebraic stress/flux model consists of Equations (2.28) and (2.29), the transport equations for k and ε , and an equation for the temperature variance.

2.2 Previous Numerical Studies

2.2.1 Two - Equation Models

In one of the earliest applications of a two-equation model to buoyant flow, Plumb and Kennedy [9] applied the Jones and Launder low-Reynolds number k- ϵ model to natural convection from a vertical constant temperature surface. The researchers reported satisfactory agreement with available experimental data as the model overpredicted velocity in the outer portion of the boundary layer, overpredicted the heat transfer rate and failed to predict the sharp peak in k near the wall.

Markatos and Pericleous [10] used a k-ɛ model with wall functions to model natural convection in a side-heated square cavity. Although no comparison to turbulent data was made, the researchers reported that 'the results showed some of the experimentally observed features indicating qualitative agreement'.

Humphrey and To [11] studied free and mixed convection in a strongly heated cavity using a low-Reynolds number k- ε model. For the natural convection case, the researchers found that the eddy diffusion coefficient was underpredicted leading to an overprediction of Nusselt number. The mixed convection tests indicated that buoyancy

dominated flow occurred when the Richardson number was greater than 2, and inertia dominated flow occurred for Richardson number less than 0.4. For both free and mixed convection, the results were in good qualitative agreement with available flow visualization data.

Ince and Launder [12] studied natural convection in rectangular cavities using the Jones and Launder low-Reynolds number model. Although satisfactory results were initially obtained, the researchers found excellent agreement with experimental data when the Yap source term [13] was added to the ε equation. The purpose of this term is to increase the dissipation near the wall thereby decreasing the excessive length scales predicted in this region by the original model. The authors also found that the results could be marginally improved through the use of the 'generalized gradient diffusion hypothesis' in calculating the turbulent heat flux.

Henkes et al. [14] performed a comparative study involving the k-ε model in connection with various low-Reynolds number models and the wall function approach. For natural convection in a square cavity, the researchers found that the use of wall functions leads to overpredicted heat transfer rates. It was also argued that the combination of buoyant source terms in the k and ε equations has a small net effect on the resulting turbulent viscosity.

Davidson [15] studied natural convection in a rectangular cavity employing a modified low-Reynolds number model. Corrections to the damping functions were made to account for viscous effects in free flows while remaining consistent in its near-wall behaviour. The predictions showed very good agreement with both the experimental data

of Cheesewright et al. [16] and results obtained with the Lam and Bremhorst model.

2.2.2 Differential and Algebraic Stress/Flux Models

Several studies of buoyancy-induced cavity flow involving more physically realistic turbulence models have been carried out in the past.

Rodi [8] studied vertical buoyant jets with the aid of an algebraic stress/flux model. It was found that the predicted spreading rates were in better agreement with the experimental data than those calculated using the standard k- ϵ model. The temperature variance, based on an algebraic relationship assuming a constant time scale ratio R (defined in Equation (3.27)), was generally overpredicted and not properly distributed. Rodi suggests solving a complete transport equation for temperature variance.

To and Humphrey [17] studied natural convection from a heated, vertical plate using a low-Reynolds number k- ϵ model and an algebraic stress/flux model. The latter also employed an algebraic expression for temperature variance while assuming a constant R value. Both models were shown to predict the mean flow and heat transfer well with only minor discrepancies between the data. The researchers also found that the algebraic model was capable of predicting the anisotropic turbulence characteristics.

Silva and Emery [18] used an algebraic stress/flux model to predict natural convection flow in a square enclosure and compared the results to those obtained using a k-ɛ model. It was found that the algebraic model predicted higher average Nusselt numbers and a more developed momentum boundary layer.

Davidson [19], again investigating flow in a rectangular cavity, used a hybrid of

the eddy viscosity and algebraic approaches. Specifically, Davidson added the buoyant part of the algebraic Reynolds stress equation (Equation 2.28) to the standard eddy viscosity relationship (Equation 2.5). Davidson also made use of the generalized gradient diffusion hypothesis when calculating the turbulent heat flux. While noting that the model predicted turbulent quantities more realistically, the results showed a small effect on the heat transfer and mean flow.

In an evaluation of turbulence models for predicting buoyant flow, Shabbir and Taulbee [20] studied the axisymmetric buoyant plume. By substituting experimental data into the closure equations, the authors were able to investigate the validity of the k-\varepsilon model and the algebraic stress/flux model. The researchers found that the k-\varepsilon model could not predict the proper axial heat flux distribution, while the algebraic model could not yield realistic values for this quantity if the magnitude of the temperature variance was properly predicted. Shabbir and Taulbee suggest that models such as Rodi's have made up for incorrect predictions of the axial heat flux by overpredicting the temperature variance thus leading to a well-predicted mean flow. The authors also state that not only is a transport equation for the temperature variance required, but a full differential stress/flux treatment before the axial heat flux and the temperature variance can be calculated properly.

Hanjalic and Vasic [21] studied natural convection in rectangular and square cavities using an algebraic heat flux model. The authors proposed that the accurate calculation of Reynolds stress components is not necessary and thus used the eddy viscosity representation (Equation (2.5)) for this quantity (an algebraic expression for

temperature variance was also employed with constant time-scale ratio R). Satisfactory results were obtained for side and bottom heated, and mixed configuration cavities. The researchers also indicated that three-dimensional effects are probably the major cause of reported disagreement in cavity flows.

In a review of the modelling practices associated with turbulent buoyant flows, Hanjalic [22] states that the minimum level required to obtain satisfactory results is the algebraic flux model. The author recommends the solution of transport equations for the temperature variance and its dissipation suggesting that the assumption of constant time scale ratio, R, is invalid. Hanjalic also states that the inadequacy of the turbulent diffusion model for turbulent quantities seems to be compensated by mean flow advection resulting in stronger recirculatory motion than detected by experiment. Results generated using a three equation model $(k-\epsilon-t^2)$ and a four equation model $(k-\epsilon-t^2-\epsilon_t)$ for some cavity and annulus flows were presented.

Murakami et al. [23] investigated the flow of a nonisothermal horizontal jet in an enclosure using the k-ε, algebraic stress/flux (with temperature variance transport equation) and differential stress/flux models. The authors found that the k-ε model predicted much lower values for the streamwise heat flux than the higher order models leading to poorer prediction of temperature profiles. All three models showed poor agreement just after the discharge. The results were slightly better for the differential stress/flux model as opposed to the algebraic model. The researchers attributed this to inadequate modelling of the transport of the turbulent stress and heat flux (Equations (2.26) and (2.27)).

Kato et al. [24] studied two-dimensional room airflow using an algebraic model similar to that used by Murakami et al. The authors reported a remarkable difference in the values of turbulent heat flux predicted by the k-ε and algebraic models. No comparison with experimental values was made.

Kenjeres and Hanjalic [25] studied natural convection in concentric and eccentric horizontal annuli using a three equation model. Good agreement with experimental data was obtained after adjustment of the model constants. The authors expect that better results could be obtained with a four equation model.

So and Sommer [26] present an explicit formulation of the algebraic heat flux as opposed to the implicit form given in Equation (2.29). The researchers report that this approach will prevent numerical instabilities from occurring in the heat flux equations.

Sommer and So [27] discuss the need to solve transport equations for the temperature variance and its dissipation. The authors claim that this level of modelling is necessary to predict the countergradient heat transport phenomena. Sommer and So also use the thermal time scale, in addition to the mechanical time scale, in modelling the heat flux equation.

2.3 Problem History

The present study involves the investigation of turbulent convection within a rectangular enclosure shown in Figure 2.1. Water, at temperature T_j , flows through an inlet at the top of the cavity. Heat transfer to the fluid occurs on the right vertical surface which is maintained at a constant temperature, T_w . The water exits through the outlet at

the bottom of the enclosure. The height to width aspect ratio is 2 for all cases considered.

This specific problem has previously been investigated experimentally and numerically by Nurnberg [28]. A summary of the test cases used is provided below in Table 2.2.

CASE	1	2	3	4
u _j (m/s)	.123	.124	.063	.063
T _w (°C)	20	42.5	63.0	80.6
T _j (°C)	20	22.3	24.0	25.9
Re _H	36100	47600	30000	35300
Gr _H (10-9)	0	2.87	10.7	24.2
Ri _H	0 ·	1.27	11.9	19.4

Table 2.2 - Summary of Test Cases

These cases have been chosen to study flows covering a range of Richardson (Ri) numbers. This important convection parameter is defined as the ratio of buoyant to inertial forces,

$$Ri_H = \frac{Gr_H}{Re_H^2} \tag{2.30}$$

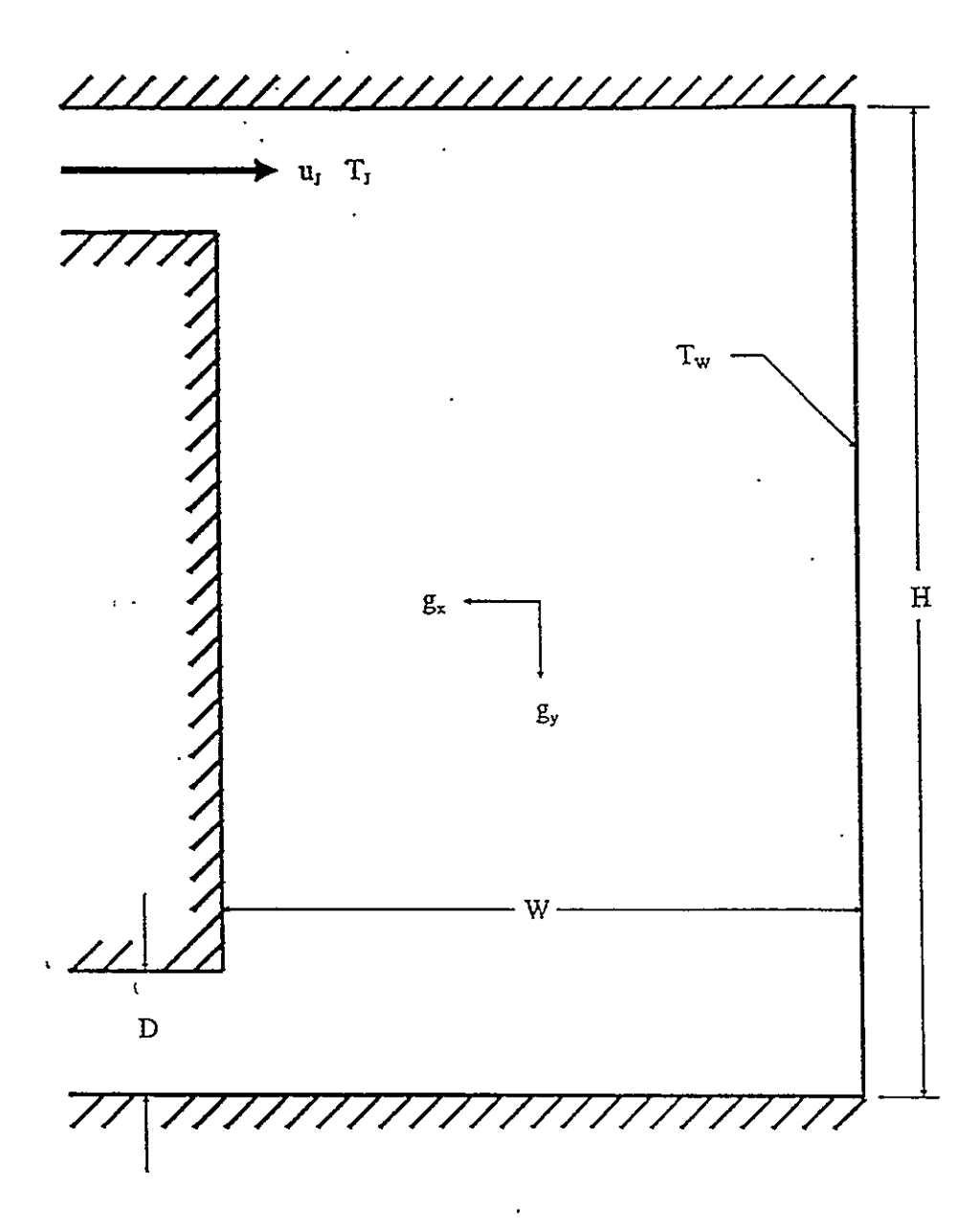


Figure 2.1: Problem Specification

The first test case, being isothermal, is purely inertia driven, while the fourth case is predominantly controlled by buoyancy. Cases Two and Three are designed for mixed convection flow where the magnitudes of these forces are comparable.

2.3.1 Experimental Results

Detailed velocity data was collected using a single component laser Doppler anemometer system while horizontal temperature profiles at three vertical locations were obtained using thermocouples. Flow visualization was also performed using the laser induced fluorescence technique.

Figure 2.2 shows the velocity measurements on the vertical plane of symmetry for Case 1. A large clockwise recirculating cell dominates the flow in the cavity while small secondary cells form in the corners. An important factor in this study is the location of flow separation along either the heated vertical surface or the adiabatic top wall. For inertia dominated flow, the fluid separates along the heated wall at a distance y_{sep} from the bottom of the cavity. If the flow is dominated by buoyancy, the fluid penetrates a distance x_{pen} from the opening to the cavity before separating along the top wall. For the isothermal case, the fluid separates on the vertical wall at a height of approximately 70 mm or 0.24 when made dimensionless by the cavity height.

Velocity measurements for Case 2 are presented in Figure 2.3. In this case buoyant effects become evident as the primary recirculating cell has decreased in size and a larger counterclockwise secondary cell has formed in the bottom right corner of the cavity. The increased secondary cell is the result of buoyancy providing a source of

positive momentum in the vertical direction along the heated wall. The result is an increase in the separation height location to 120 mm or 0.4 dimensionless units.

In Case 3 the flow is further influenced by buoyancy, as shown in Figure 2.4.

Here, two recirculating cells of approximately equal size have formed and the resulting separation height has increased to 190 mm or 0.64 dimensionless units.

Finally, the velocity measurements for Case 4 are presented in Figure 2.5. In this case the inertially driven cell seen in the previous three cases is completely overcome by buoyant forces. This results in a single large counterclockwise cell dominating the cavity flow. The fluid separates along the horizontal top wall, having a penetration depth into the cavity of 25 mm or .084 dimensionless units.

All of the LDA data described previously was supported by the flow visualization study.

2.3.2 Numerical Results

The problem was modelled in two-dimensions using the Lam and Bremhorst low-Reynolds number k-\varepsilon approach [28]. The simple eddy viscosity relationships were employed for both the Reynolds stress and turbulent heat flux terms.

Streamlines for the isothermal case are shown in Figure 2.6. The inertially driven cell has size and strength comparable to the experimental values. The predicted separation height is 0.31 dimensionless units.

Results for Case 2 are presented in Figure 2.7. Although the simulated and measured flow fields are similar, the predicted buoyant cell is larger. The separation

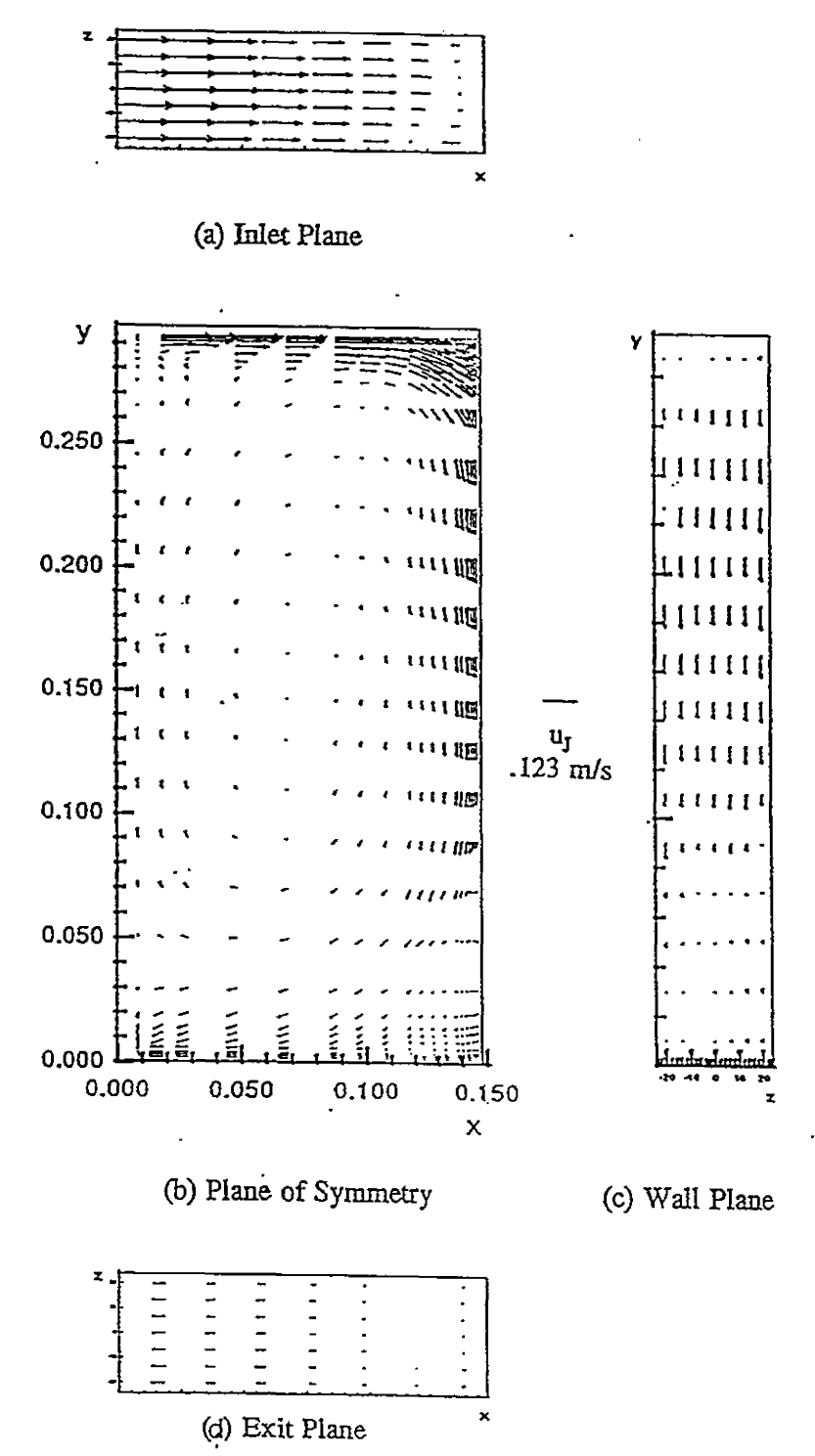


Figure 2.2 - Case 1 - LDA Results

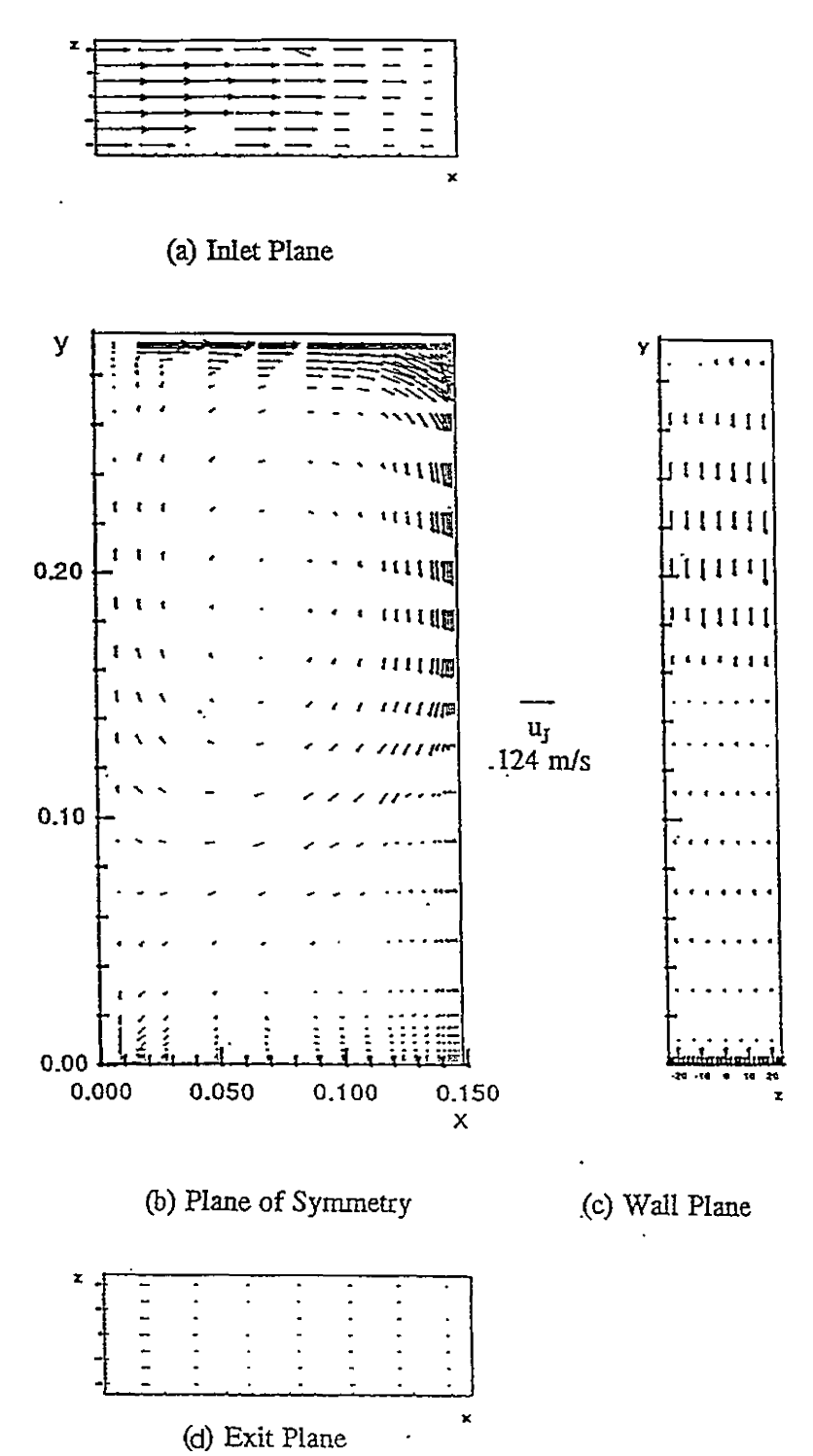


Figure 2.3 - Case 2 - LDA Results

ì

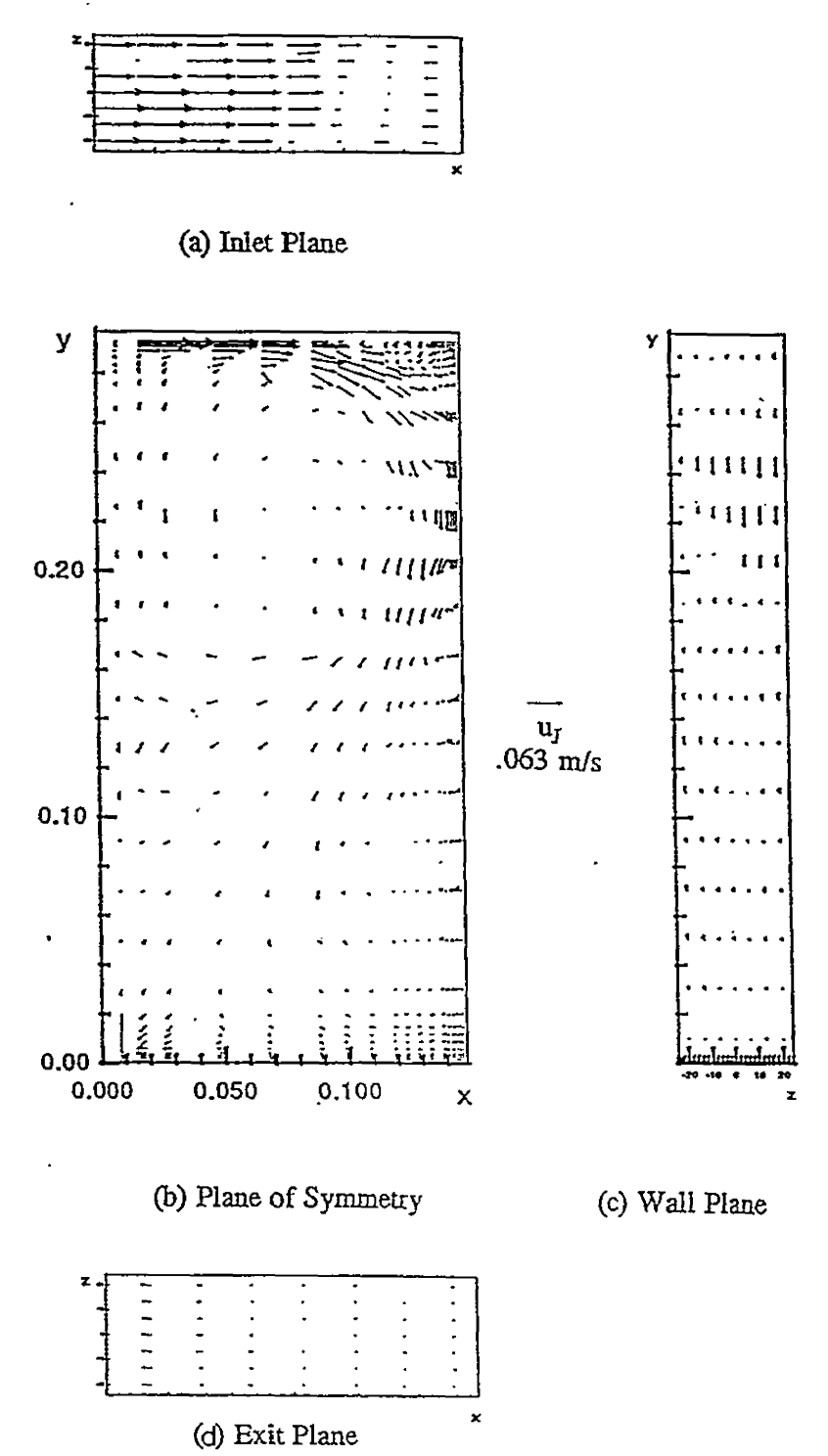
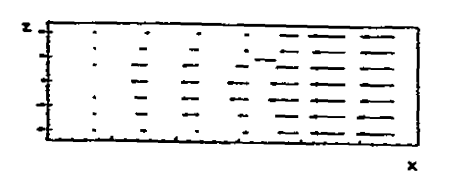
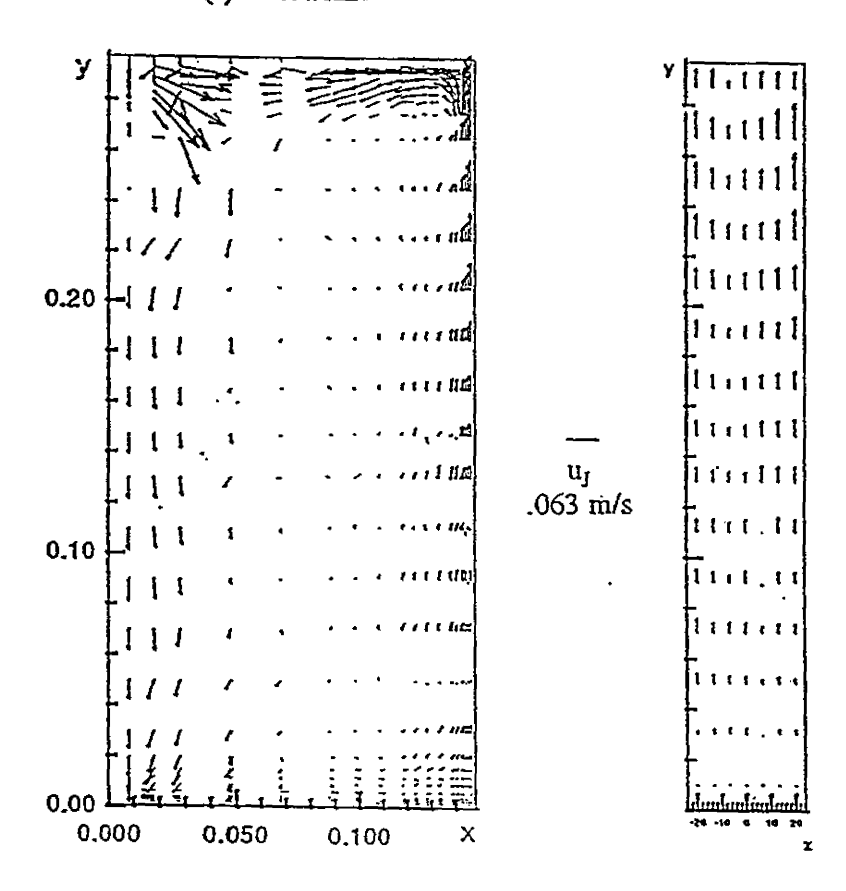
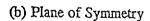


Figure 2.4 - Case 3 - LDA Results



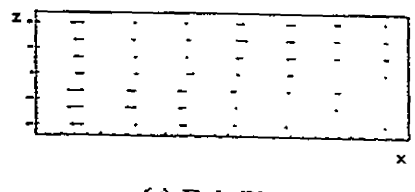
(a) Inlet Plane





(c) Wall Plane

`.,



(d) Exit Plane

Figure 2.5 - Case 4 - LDA Results

height was found to be 0.76 dimensionless units.

Case 3 results are shown in Figure 2.8. The simulations show the buoyant forces overcoming inertia resulting in one large counterclockwise rotating cell. The penetration depth of the fluid into the cavity was found to be .025 dimensionless units.

The predictions for Case 4 are shown in Figure 2.9. The flow field is similar to the experiment as it is completely dominated by buoyancy. The predicted penetration depth is .025 dimensionless units.

A summary of experimental and predicted dimensionless separation locations, Y_{sep} , and penetration depths, X_{pen} , is given in Table 2.3.

	Experimental Data		Numerical Predictions	
Case	Y_{sep}	X _{pen}	Y_{scp}	X_{pen}
1	0.24	-	0.31	-
2	0.40	-	0.76	-
3	0.64	-	-	0.025
4	-	0.084	-	0.025

Table 2.3: Separation Locations

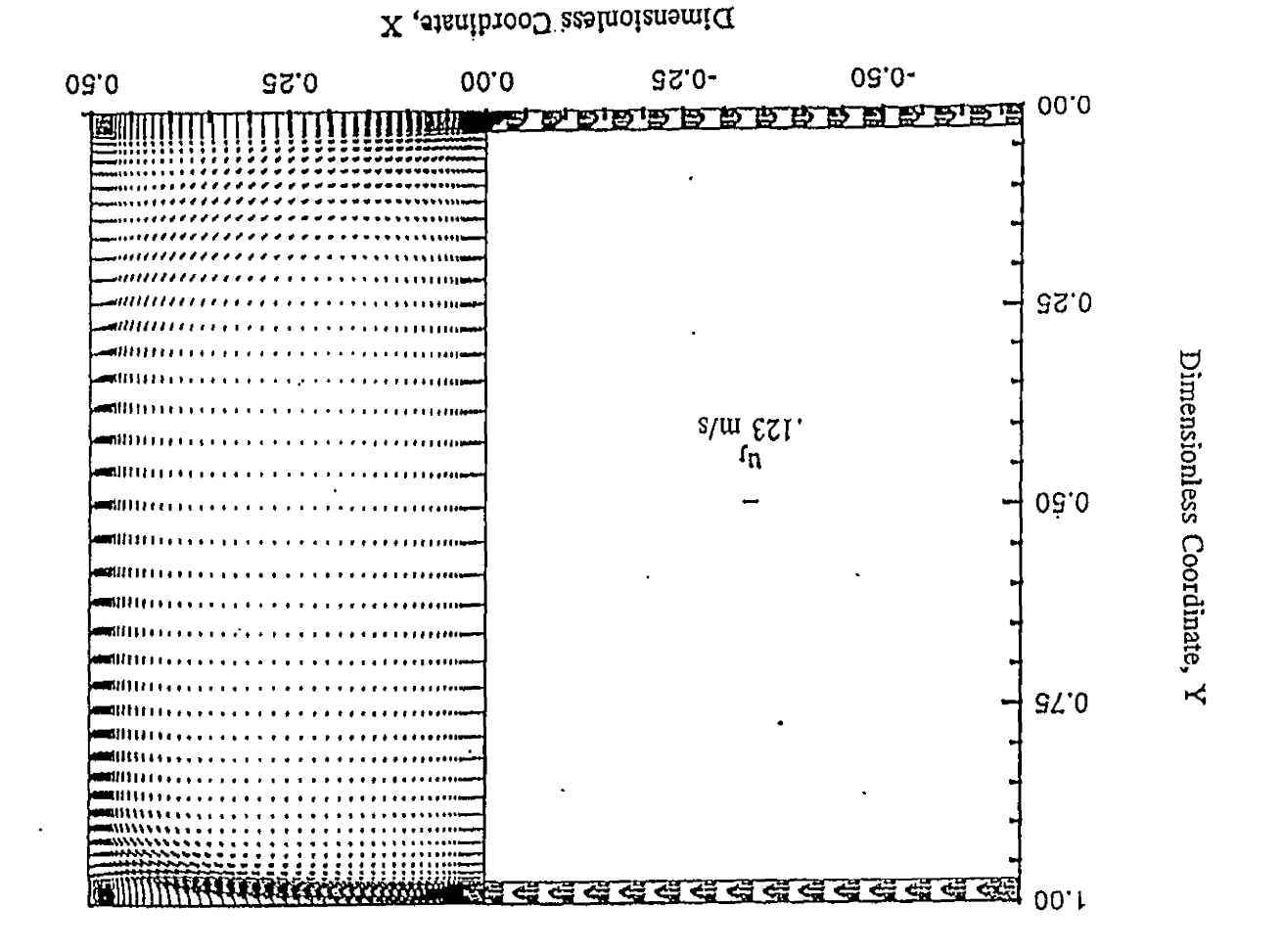
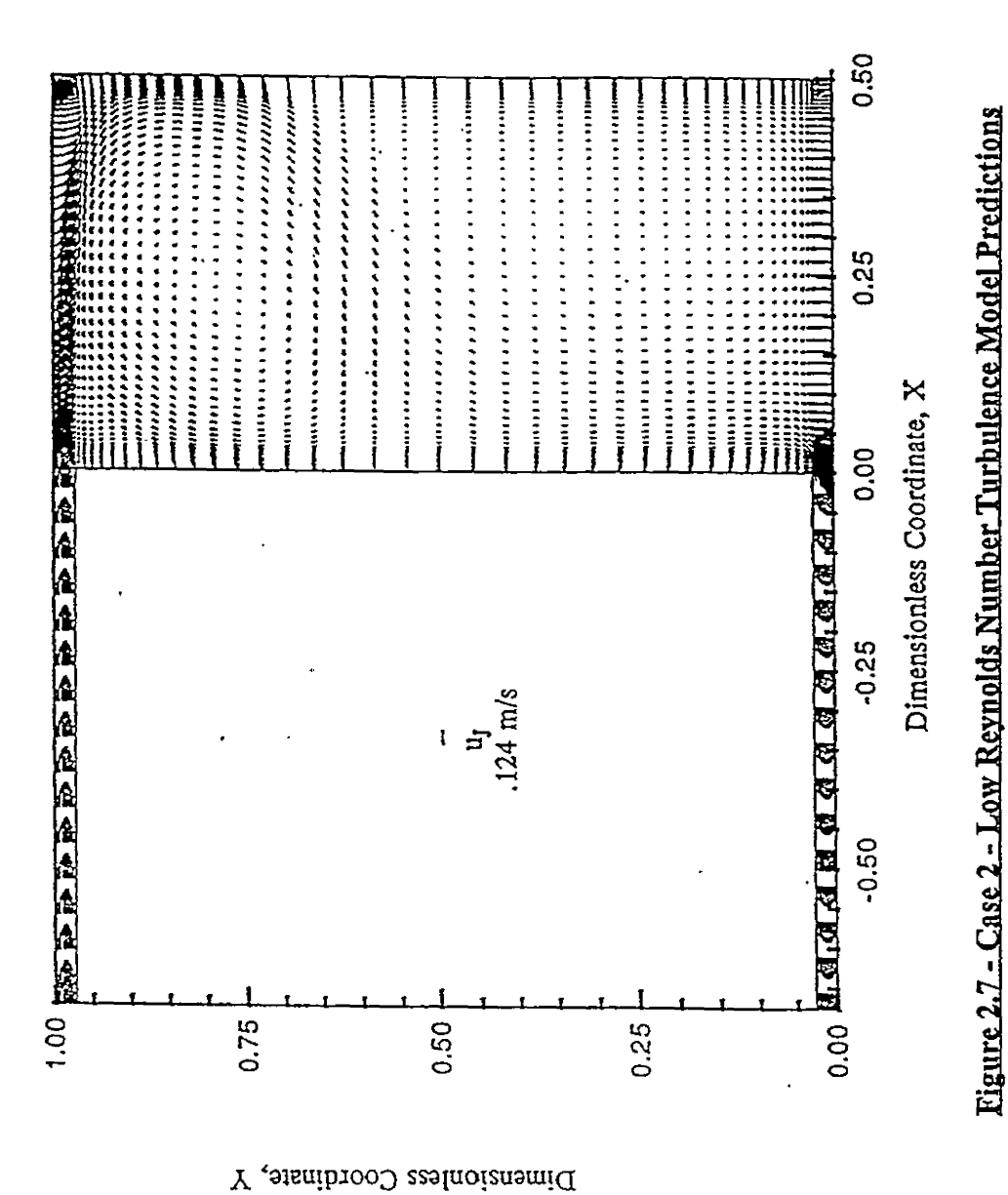


Figure 2.6 - Case I - Low Reynolds Number Turbulence Model Predictions

4 14 14



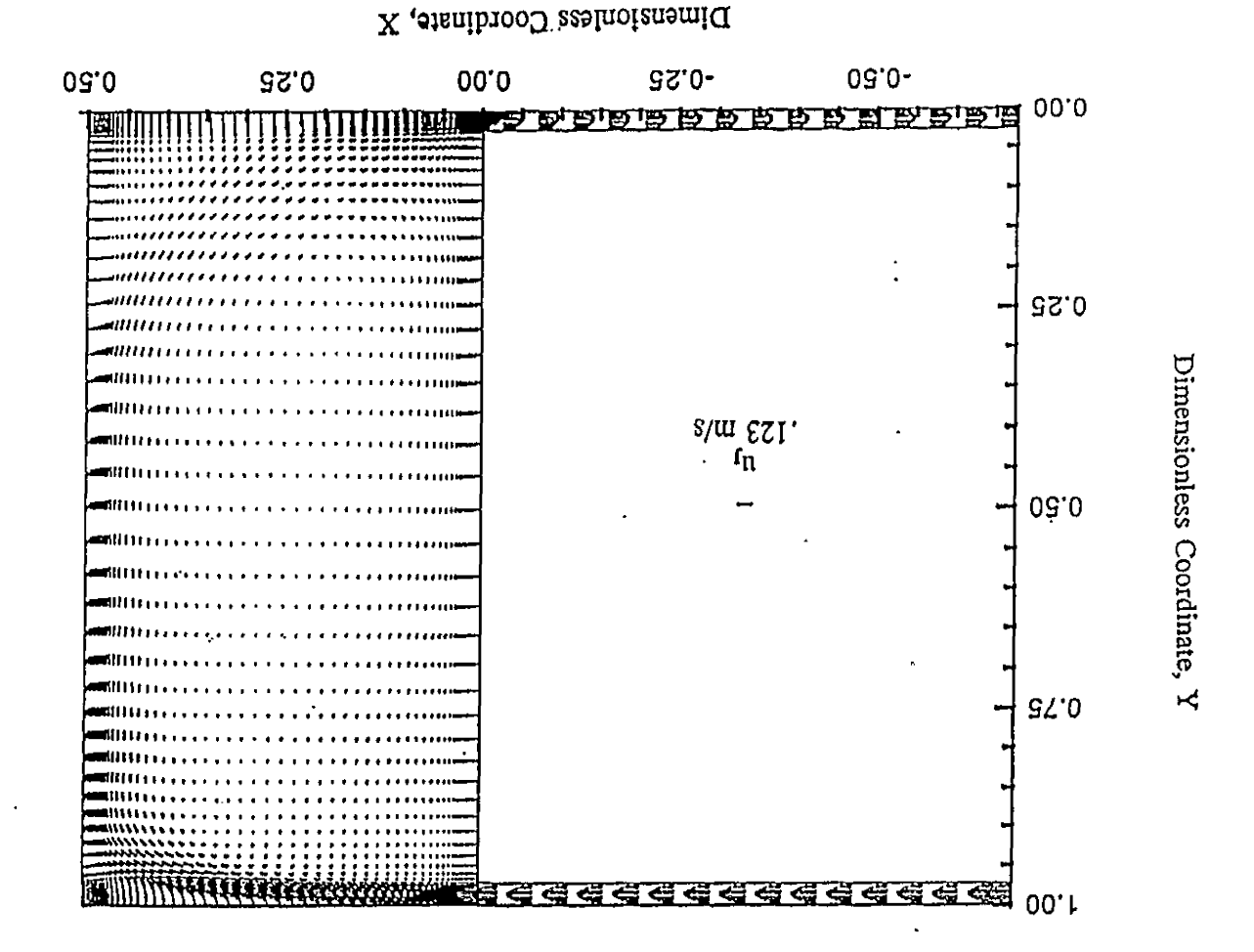


Figure 2.8 - Case 3 - Low Reynolds Number Turbulence Model Predictions

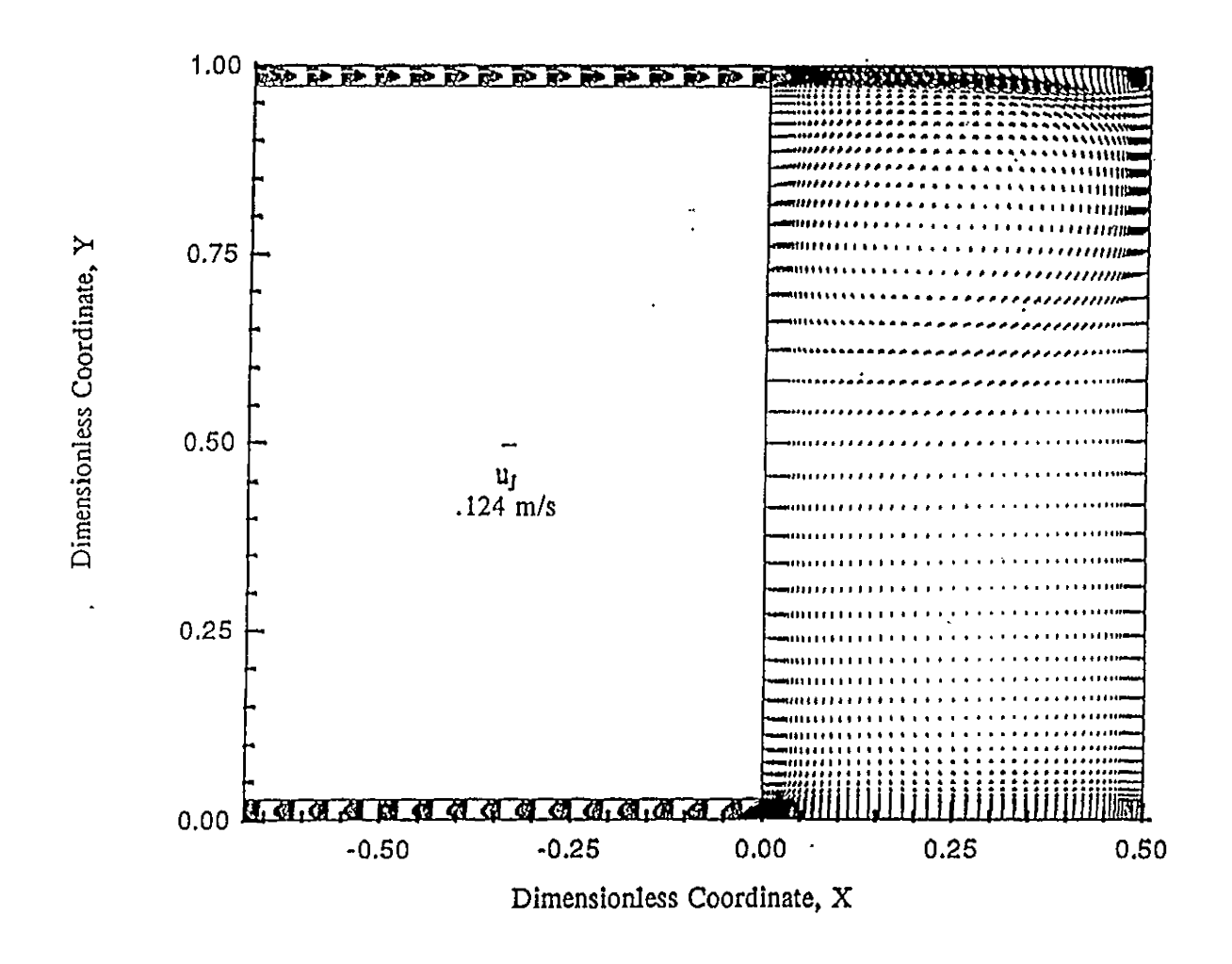


Figure 2.9 - Case 4 - Low Reynolds Number Turbulence Model Predictions

Based on the data, it may be concluded that the buoyant force is overpredicted by the current numerical model. This leads to a higher separation point in Case 2, separation along the horizontal top wall in Case 3, and decreased penetration depth in Case 4.

Clearly, an accurate estimation of the buoyant force is necessary before agreement with experimental results is possible.

CHAPTER THREE

MATHEMATICAL FORMULATION

3.1 Introduction

This chapter serves as an outline of the mathematical formulation employed in modelling the problem. Section 3.2 contains the conservation equations for velocity, temperature, turbulence kinetic energy, and dissipation of turbulence kinetic energy. The equations are presented in dimensional and dimensionless forms. Section 3.3 discusses the modelling of the turbulent heat flux and the fluctuating temperature variance. Boundary conditions for the differential equations and the Lam and Bremhorst low-Reynolds number damping functions are discussed in Section 3.4.

3.2 Governing Equations

3.2.1 Dimensional Governing Equations

The time-averaged equations governing the mean flow include the continuity, x-momentum, y-momentum, and energy equations:

Continuity

$$\frac{\partial u}{\partial x} + \frac{\partial v}{\partial y} = 0 \tag{3.1}$$

x-Momentum

$$u\frac{\partial u}{\partial x} + v\frac{\partial u}{\partial y} = -\frac{1}{\rho}\frac{\partial p}{\partial x} + \frac{\partial}{\partial x}\left((v_l + v_t)\frac{\partial u}{\partial x}\right) + \frac{\partial}{\partial y}\left((v_l + v_t)\frac{\partial u}{\partial y}\right) + \frac{\partial}{\partial y}\left((v_l + v_t)\frac{\partial u}{\partial y}\right) + \frac{\partial}{\partial y}\left((v_l + v_t)\frac{\partial u}{\partial x}\right) + \frac{\partial}{\partial y}\left((v_l + v_t)\frac{\partial v}{\partial x}\right) - \frac{2}{3}\frac{\partial k}{\partial x}$$
(3.2)

y-Momentum

$$u\frac{\partial v}{\partial x} + v\frac{\partial v}{\partial y} = -\frac{1}{\rho}\frac{\partial p}{\partial y} + \frac{\partial}{\partial x}\left((v_l + v_t)\frac{\partial v}{\partial x}\right) + \frac{\partial}{\partial y}\left((v_l + v_t)\frac{\partial v}{\partial y}\right) + \frac{\partial}{\partial y}\left((v_l + v_t)\frac{\partial v}{\partial y}\right) + \frac{\partial}{\partial y}\left((v_l + v_t)\frac{\partial v}{\partial y}\right) - g\beta(T - T_{ref}) - \frac{2}{3}\frac{\partial k}{\partial y}$$
(3.3)

Energy

$$u\frac{\partial T}{\partial x} + v\frac{\partial T}{\partial y} = \frac{\partial}{\partial x} \left(\frac{\mathbf{v}_l}{\mathbf{\sigma}_l} \frac{\partial T}{\partial x} \right) + \frac{\partial}{\partial y} \left(\frac{\mathbf{v}_l}{\mathbf{\sigma}_l} \frac{\partial T}{\partial y} \right) - \frac{\partial}{\partial x} \left(\overline{u't'} \right) - \frac{\partial}{\partial y} \left(\overline{v't'} \right)$$
(3.4)

The momentum equations were obtained by substituting the eddy viscosity relationship for

the Reynolds stress terms (Equation (2.5)) into Equation (2.3). The turbulent viscosity, v_t , is given by,

$$v_t = C_{\mu} f_{\mu} \frac{k^2}{\varepsilon} \tag{3.5}$$

where f_{μ} is a damping term to be discussed in Section 3.4.2. Forms of the k and ϵ equations incorporating low-Reynolds number damping functions are used:

Turbulent Kinetic Energy

$$u\frac{\partial k}{\partial x} + v\frac{\partial k}{\partial y} = \frac{\partial}{\partial x} \left((v_l + \frac{v_t}{\sigma_k}) \frac{\partial k}{\partial x} \right) + \frac{\partial}{\partial y} \left((v_l + \frac{v_t}{\sigma_k}) \frac{\partial k}{\partial y} \right) + G - \varepsilon + \beta g \overline{v't'}$$
 (3.6)

Dissipation of Turbulent Kinetic Energy

$$u\frac{\partial \varepsilon}{\partial x} + v\frac{\partial \varepsilon}{\partial y} = \frac{\partial}{\partial x} \left((v_l + \frac{v_t}{\sigma_{\varepsilon}}) \frac{\partial \varepsilon}{\partial x} \right) + \frac{\partial}{\partial y} \left((v_l + \frac{v_t}{\sigma_{\varepsilon}}) \frac{\partial \varepsilon}{\partial y} \right)$$

$$+ C_1 f_1 \frac{\varepsilon}{k} G - C_2 f_2 \frac{\varepsilon^2}{k} + C_3 f_3 g \beta \frac{\varepsilon}{k} \overline{vT}$$

$$(3.7)$$

where the generation of turbulence, G, is

$$G = v_t \left(2 \left(\frac{\partial u}{\partial x} \right)^2 + 2 \left(\frac{\partial v}{\partial y} \right)^2 + \left(\frac{\partial u}{\partial \dot{y}} + \frac{\partial v}{\partial x} \right)^2 \right)$$
 (3.8)

The standard model constants are given in Table 2.1 while the damping functions are discussed in Section 3.4.2. Representation of the turbulent heat flux, which appears in the energy, kinetic energy, and dissipation of kinetic energy equations, is discussed in Section 3.3.

3.2.2 Dimensionless Variables

The governing equations can be cast into a non-dimensional form when the following variable definitions are employed:

Dimensionless Distance

$$X = \frac{x}{H} \qquad Y = \frac{y}{H} \tag{3.9}$$

where H is the cavity height.

Dimensionless Velocity

$$U = \frac{u}{U_{jet}} \qquad V = \frac{v}{U_{jet}} \tag{3.10}$$

where Ujet is the average inlet jet velocity.

Dimensionless Temperature

$$\theta = \frac{T - T_j}{T_W - T_j} \tag{3.11}$$

where T_j is the inlet temperature of the fluid and $T_{\mathbf{w}}$ is the temperature of the heated wall.

Dimensionless Pressure

$$P = \frac{p}{\rho U_{jet}^2} \tag{3.12}$$

Dimensionless Kinetic Energy

$$k^* = \frac{k}{U_{iet}^2} \tag{3.13}$$

Dimensionless Dissipation of Turbulent Kinetic Energy

$$\varepsilon^{\bullet} = \frac{\varepsilon H}{U_{iet}^{3}} \tag{3.14}$$

3.2.3 Dimensionless Governing Equations

Substitution of the dimensionless dependent variables into the governing equations yields the following equations:

Dimensionless Continuity

$$\frac{\partial U}{\partial X} + \frac{\partial V}{\partial Y} = 0 \tag{3.15}$$

Dimensionless X-Momentum

$$U\frac{\partial U}{\partial X} + V\frac{\partial U}{\partial Y} = -\frac{\partial P}{\partial X} + \frac{\partial}{\partial X}\left(\left(\frac{a}{Re_l} + \frac{a}{Re_t}\right)\frac{\partial U}{\partial X}\right) + \frac{\partial}{\partial Y}\left(\left(\frac{a}{Re_l} + \frac{a}{Re_t}\right)\frac{\partial U}{\partial Y}\right)$$
(3.16)

$$+ \frac{\partial}{\partial X} \left(\left(\frac{a}{Re_I} + \frac{a}{Re_t} \right) \frac{\partial U}{\partial X} \right) + \frac{\partial}{\partial Y} \left(\left(\frac{a}{Re_I} + \frac{a}{Re_t} \right) \frac{\partial V}{\partial X} \right) - \frac{2}{3} \frac{\partial k^*}{\partial X}$$

Dimensionless Y-Momentum

$$U\frac{\partial V}{\partial X} + V\frac{\partial V}{\partial Y} = -\frac{\partial P}{\partial Y} + \frac{\partial}{\partial X} \left(\left(\frac{a}{Re_l} + \frac{a}{Re_t} \right) \frac{\partial V}{\partial X} \right) + \frac{\partial}{\partial Y} \left(\left(\frac{a}{Re_l} + \frac{a}{Re_t} \right) \frac{\partial V}{\partial Y} \right)$$
(3.17)

$$+ \frac{\partial}{\partial X} \left(\left(\frac{a}{Re_l} + \frac{a}{Re_t} \right) \frac{\partial U}{\partial Y} \right) + \frac{\partial}{\partial Y} \left(\left(\frac{a}{Re_l} + \frac{a}{Re_t} \right) \frac{\partial V}{\partial Y} \right) + \frac{Gr_y a^2 \theta}{Re_t^2} - \frac{2}{3} \frac{\partial k^*}{\partial Y}$$

where Re, and Re, are Reynolds numbers based on laminar and turbulent viscosity, respectively,

$$Re_{I} = \frac{U_{jet}D}{v_{I}} \qquad Re_{t} = \frac{U_{jet}D}{v_{t}}$$
 (3.18)

Dimensionless Energy

$$U \frac{\partial \theta}{\partial X} + V \frac{\partial \theta}{\partial Y} = \frac{\partial}{\partial X} \left(\frac{a}{Re_{l}\sigma_{l}} \frac{\partial \theta}{\partial X} \right) + \frac{\partial}{\partial Y} \left(\frac{a}{Re_{l}\sigma_{l}} \frac{\partial \theta}{\partial Y} \right)$$

$$- \frac{\partial}{\partial X} \left(\overline{u't'} \right)^{*} - \frac{\partial}{\partial Y} \left(\overline{v't'} \right)^{*}$$
(3.19)

Dimensionless Turbulent Kinetic Energy

$$U \frac{\partial k^*}{\partial X} + V \frac{\partial k^*}{\partial Y} = \frac{\partial}{\partial X} \left(\left(\frac{a}{Re_l} + \frac{a}{\sigma_k Re_t} \right) \frac{\partial k^*}{\partial X} \right) + \frac{\partial}{\partial Y} \left(\left(\frac{a}{Re_l} + \frac{a}{\sigma_k Re_t} \right) \frac{\partial k^*}{\partial Y} \right)$$

$$+ G^* - \varepsilon^* + \frac{a^2 (Gr_y)_l^2}{Re_l^2} \overline{v't'}$$
(3.20)

Dimensionless Dissipation of Turbulent Kinetic Energy

$$U \frac{\partial \varepsilon^*}{\partial X} + V \frac{\partial \varepsilon^*}{\partial Y} = \frac{\partial}{\partial X} \left(\left(\frac{a}{Re_l} + \frac{a}{\sigma_{\varepsilon} Re_t} \right) \frac{\partial \varepsilon^*}{\partial X} \right) + \frac{\partial}{\partial Y} \left(\left(\frac{a}{Re_l} + \frac{a}{\sigma_{\varepsilon} Re_t} \right) \frac{\partial \varepsilon^*}{\partial Y} \right)$$
(3.21)

+
$$C_1 f_1 \frac{\varepsilon^*}{k^*} G^* - C_2 f_2 \frac{\varepsilon^{*2}}{k^*} + C_3 f_3 \frac{\varepsilon^*}{k} \frac{a^2 (Gr_y)_l^2}{Re_l^2} \frac{v't'}{v't'}$$

where the dimensionless generation of turbulence, G*, is

$$G^* = \frac{a}{Re_t} \left[2 \left(\frac{\partial U}{\partial X} \right)^2 + 2 \left(\frac{\partial V}{\partial Y} \right)^2 + \left(\frac{\partial U}{\partial Y} + \frac{\partial V}{\partial X} \right)^2 \right]$$
(3.22)

3.3 Representation of Turbulent Heat Flux

The turbulent heat flux, appearing in the energy, kinetic energy of turbulence, and dissipation equations, is calculated according to Equation (2.29). The additional simplifying assumption of local equilibrium $(P_k + G_k = \epsilon)$ is also invoked. The resulting algebraic turbulent heat flux equations are,

Dimensional Turbulent Heat Flux Equation

$$\overline{u'_{i}t'} = -C \frac{k}{\varepsilon} \left(\overline{u'_{i}u'_{j}} \frac{\partial T}{\partial x_{i}} + \xi \overline{u'_{j}t'} \frac{\partial u_{i}}{\partial x_{i}} + \eta \beta g_{i} \overline{t'^{2}} \right)$$
(3.23)

Dimensionless Turbulent Heat Flux Equation

$$(\overline{u'_i t'})^* = -\frac{Ck^*}{\varepsilon^*} \left[(\overline{u'_i u'_j})^* \frac{\partial \theta}{\partial X_j} + \xi (\overline{u'_f t'})^* \frac{\partial U_i}{\partial X_j} + \eta \frac{a^2 (Gr_i)_l}{Re_l^2} (\overline{t'^2})^* \right]$$
(3.24)

where C, ξ , and η are model constants discussed in Chapter Five.

All of the quantities in the above relationship are known with the exception of the fluctuating temperature variance. This quantity can be accounted for using a modelled transport equation [22],

Dimensionless Fluctuating Temperature Variance Equation

$$U_{i} \frac{\partial \overline{t'^{2}}^{*}}{\partial X_{i}} = \frac{\partial}{\partial X_{i}} \left[\left(\frac{c_{i} f_{\mu} k^{*2}}{\varepsilon^{*}} + \frac{a}{\sigma_{i} Re_{i}} \right) \frac{\partial \overline{t'^{2}}^{*}}{\partial X_{i}} \right] - 2 \left(\overline{u'_{j} t'} \right)^{*} \frac{\partial \theta}{\partial X_{j}} - 2 \varepsilon_{\theta}^{*}$$
(3.25)

where ε_0^* represents the dimensionless dissipation of temperature variance. This quantity is calculated from a simple, algebraic relationship given below,

$$\varepsilon_0^* = \frac{\varepsilon^*}{R} \frac{(\overline{t'^2})^*}{2k^*} \tag{3.26}$$

The quantity R is defined as the ratio of the mechanical to the thermal time scale,

$$R = \frac{k/\varepsilon}{\overline{t'^2}/2\,\varepsilon_0} \tag{3.27}$$

The dimensionless temperature variance equation can also be modelled using a simplified algebraic expression,

$$(\overline{t'^2})^* = -2R \frac{k^*}{\varepsilon^*} (\overline{u'_j t'})^* \frac{\partial \theta}{\partial X_j}$$
 (3.28)

The fluctuating temperature variance is modelled using both the algebraic (Equation (3.28)) and differential (Equation (3.25)) relationships within this study.

3.4 Boundary Conditions

3.4.1 Velocity and Temperature Boundary Conditions

The following boundary conditions are used to simulate the velocity and temperature fields:

No Slip Wall:

Velocities normal and adjacent to a solid boundary are set equal to zero. For example, along the lower horizontal wall,

$$U|_{y=0} = 0$$

$$V|_{y=0} = 0$$
(3.29)

Adiabatic Wall:

Temperature gradients normal to the insulated surfaces are set equal to zero indicating zero heat flux. For the lower, horizontal wall,

$$\frac{\partial \theta}{\partial Y}\big|_{y=0} = 0 \tag{3.30}$$

Isothermal Wall:

The dimensionless temperature of the heated surface is set equal to one,

$$\theta \mid_{x - \overline{R}'} = 1 \tag{3.31}$$

Inflow Boundary: `

Inflow conditions are specified at the point of expansion into the cavity. A powerlaw profile is used for the X-momentum component while the Y-momentum component is set equal to zero. The dimensionless temperature at this location is also set equal to zero.

Outflow Boundary:

Outflow conditions are specified at the end of the developing length added to the bottom outlet of the cavity. The flow is assumed to be fully-developed upon exit at this location such that,

$$V|_{out} = 0$$

$$\frac{\partial U}{\partial X}|_{out} = 0 \qquad \frac{\partial \theta}{\partial X}|_{out} = 0$$
(3.32)

3.4.2 Turbulence Boundary Conditions

Turbulence effects are incorporated using the Lam and Bremhorst low-Reynolds number turbulence model [28]. The boundary conditions for turbulence kinetic energy

and dissipation of turbulence kinetic energy next to a solid wall are,

$$k^*|_{wall} = 0$$
 $\frac{\partial \varepsilon^*}{\partial n}|_{wall} = 0$ (3.33)

where n is the direction normal to the surface.

To account for viscous effects in the vicinity of the solid walls or in other low-Reynolds number regions, the following damping functions are used,

$$f_{\mu} = exp \left[\frac{-2.5}{1 + \frac{R_t}{50}} \right]$$

$$f_1 = 1$$

$$f_2 = 1 - .3 exp (-R_t)^2$$

$$f_3 = 1$$
(3.34)

where the turbulent Reynolds number, R, , is given by,

$$R_t = \frac{Re_t \, k^{*2}}{a \, \varepsilon^*} \tag{3.35}$$

The effect of the Yap source term [13] in the dissipation equation is also studied.

The purpose of this term is to increase the dissipation in the near-wall region thereby reducing the turbulent length-scale to a more reasonable level. The term proposed by Yap is,

$$S_{yap} = 0.83 \left(\frac{k^{3/2}}{\varepsilon c_l y} - 1 \right) \left(\frac{k^{3/2}}{\varepsilon c_l y} \right)^2 \frac{\varepsilon^2}{k}$$
 (3.36)

where y is the distance from the wall such that the term goes to zero outside the near-wall region.

The turbulent kinetic energy at the entrance to the cavity is specified as [28],

$$k_{in}^* = \frac{\frac{3}{2} (\psi U_{jet})^2}{U_{iet}^2}$$
 (3.37)

where Ψ , the turbulence intensity, is taken to be 10%.

The dissipation of turbulence kinetic energy at the inlet was varied to investigate a range of inlet turbulent length scales, l_{in} , where

$$l_{in} = \frac{C_{\mu} f_{\mu} k^{\frac{3}{2}}}{\varepsilon} \tag{3.38}$$

Because the equation for turbulent heat flux is algebraic, no boundary conditions are required for this quantity. When the full transport equation for fluctuating temperature variance is employed (Equation (3.25)), the following boundary condition is imposed at the solid surface:

$$\overline{\left(t^{\prime 2}\right)^{*}}|_{wall}=0 \tag{3.39}$$

CHAPTER FOUR

NUMERICAL FORMULATION

4.1 Introduction

This chapter provides a description of the numerical approach to the problem.

Section 4.2 provides a general overview of the solution process. Complete details of the numerical aspects of this process are available in reference [28]. Section 4.3 provides a description of the features added to the code to facilitate the current study. These include the calculation of algebraic heat flux and fluctuating temperature variance, and a modified treatment of the energy equation.

4.2 Solution Strategy

4.2.1 General Conservation Equation

All of the dependent variables obey a generalized conservation principle. If the dependent variable is denoted by φ, the general differential equation is,

$$\frac{\partial}{\partial x} \left(u \, \Phi \right) + \frac{\partial}{\partial y} \left(v \, \Phi \right) = \frac{\partial}{\partial x} \left[\Gamma_{\Phi} \, \frac{\partial \Phi}{\partial x} \right] + \frac{\partial}{\partial y} \left[\Gamma_{\Phi} \, \frac{\partial \Phi}{\partial y} \right] + S_{\Phi} \tag{4.1}$$

where Γ is a diffusion coefficient. The terms on the left hand side represent convection of the dependent variable, while the first two terms on the right hand side are responsible for

diffusion. The final term, S_{φ} , is a general source term incorporated to include all other relevant processes.

The dimensionless governing equations (Equations (3.15) to (3.22)) can be expressed in this form using the values in Table 4.1.

ф	$\Gamma_{\!\scriptscriptstyle{f \Phi}}$	S_{ϕ}
ប	$\frac{a}{Re_l} + \frac{a}{Re_t}$	$\frac{\partial}{\partial X} \left[\left(\frac{a}{Re_I} + \frac{a}{Re_t} \right) \frac{\partial U}{\partial X} \right] + \frac{\partial}{\partial Y} \left[\left(\frac{a}{Re_I} + \frac{a}{Re_t} \right) \frac{\partial V}{\partial X} \right] - \frac{2}{3} \frac{\partial k^*}{\partial X}$
v	$\frac{a}{Re_t} + \frac{a}{Re_t}$	$\frac{\partial}{\partial X} \left[\left(\frac{a}{Re_l} + \frac{a}{Re_t} \right) \frac{\partial U}{\partial Y} \right] + \frac{\partial}{\partial Y} \left[\left(\frac{a}{Re_l} + \frac{a}{Re_t} \right) \frac{\partial V}{\partial Y} \right] + \frac{(Gr_y)_l a^2 \theta}{Re_l^2} - \frac{2}{3} \frac{\partial k^*}{\partial y}$
θ	<u>a</u> Re _l o _l	$-\frac{\partial}{\partial X}(\overline{u't'})^* - \frac{\partial}{\partial Y}(\overline{v't'})^*$
k*	$\frac{a}{Re_l} + \frac{a}{\sigma_k Re_t}$	$G^* - \varepsilon^* + \frac{a^2 (Gr_y)_l^2}{Re_l^2} (\overline{v^l t^l})^*$
ε*	$\frac{a}{Re_l} + \frac{a}{\sigma_e Re_t}$	$C_1 f_1 \frac{\varepsilon^*}{k^*} G^* - C_2 f_2 \frac{\varepsilon^{*2}}{k^*} + C_3 f_3 \frac{\varepsilon^*}{k^*} \frac{a^2 (Gr_y)_I^2}{Re_I^2} (\overline{v't'})^*$

Table 4.1: Governing Equations in General Form

The benefit of writing the governing equations in this manner is that it is only necessary to have an algorithm designed to solve Equation (4.1). This process can then be used repeatedly for various values of ϕ , Γ_{ϕ} , and S_{ϕ} .

4.2.2 Discretization of the Governing Equations

Discretization of the general conservation equation is accomplished using the control-volume approach described by Patankar [29]. The grid is staggered such that velocities are calculated on the control volume faces while pressure, temperature, and the other scalars are calculated at the centre of the control volume. This method prevents the occurrence of a 'checkerboard' distribution within the solution set.

To reduce the possibility of false diffusion, the Quadratic Upstream Interpolation for Convective Kinematics (QUICK) scheme is used to deal with the convective terms [28].

Following Patankar's nomenclature, individual source terms, S_n, are linearized as shown below:

$$S_C = S_n$$
, if $S_n \ge 0$
 $S_P = \frac{S_n}{\Phi}$, if $S_n < 0$ (4.2)

This linearization, in accordance with Patankar's recommendation, was found to provide greater stability as opposed to simply including the entire source in the constant term, S_C.

4.2.3 Solution Algorithm

The algorithm used to calculate the flow field is the Semi-Implicit Method for Pressure-Linked Equations Revised (SIMPLER) method. Complete details of this approach are available in [29].

The simultaneous equation sets are solved with the aid of the Modified Strongly Implicit Procedure. This method was found to provide more stability than the popular Alternating Direction Implicit (ADI) or Strongly Implicit Procedure (SIP) techniques [28].

4.3 Algebraic Heat Flux Model

4.3.1 Explicit Algebraic Heat Flux Calculation

The turbulent heat flux is calculated at interior grid points according to Equation (3.24) with one modification. To improve stability, the explicit heat flux formulation of Sommer and So [27] was incorporated. This method involves the use of a simple gradient diffusion approximation to the terms containing heat flux components within the heat flux equation as shown below,

$$(\overline{u'_{i}t'})^{*}_{AFM} = -\frac{Ck^{*}}{\varepsilon^{*}} \left[(\overline{u'_{i}u'_{j}})^{*} \frac{\partial \theta}{\partial X_{j}} + \xi (\overline{u'_{j}t'})^{*}_{SGD} \frac{\partial U_{i}}{\partial X_{j}} + \eta \frac{a^{2} (Gr_{i})_{l}}{Re_{l}^{2}} (\overline{t'^{2}})^{*} \right]$$

$$where \quad (\overline{u'_{j}t'})^{*}_{SGD} = \frac{a}{Re_{t}\sigma_{T}} \frac{\partial \theta}{\partial X_{j}}$$

$$(4.3)$$

Sommer and So point out that the implicit formulation given by Equation (3.24) can become singular and, therefore, unstable under certain conditions. While the explicit model is slightly less accurate from a physical standpoint, Sommer and So have obtained

results which support the use of this model.

4.3.2 Fluctuating Temperature Variance

The temperature variance is calculated either algebraically (Equation (3.28)) or from its transport equation (Equation (3.25)). The algebraic formulation works well and requires no special attention. The transport equation fits the general conservation form (Equation (4.1)) as shown below,

ф	$\Gamma_{\!\scriptscriptstylelack}$	S _¢
<u>t'2</u> *	$\frac{c_T k^{*2}}{\varepsilon^*} + \frac{a}{\sigma_l Re_l}$	$-2\left(\overline{u't'}\right)^*\frac{\partial\theta}{\partial X}-2\left(\overline{v't'}\right)^*\frac{\partial\theta}{\partial Y}-2\varepsilon_{\theta}^*$

Table 4.2: Dimensionless Temperature Variance in General Form

For convenience the diffusion coefficient was simplified,

$$\frac{c_T f_{\mu} k^{*2}}{\epsilon^*} = \frac{a}{Re_t \sigma_T} \qquad \text{where} \quad \sigma_T = \frac{C_{\mu}}{c_T}$$
 (4.4)

When the source terms were linearized according to the procedure given in Section 4.2.2, no difficulties were found when solving the temperature variance transport equation.

4.3.3 Modified Energy Equation Formulation

The energy equation (Equation (3.19)) requires a different treatment when the algebraic heat flux model is used. When the turbulent effects are represented by simple gradient diffusion, the energy equation fits the general conservation form without the need for source terms. With the algebraic flux model, a turbulent diffusion source term given by,

$$S_{\theta} = -\frac{\partial}{\partial X_i} \overline{u'_i t'} \tag{4.5}$$

must be incorporated as the diffusion coefficient, Γ , accounts only for the laminar effects (see Table 4.1).

To prevent the dimensionless temperature from acquiring erroneous values greater than one or less than zero, a special treatment of this source term is necessary. The procedure, shown below, is suggested by Patankar [29] as a solution to this problem,

$$S_{C} = \frac{S_{\theta} \theta^{*}}{\theta^{*} - \theta}$$

$$S_{P} = -\frac{S_{\theta}}{\theta^{*} - \theta}$$
(4.6)

where S_{θ} is the source term, θ is the current temperature, and θ^{\bullet} is defined as,

$$\theta^* = \frac{\theta}{2}, \qquad \text{for } S_{\theta} \le 0$$

$$\theta^* = \frac{\theta + 1}{2}, \qquad \text{for } S_{\theta} > 0$$
(4.7)

This provision ensures that the dimensionless temperature can move only halfway towards the physical limit within one iteration and, more importantly, can never exceed this physical limit.

CHAPTER FIVE

RESULTS AND DISCUSSION

5.1 Introduction

The present work is divided into three studies. The first study involves an examination of the sensitivity of the predicted results to the choice of inlet turbulence conditions. The second study deals solely with the effect of adding the algebraic heat flux model (AFM). The final study involves the incorporation of both factors and compares these final results to the experimental data.

5.2 Inlet Turbulent Viscosity Study

The effect of varied inlet eddy viscosity and turbulent length scale in conjunction with the low Reynolds number k- ϵ model was studied. This was accomplished through adjustment of the inlet dissipation of turbulent kinetic energy while holding the inlet turbulent intensity constant at 10%.

The corresponding dimensionless eddy viscosity and dimensionless turbulent length scale are calculated according to,

$$v^* = \frac{v_t}{v_l} = \frac{Re_D}{a} \frac{C_{\mu}k^{*2}}{\epsilon^*}$$
 (5.1)

$$l^* = \frac{l}{D} = \frac{1}{a} \frac{C_{\mu} k^{*\frac{3}{2}}}{\epsilon^*}$$
 (5.2)

The turbulent length scale, I, can be estimated based on the height of the inlet section, D. A dimensionless turbulence length scale, I*, of up to 10 % is considered reasonable whereas much larger values are generally unacceptable [30]. Within the course of this study the inlet turbulence conditions are specified such that the effect of a range of dimensionless turbulence length scales up to 60 % can be examined.

The effect of the inlet parameters on the predicted results will be discussed for each case independently, followed by some general comments on their selection when dealing with buoyant flows.

5.2.1 Case 1

Two sets of inlet conditions were chosen for this simpler, isothermal case. The purpose of the study is to determine the effect of increasing the inlet length scale to a larger, but still realistic, value when dealing with isothermal flow conditions. The conditions and predicted dimensionless separation heights are summarized in Table 5.1.

Test	k* _{in}	ε* _{in}	$v_{t}^{*}_{in}$	1*	Separation
1 (a)	.015	1.15	0.0467	0.000393	0.33
1 (b)	.015	0.08	6.311	0.0531	0.16

Table 5.1 - Inlet Viscosity Study (Case 1)

Figure 5.1 compares the predicted streamlines for the two tests while Figure 5.2 presents turbulent viscosity contours. Although the streamlines are qualitatively similar, the reduced inlet dissipation rate (with inlet length scale of approximately 5 %) results in a lower separation location on the right wall and further penetration along the top wall. The turbulent viscosity contours are very similar except in the inlet region where the reduced dissipation rate test shows significantly higher levels. The effect of the varied inlet turbulent conditions on the midheight turbulent viscosity profile is minimal as shown in Figure 5.3.

The important result is the significant decrease in separation height as the result of increasing the inlet turbulent length scale. This effect can be attributed to an increase in mean flow momentum resulting when the dissipation rate, which removes energy from the mean flow, is reduced.

5.2.2 Case 2

Four inlet dissipation levels were examined in conjunction with Case 2. The inlet turbulence parameters and the predicted dimensionless separation heights are summarized below in Table 5.2. A large range of dimensionless length scales were employed for this

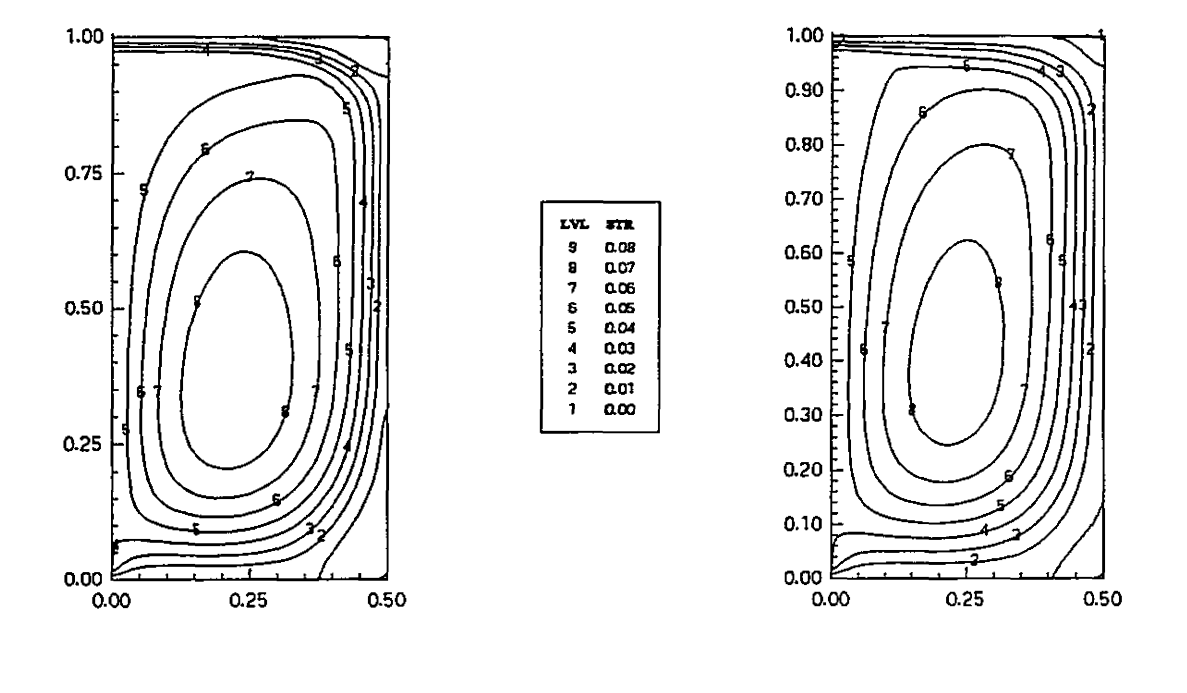
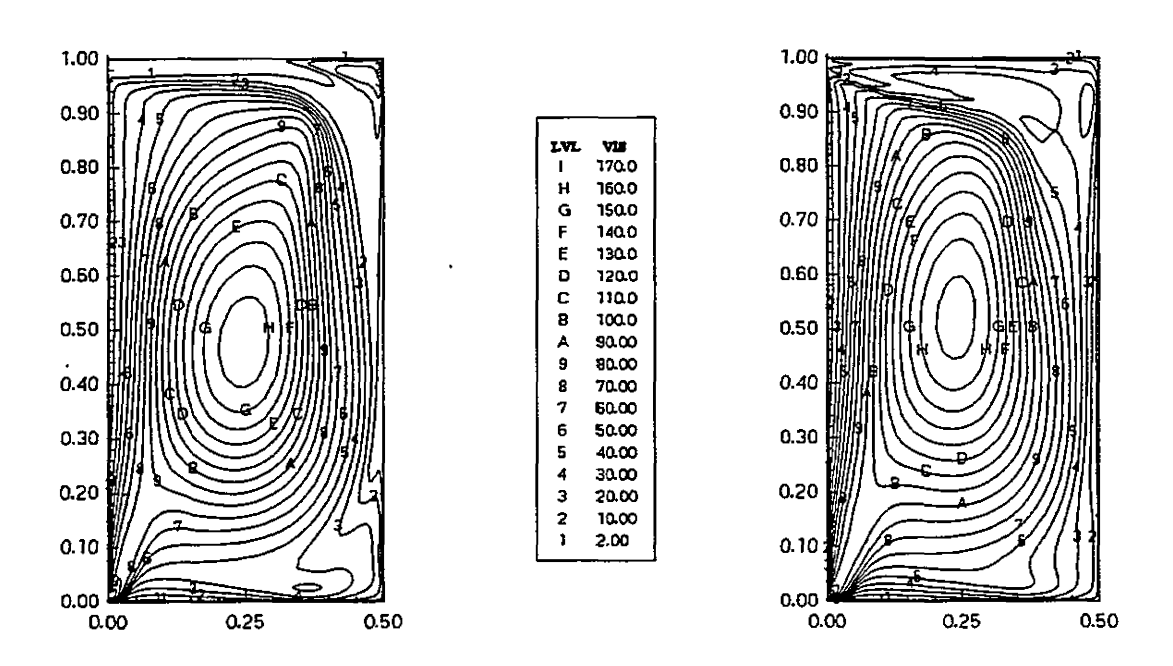


Figure 5.1 - Inlet Viscosity Study (Case 1): Streamlines



Test 1 (a)

Test 1 (a)

Test 1 (b)

Test 1 (b)

Figure 5.2 - Inlet Viscosity Study (Case 1): Turbulent Viscosity Contours

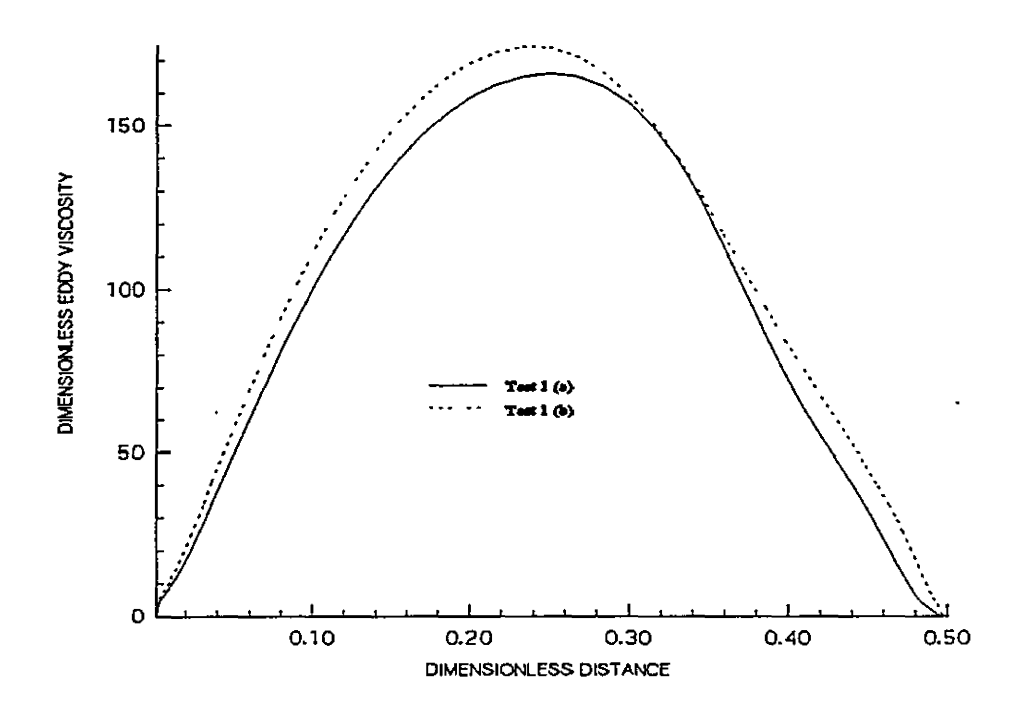


Figure 5.3 - Inlet Viscosity Study (Case 1): Turbulent Viscosity Profile (Y = 0.5)

case. Test 2 (d) involves a physically unrealistic value of approximately 60 % leading to flow separation along the top horizontal wall.

Test	k* _{in}	ε* _{in}	$v_{t in}^*$	1* _{in}	Separation
2 (a)	0.015	1.15	0.075	0.000477	0.7478
2 (b)	0.015	0.09	7.97	0.0507	0.7596
2 (c)	0.015	0.05	17.09	0.109	0.7673
2 (d)	0.015	0.01	95.80	0.611	0.3377 (pen)

Table 5.2 - Inlet Viscosity Study (Case 2)

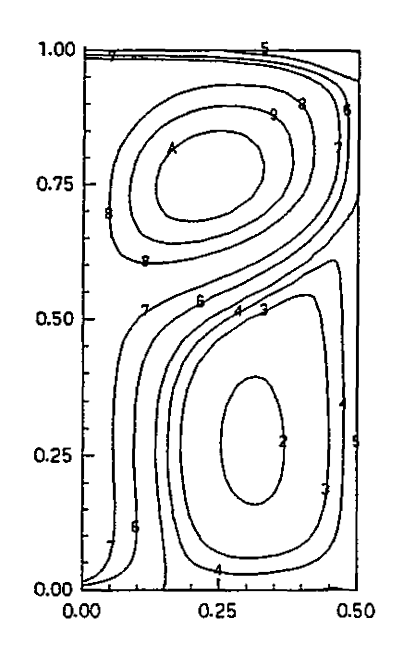
Predicted streamlines for Tests 2 (a), 2 (b), and 2 (d) are presented in Figure 5.4, while turbulent viscosity contours are compared in Figure 5.5.

The streamline plots show slight increases in separation point location with corresponding increases in inlet turbulent viscosity. Test 2 (d), with the highest level of inlet turbulent viscosity, predicts a flow pattern where the inlet jet does not even reach the heated wall.

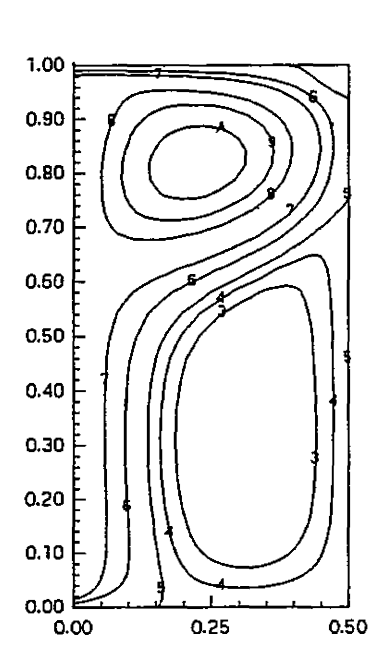
Figure 5.6 shows profiles of turbulent viscosity at the cavity midheight. While the profiles exhibit similar shapes, significant increases in magnitude occur throughout the cavity as the inlet turbulent viscosity is increased. This result is consistent with Figure 5.5 showing turbulent viscosity contours.

This increase in inlet turbulent viscosity leads to increased heat transfer at the hot wall as shown in Figure 5.7. Test 2 (d), having the highest level of inlet turbulent

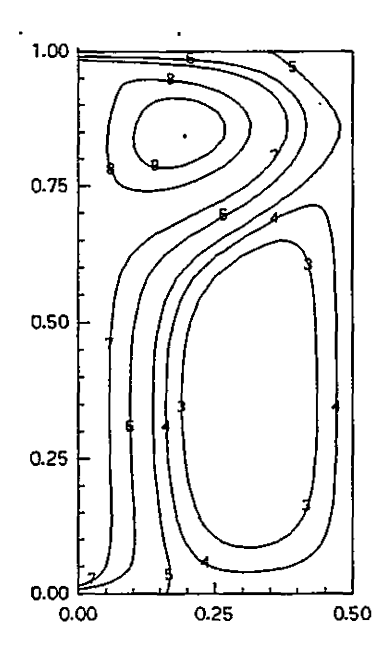
LVL	STR
В	0.07
Α	0.06
9	0.05
8	0.04
7	0.02
6	0.01
5	0.00
4	-0.00
3	-0.01
2	-0.02
1	-0.03



Test 2 (a)

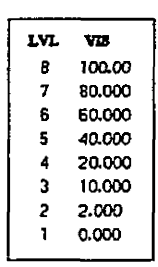


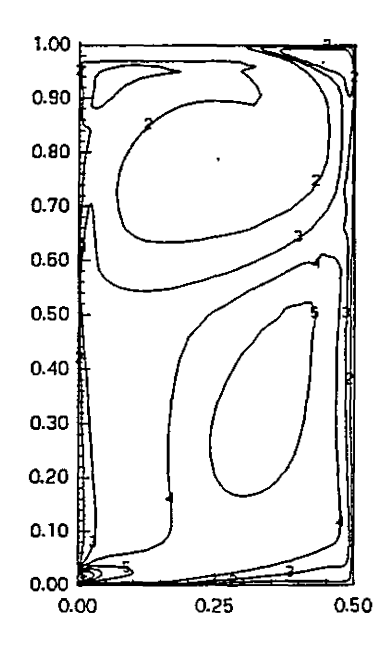
Test 2 (b)



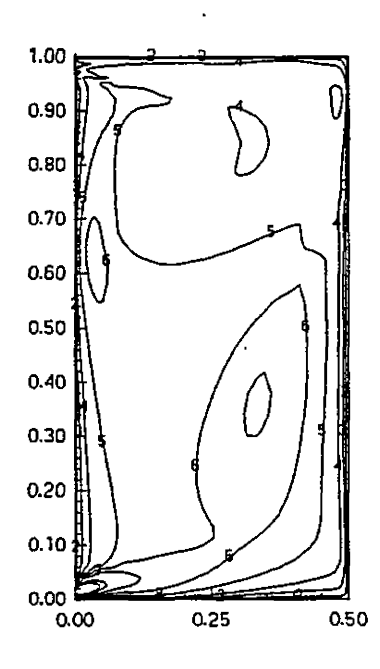
Test 2 (d)

Figure 5.4 - Inlet Viscosity Study (Case 2): Streamlines

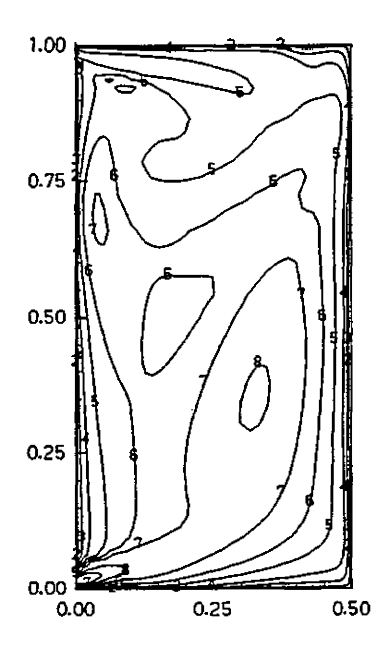




Test 2 (a)



Test 2 (b)



Test 2 (d)

Figure 5.5 - Inlet Viscosity Study (Case 2): Turbulent Viscosity Contours

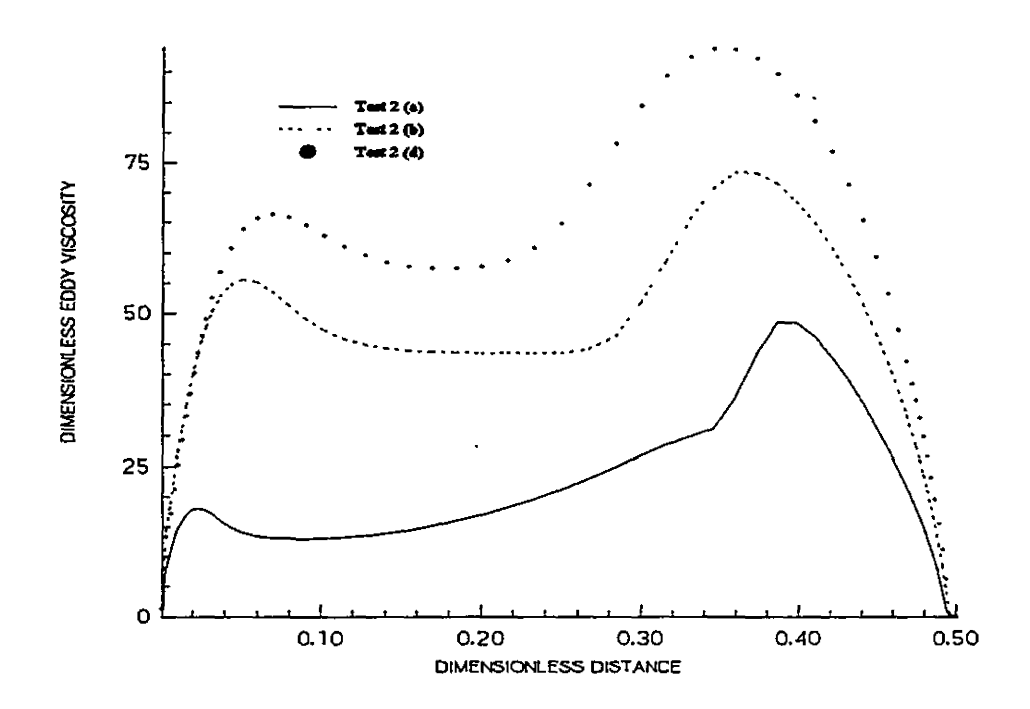
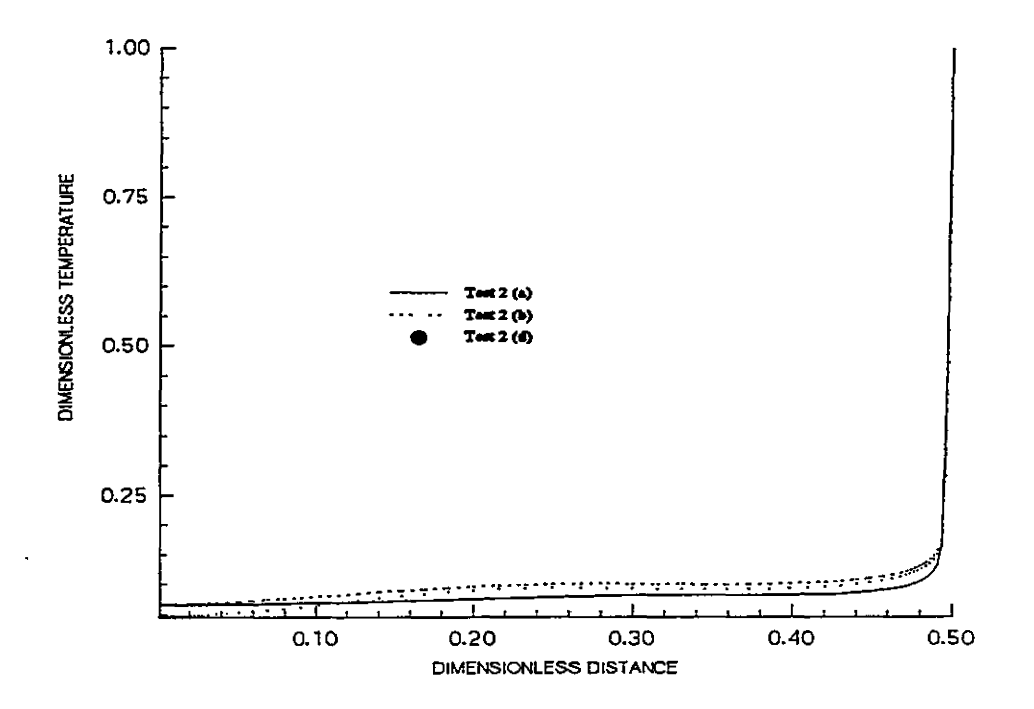


Figure 5.6 - Inlet Viscosity Study (Case 2): Turbulent Viscosity Profile (Y=0.5)



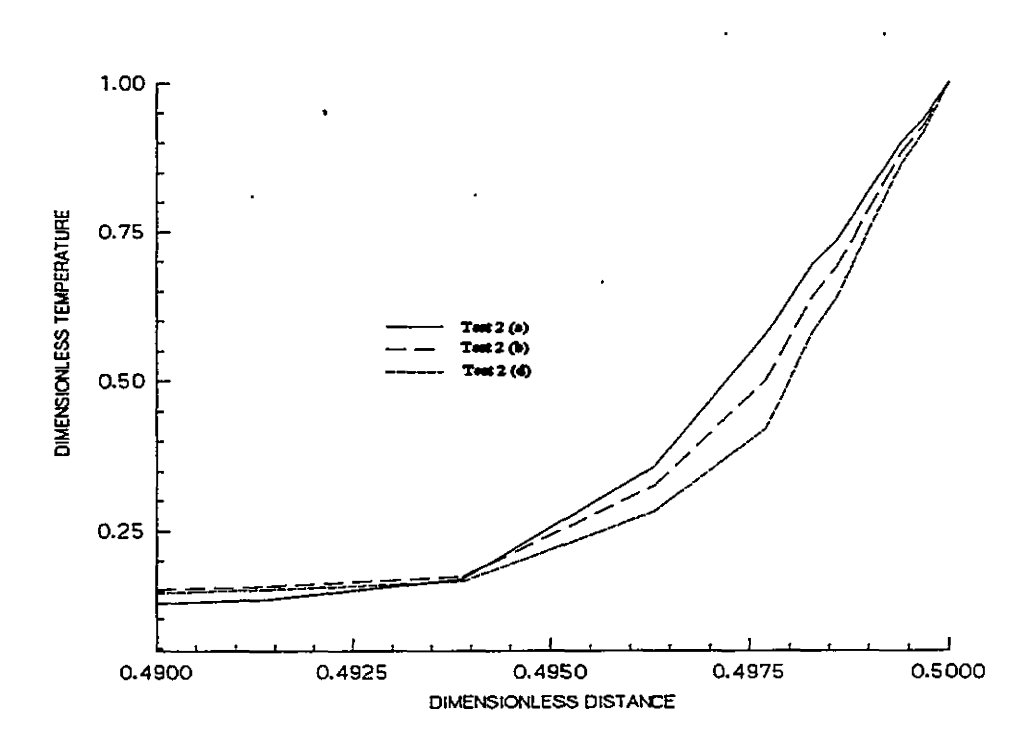


Figure 5.7 - Inlet Viscosity Study (Case 2): Temperature Profiles (Y=0.5)

viscosity, has the steepest temperature gradient and therefore, the highest heat transfer rate. This results in an increased buoyant force which translates to additional vertical momentum and a higher separation point.

5.2.3 Case 3

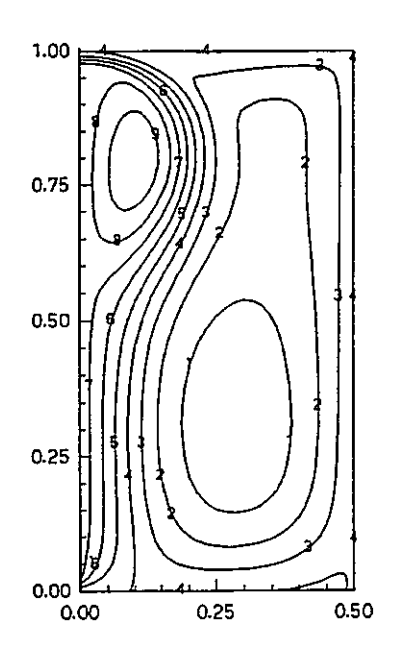
Seven sets of inlet conditions were tested for this case. These conditions and the corresponding predicted penetration depths are listed below in Table 5.3.

Test	k* _{in}	ε* _{in}	$v_{t}^{*}_{in}$	1* _{in}	Penetration
3 (a)	0.015	1.15	0.0347	0.000350	0.03030
3 (b)	0.015	0.30	0.402	0.00407	0.2380
3 (c)	0.015	0.20	0.904	0.00915	0.3744
3 (d)	0.015	0.10	3.28	0.0332	0.3569
3 (e)	0.015	0.075	5.26	0.0531	0.3539
3 (f)	0.015	0.050	9.50	0.0959	0.3502
3 (g)	0.015	0.010	59.8	0.605	0.3279

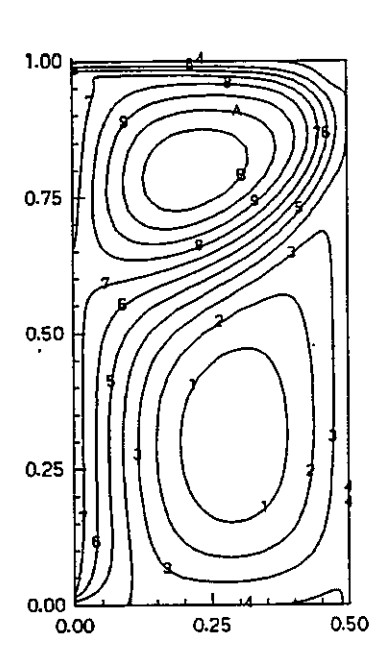
Table 5.3 - Inlet Viscosity Study (Case 3)

The predicted penetration depths are quite sensitive to the choice of inlet dissipation rate. As the inlet dissipation is decreased from the original level of 1.15 to 0.20 the fluid penetrates further into the cavity, nearly coming into contact with the heated wall. However, further decreases in the inlet dissipation rate result in a slight regression of

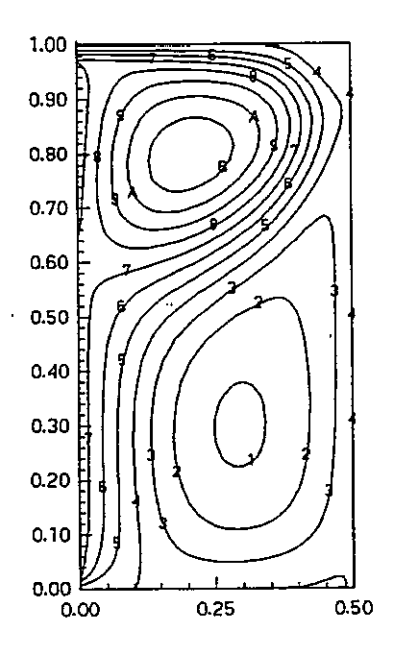
LVL	STR.
В	0.07
Α	0.06
9	0.05
8	0.04
7	0.03
6	0.02
5	0.01
4	0.00
3	-0.01
2	-0.02
1	-0.03



Test 3 (a)



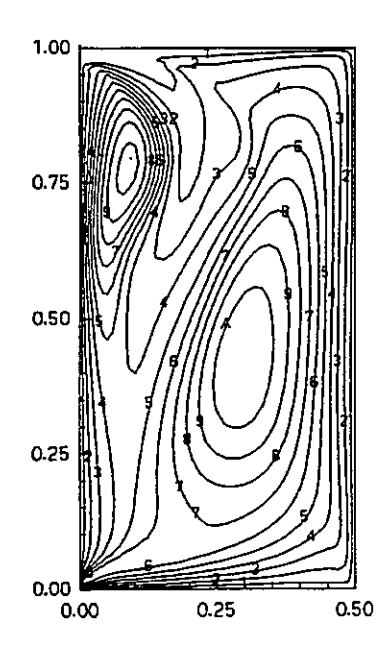
Test 3 (c)



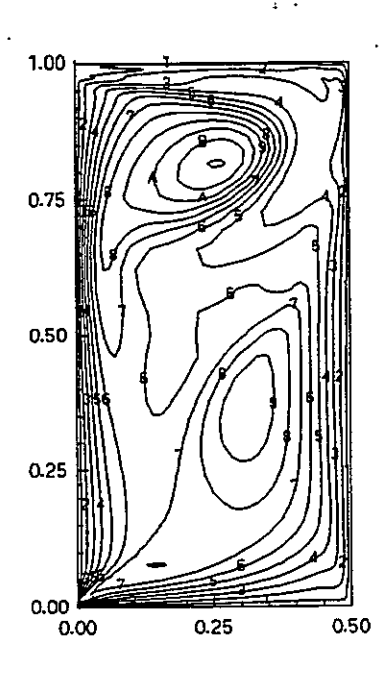
Test 3 (g)

Figure 5.8 - Inlet Viscosity Study (Case 3): Streamlines

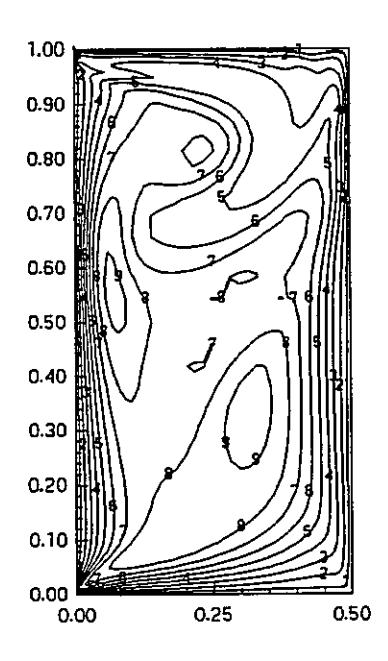
LVL	VIS
С	110.0
В	100.0
Α	90.00
9	80.00
8	70.00
7	60.00
6	50.00
5	40.00
4	30.00
3	20.00
2	10.00
1	2.00



Test 3 (a)

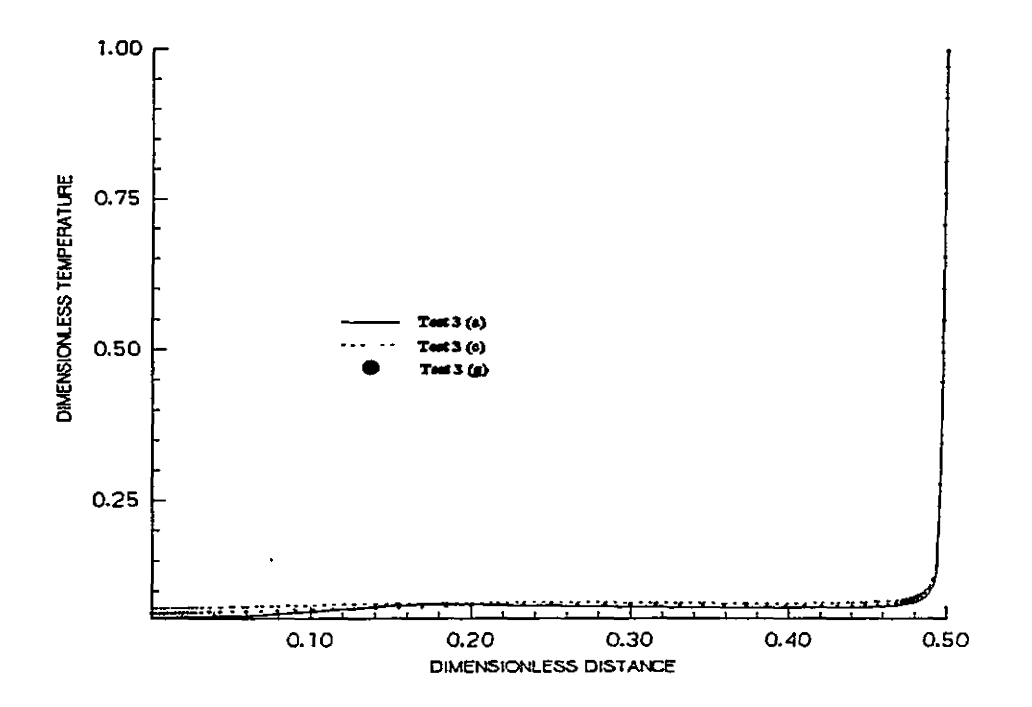


Test 3 (c)



Test 3 (g)

Figure 5.9 - Inlet Viscosity Study (Case 3): Turbulent Viscosity Contours



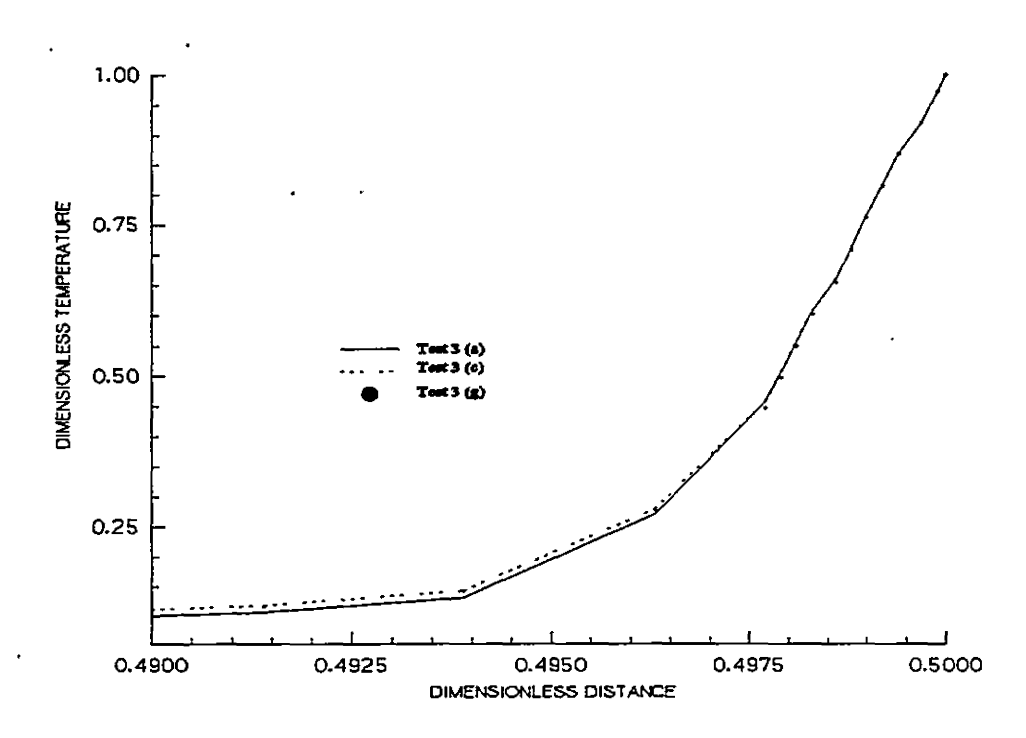


Figure 5.10 - Inlet Viscosity Study (Case 3): Temperature Profile (Y=0.5)

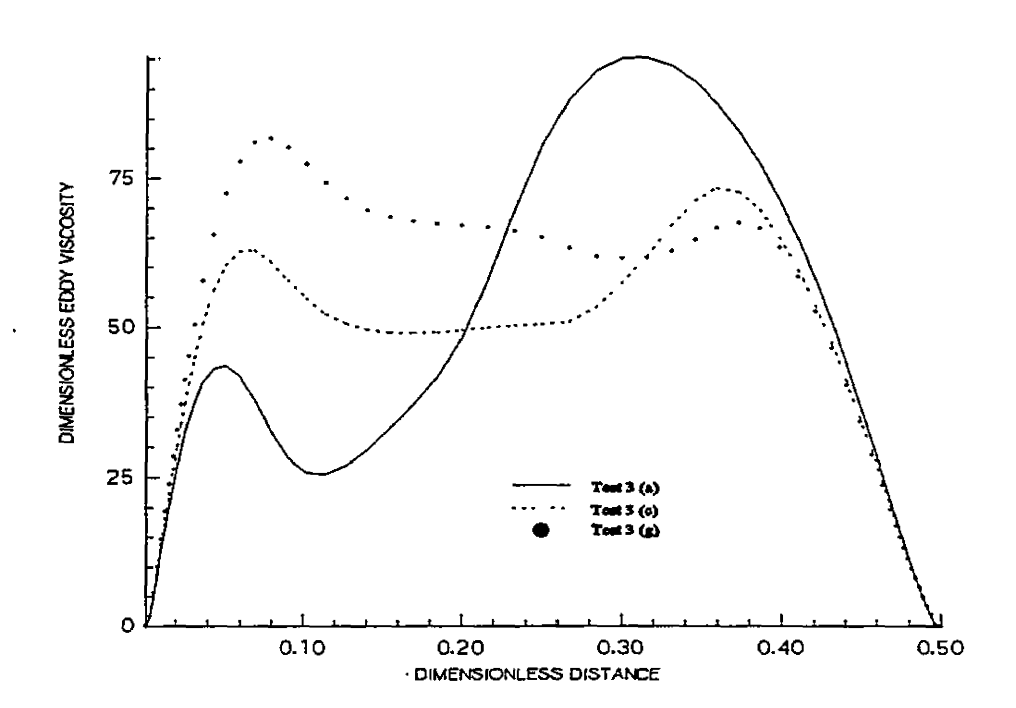


Figure 5.11 - Inlet Viscosity Study (Case 3): Turbulent Viscosity Profile (Y=0.5)

this penetration depth.

Figures 5.8 and 5.9 show streamline plots and turbulent viscosity contours for Tests 3 (a), 3 (c), and 3 (g). When the inlet dissipation rate is decreased from the original level of 1.15 (Tests 3 (c) and 3 (g)), the predictions become more representative of the mixed flow conditions involved as two similarly-sized cells, rotating in opposite directions, are formed.

Figure 5.10 shows temperature profiles at the cavity midheight. The profiles are surprisingly similar but the significance of any comparison involving Test 3 (a) is questionable due to the substantial difference in the predicted flow field. The results do show a slightly steeper temperature gradient and higher core temperature for Test 3 (g), which has the minimum inlet dissipation rate, when compared to Test 3 (c).

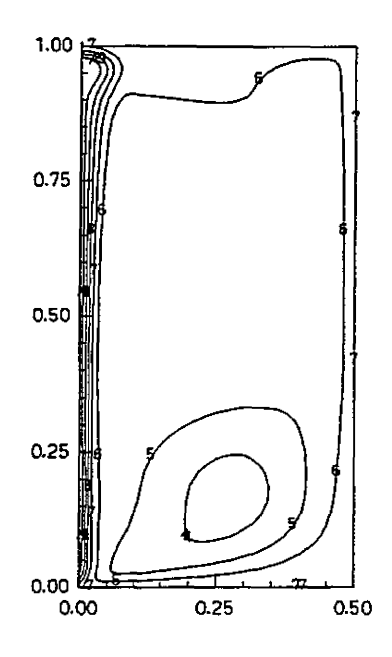
Apparently, two effects related to the inlet turbulence conditions contribute to the penetration of the fluid into the cavity. As the inlet dissipation rate is initially reduced, the extended penetration into the cavity can be attributed to additional mean flow momentum due to the smaller energy losses as evidenced in Case 1, while the slight regression of this penetration depth is the result of increased buoyancy due to a slightly higher heat transfer rate. This effect was found to be dominant in Case 2.

5.2.4 Case 4

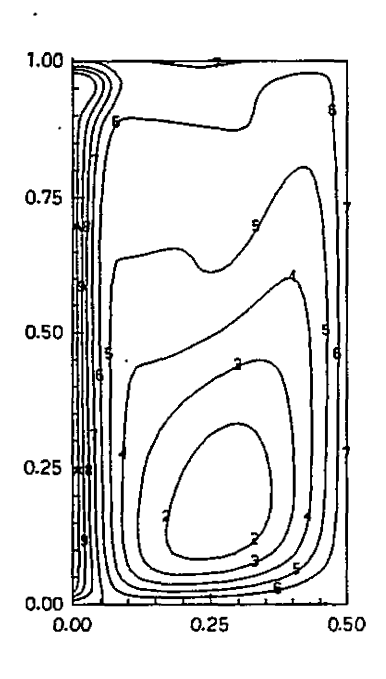
Three sets of inlet turbulence conditions were tested in conjunction with Case 4.

The test cases and corresponding penetration depths are shown in Table 5.4.

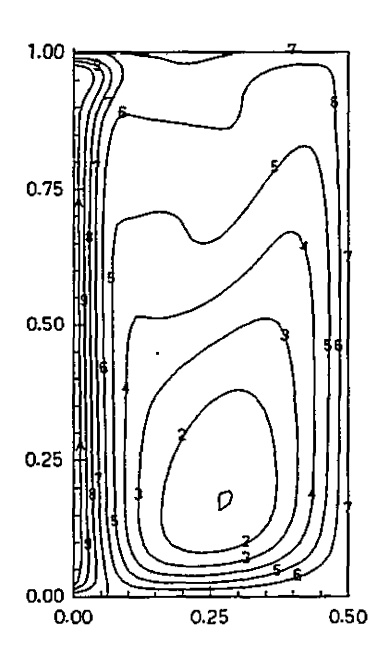
LVL	STR
В	0.04
Α	0.03
9	0.02
8	0.01
7	0.00
6	-0.01
5	-0.02
4	-0.03
3	-0.04
2	-0.05
1	-0.05



Test 4 (a)



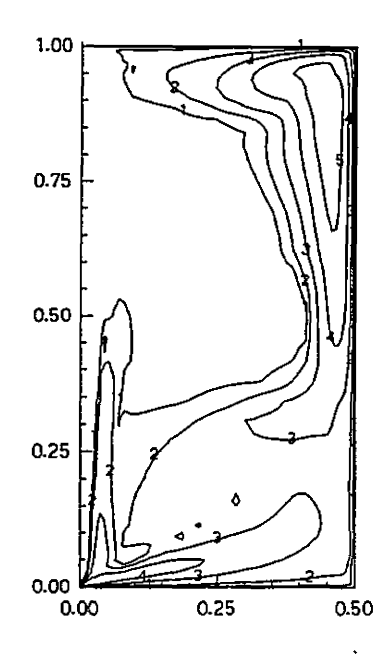
Test 4 (b)



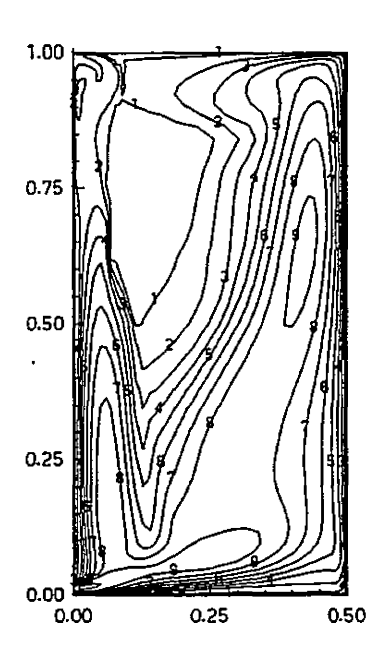
Test 4 (c)

Figure 5.12 - Inlet Viscosity Study (Case 4): Streamlines

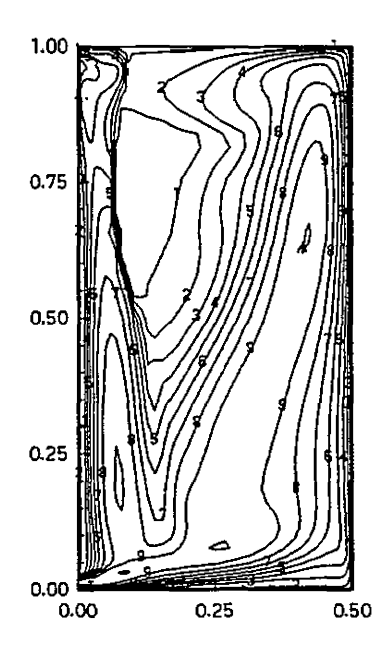
B 100.0 A 90.00 9 80.00 7 60.00 6 50.00 5 40.00 4 30.00 3 20.00 2 10.00 1 2.00



Test 4 (a)

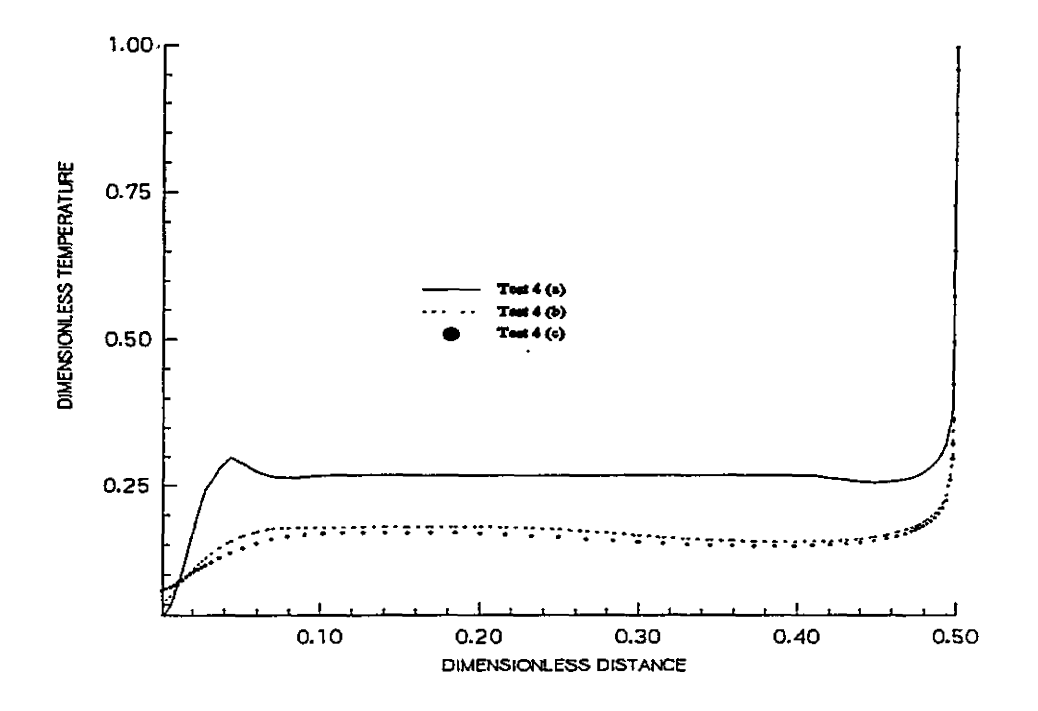


Test 4 (b)



Test 4 (c)

Figure 5.13 - Inlet Viscosity Study (Case 4): Turbulent Viscosity Contours



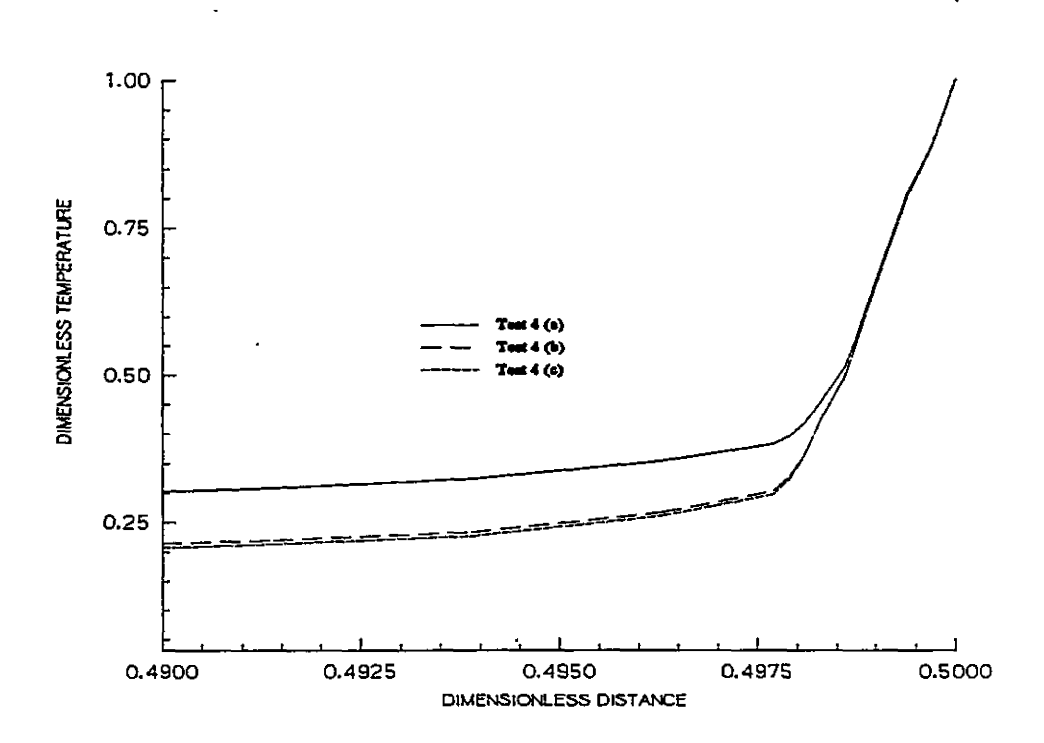


Figure 5.14 - Inlet Viscosity Study (Case 4): Temperature Profile (Y = 0.5)

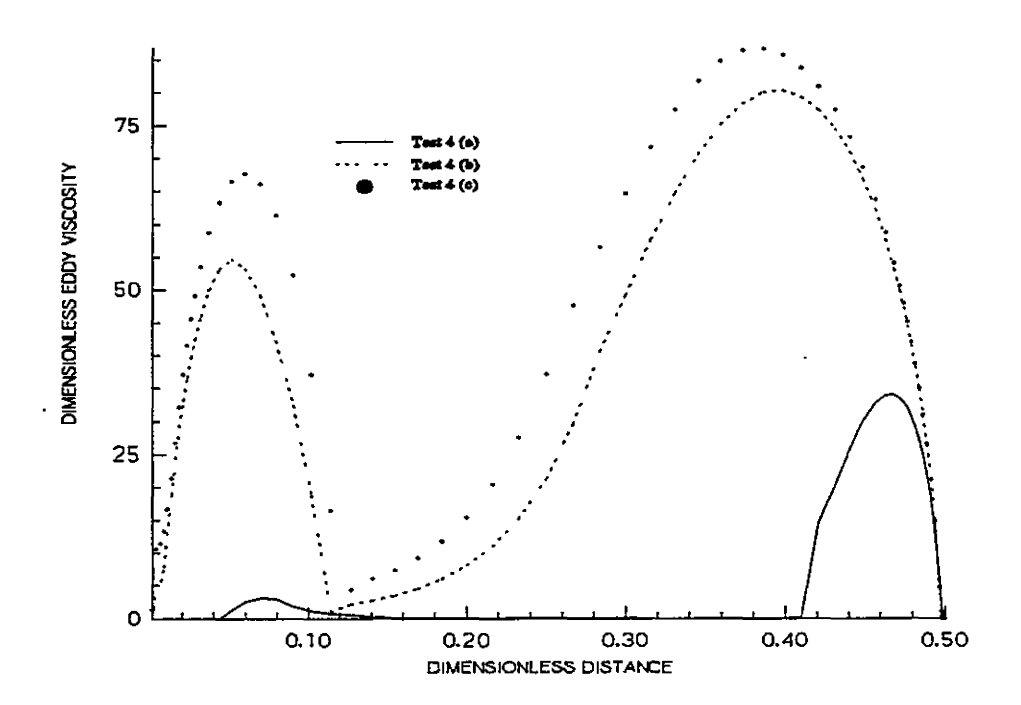


Figure 5.15 - Inlet Viscosity Study (Case 4): Turbulent Viscosity Profile (Y=0.5)

Test	k* _{in}	ε* _{in}	$v_{\rm t}^*$	1* _{in}	Penetration
4 (a)	0.015	1.15	0.0450	0.000387	0.0178
4 (b)	0.015	0.09	5.0910	0.0438	0.0229
4 (c)	0.015	0.01	70.635	0.607	0.0471

Table 5.4 - Inlet Viscosity Study (Case 4)

As shown above, the penetration depth of the fluid increases slightly as the inlet dissipation rate is decreased. Figures 5.12 and 5.13 show the streamline and turbulent viscosity plots, respectively. The streamline plots show increased buoyant recirculation as the inlet turbulent viscosity is initially increased. This effect is the result of increased heat transfer rates due to higher levels of turbulent viscosity throughout the cavity. Further increases in inlet turbulent viscosity leads to similar results.

Figure 5.14 shows dimensionless temperature profiles at the midheight of the cavity. The profiles for Tests 4 (b) and 4 (c) are also very similar. Again, it is difficult to make comparisons between Test 4 (a) and the other cases because of the differences in the predicted flow fields.

Figure 5.15 shows turbulent viscosity profiles at the cavity midheight. Once again, significant increases in turbulent viscosity levels arise in the reduced inlet dissipation test cases.

5.2.5 Inlet Viscosity Study Summary

The purpose of this study was to determine the sensitivity of the results to changes in inlet turbulence parameters. While many researchers select these values without reporting or even conducting a sensitivity analysis, the results have shown that modification of these quantities within reasonable limits can have a significant effect when dealing with this type of flow.

For this mixed-convection study, changes to the inlet rate of dissipation has two noticeable effects. The first involves an additional source of mean flow momentum resulting from reduced turbulent energy losses. This leads to further penetration into the cavity towards the heated wall. The second effect involves increases in the vertical buoyant force near the heated wall due to higher levels of turbulent viscosity which seems to diffuse throughout the cavity when the inlet dissipation rate is reduced. This leads to higher separation heights along the heated wall. Although both effects are present in all cases involving heat transfer, the first effect was generally prevalent in Case 3 while the second effect dominated Case 2. Such behaviour could be a function of inlet Reynolds number as Case 3 has a lower inlet jet velocity than Case 2. It could be that a decreased inlet dissipation rate does not have as great an effect on the mean flow momentum for higher Reynolds number or more turbulent flows.

5.3 Algebraic Flux Model (AFM) Study

The effect of adding the algebraic heat flux model to the existing k- ε equations was studied. The original simple gradient diffusion (SGD) representation for the turbulent heat

flux components is given by,

$$(\overline{u'_i t'})^* = -\frac{a}{Re_T} \frac{\partial \theta}{\partial X_i}$$
 (5.3)

while the algebraic heat flux is given by,

$$(\overline{u'_{i}t'})^{*} = -\frac{Ck^{*}}{\varepsilon^{*}} \left[(\overline{u'_{i}u'_{j}})^{*} \frac{\partial \theta}{\partial X_{k}} + \xi (\overline{u'_{j}t'})^{*} \frac{\partial U_{i}}{\partial X_{j}} + \eta \frac{a^{2}(Gr_{i})_{l}}{Re_{l}^{2}} (\overline{t'^{2}})^{*} \right]$$
(5.4)

where C, η , ξ are constants. The fluctuating temperature variance was also evaluated algebraically, according to,

$$(\overline{t'^2})^* = -2R \frac{k^*}{\varepsilon^*} (\overline{u'_j t'})^* \frac{\partial \theta}{\partial X_j}$$
 (5.5)

where time-scale ratio R is constant.

The constants η , ξ were assumed to have a value of 0.6. This value is commonly used within the literature although some researchers have employed a value of 0.5 [21,8]. Selection of the constants C and R has been much more controversial and problem-dependent. For the purpose of this study, two values of C were employed, 0.28 and 0.10. These values represent the range of values reported in the literature. A constant value of 0.5 was chosen for the time-scale ratio R. In some tests, this value was modified and will be mentioned when appropriate.

Studies were conducted for each of the cases involving heat transfer. The effect of the AFM model on the predicted streamlines, turbulent heat flux, temperature and turbulent viscosity distributions will be discussed.

It should be noted that the inlet turbulence conditions were held constant for this particular study. The inlet turbulent intensity was set at 10% and the dimensionless inlet dissipation rate was defined as 1.15. The inlet length scale and turbulent viscosity are dependent on Reynolds number and therefore vary for each case. These values are available in the inlet viscosity study (Section 5.2).

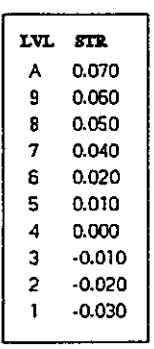
5.3.1 Case 2

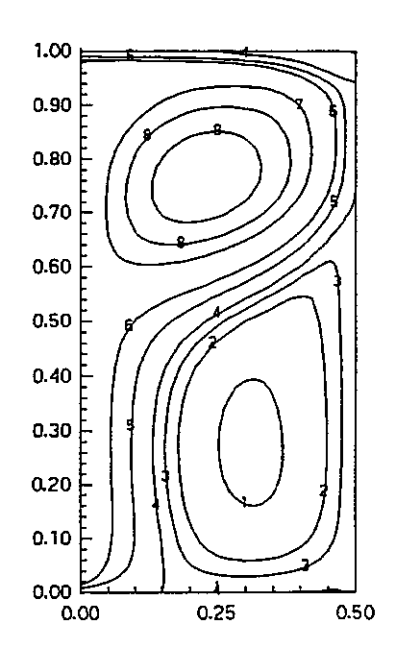
Figure 5.16 shows the predicted streamlines for the AFM study, while separation locations are presented in Table 5.5.

Model	Model Constant C	Separation Height
SGD ,	-	.7478
AFM	0.28	.7108
AFM	0.10	.7242

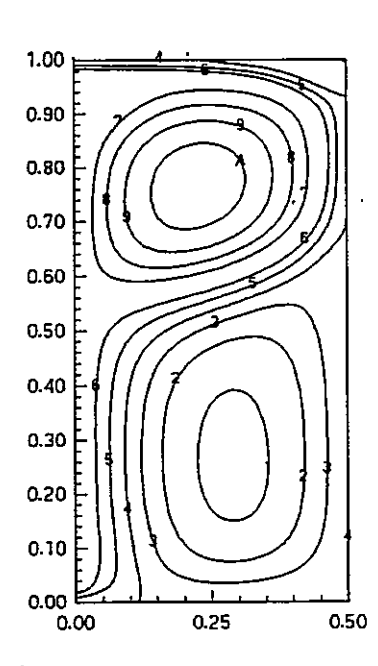
Table 5.5 - AFM Study (Case 2)

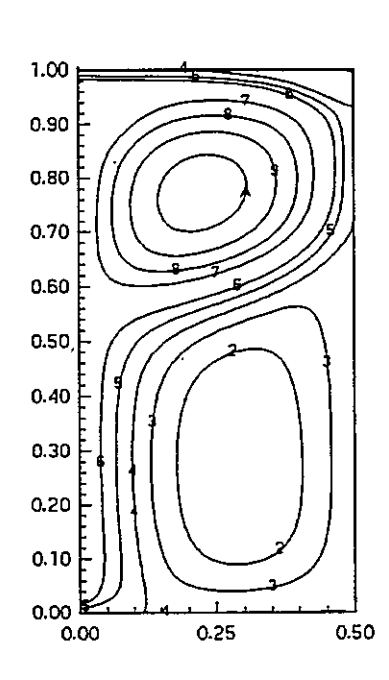
Although only small differences arise when the algebraic flux model is employed, a few interesting trends are apparent. It was expected that the use of the AFM model would lead to higher rates of heat transfer, and, therefore, more buoyant flow and higher separation locations. The results show a slightly decreased separation location when the flux model, with C=0.28, is employed. Furthermore, the use of a decreased model constant (C=0.10) leads to a small increase in separation location.





SGD Model

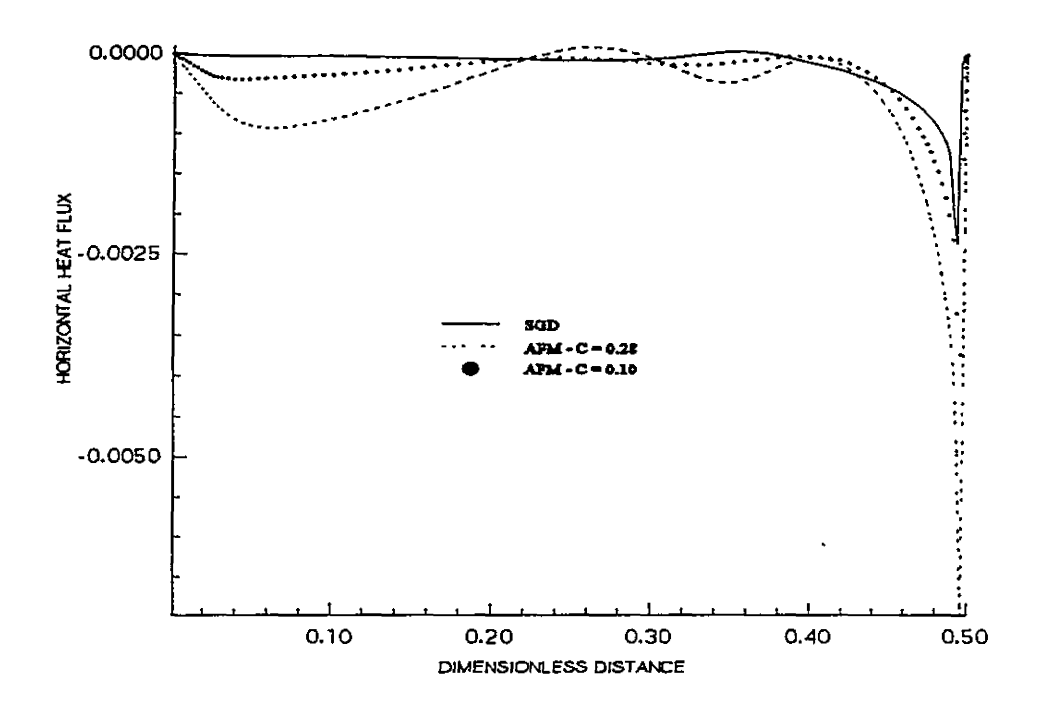




AFM - C=.28

AFM - C=.10

Figure 5.16 - AFM Study (Case 2): Streamlines



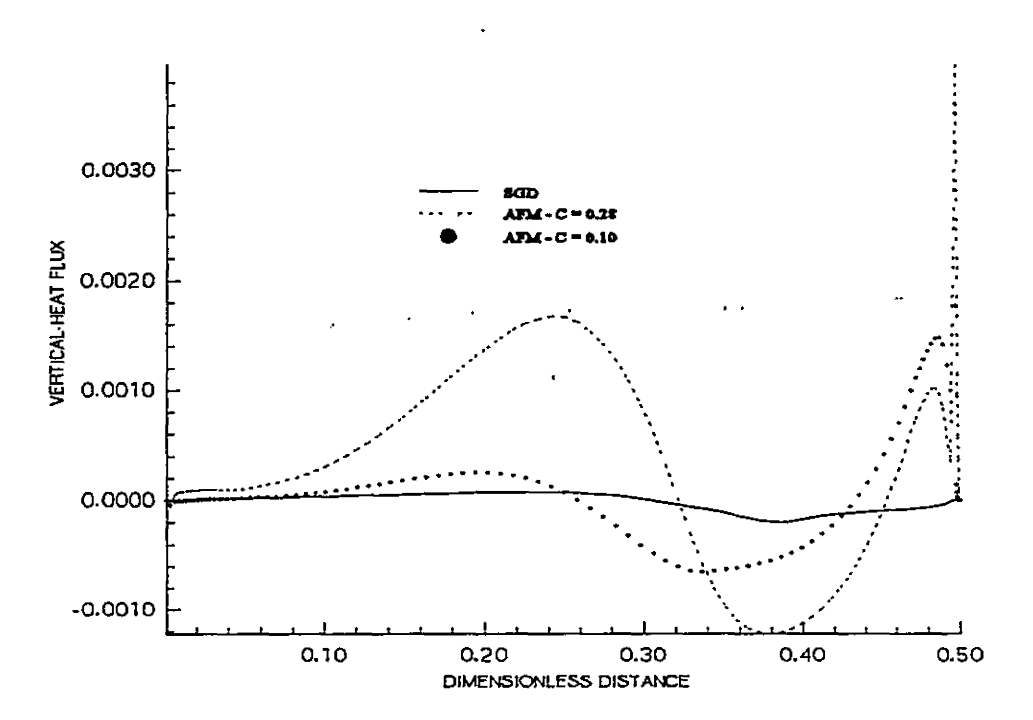
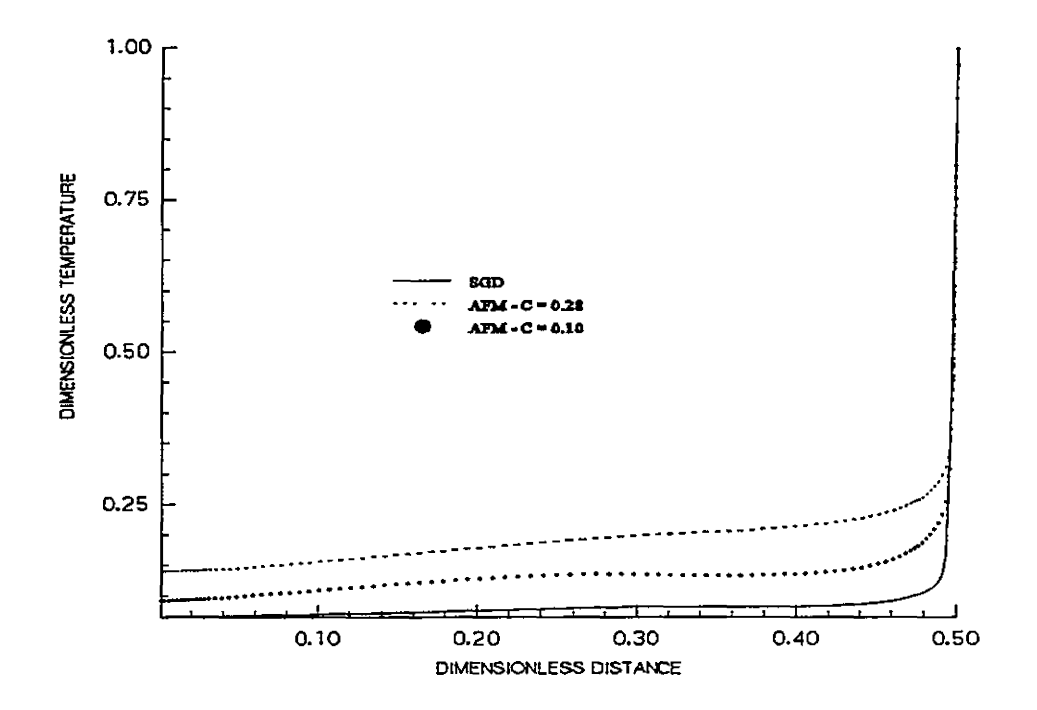


Figure 5.17 - AFM Study (Case 2): Turbulent Heat Flux Profiles (Y=0.5)



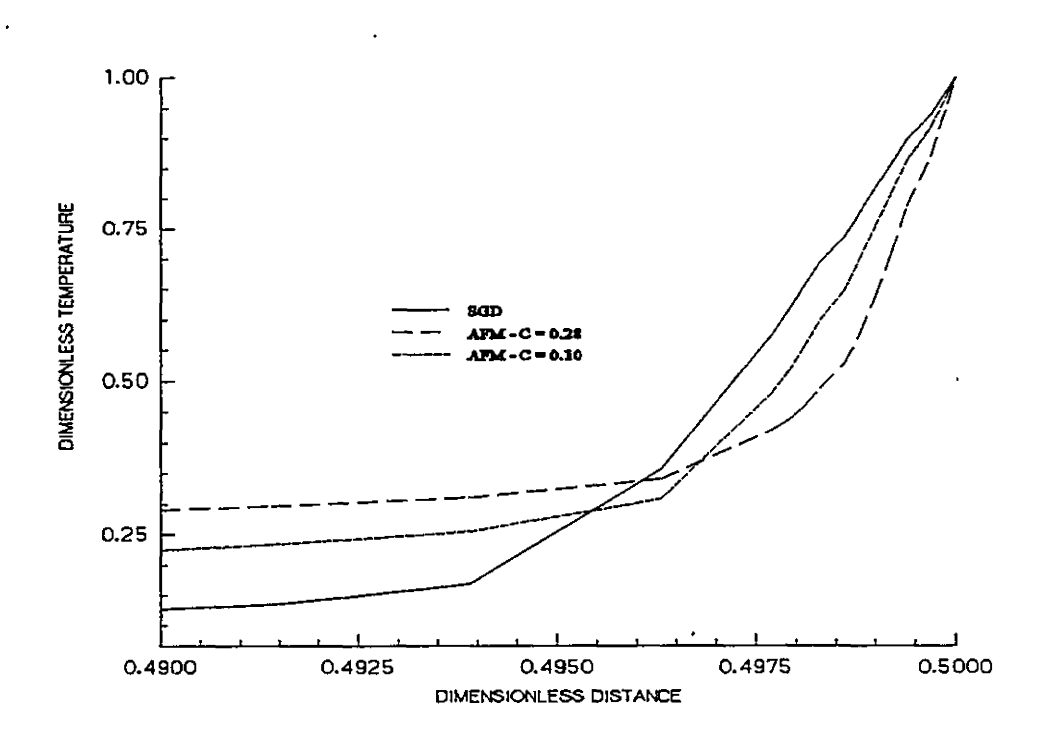


Figure 5.18 - AFM Study (Case 2): Dimensionless Temperature Profiles (Y=0.5)

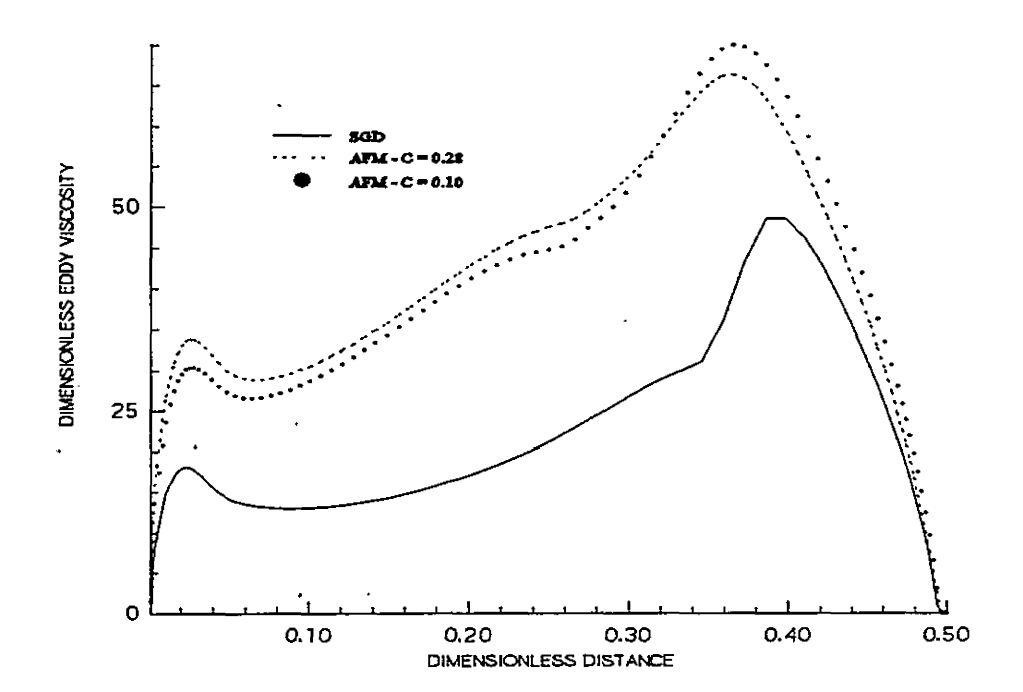


Figure 5.19 - AFM Study (Case 2): Turbulent Viscosity Profiles (Y=0.5)

Figure 5.17 shows turbulent heat flux profiles at the midheight of the cavity. Use of the AFM model leads to significantly higher levels, especially for the vertical heat flux. The heat transfer rate, although predominantly controlled by the horizontal gradient of the horizontal turbulent heat flux, should increase under these conditions. Figure 5.18 shows the dimensionless temperature distribution at the cavity midheight. As expected, the AFM model, with C=0.28, results in the steepest temperature gradient and, therefore, the highest rate of heat transfer. The increased vertical turbulent heat flux also leads to higher levels of turbulent viscosity due to the buoyant source term appearing in the k and ε equations. This effect is illustrated in Figure 5.19.

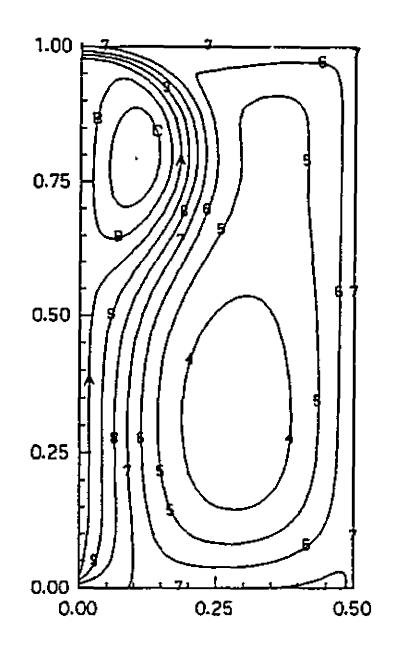
Although the separation location decreases slightly when the AFM model is employed, the width of the buoyant cell increases, as does the strength of recirculation. These results are consistent with increased heat transfer resulting from higher levels of turbulent heat flux. It is expected that further increases in heat transfer rate would result in corresponding increases in separation location.

5.3.2 Case 3

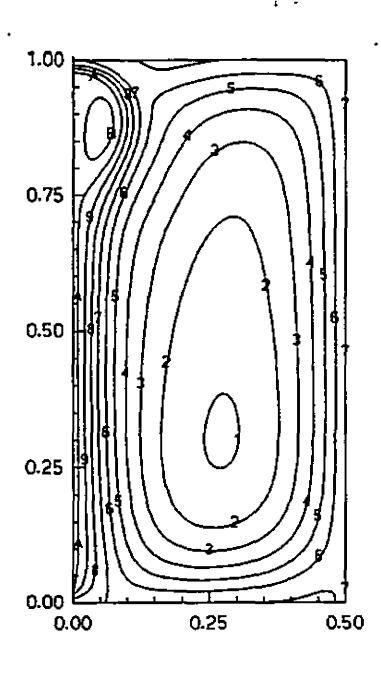
Figure 5.20 shows the predicted streamlines for Case 3. Use of the AFM model results in increased buoyant recirculation as the fluid is driven back closer to the inlet.

Predicted penetration depths are shown in Table 5.6. As expected, the effect is more exaggerated for C=0.28 than for C=0.10.

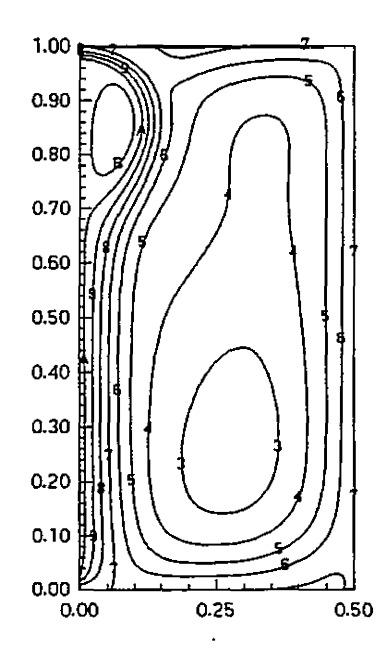
LVL	STR
D	0.06
C	0.05
В	0.04
A	0.03
9	0.02
8	0.01
7	0.00
6	-0.01
5	-0.02
4	-0.03
3	-0.04
2	-0.05
1	-0.06



SGD Model

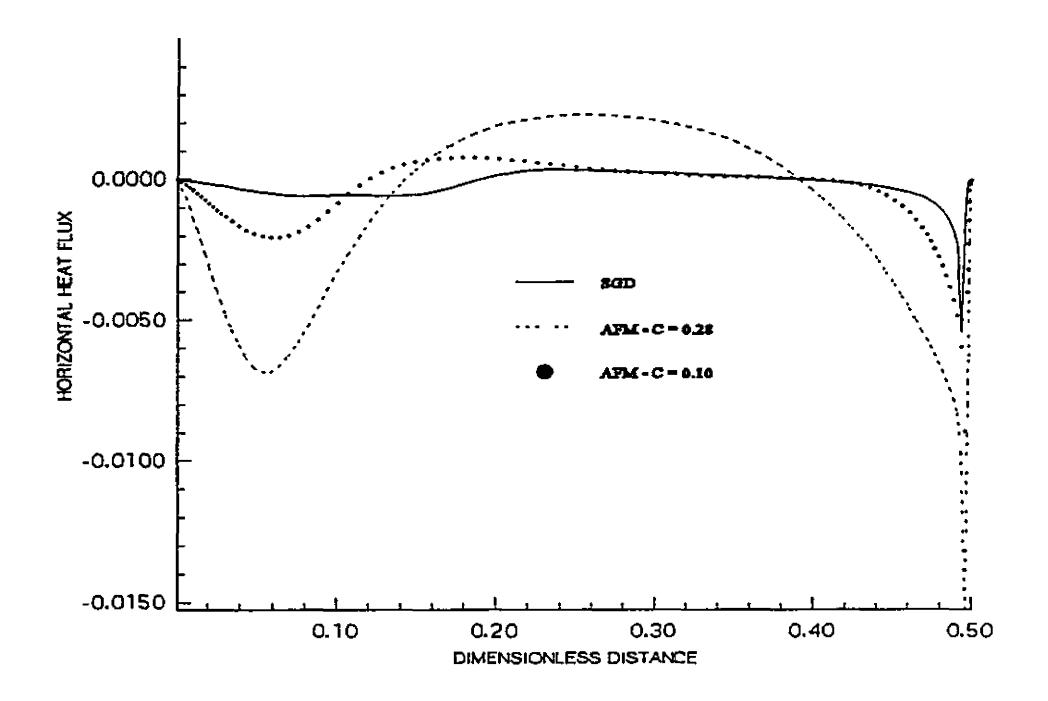


AFM - C = 0.28



AFM - C = 0.10

Figure 5.20 - AFM Study (Case 3): Streamlines



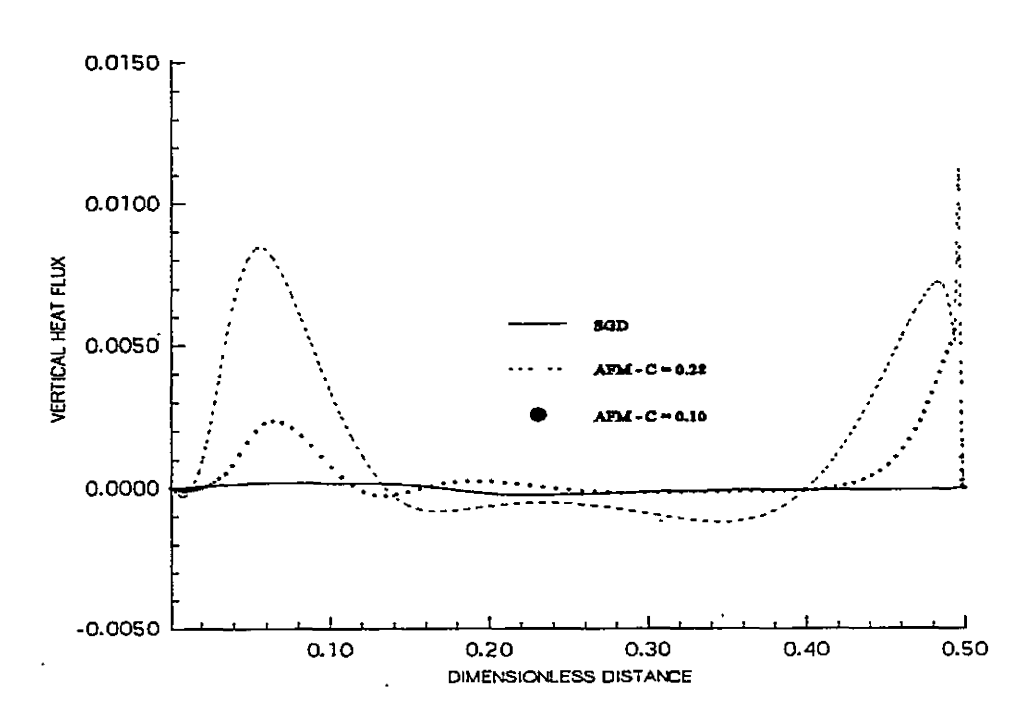
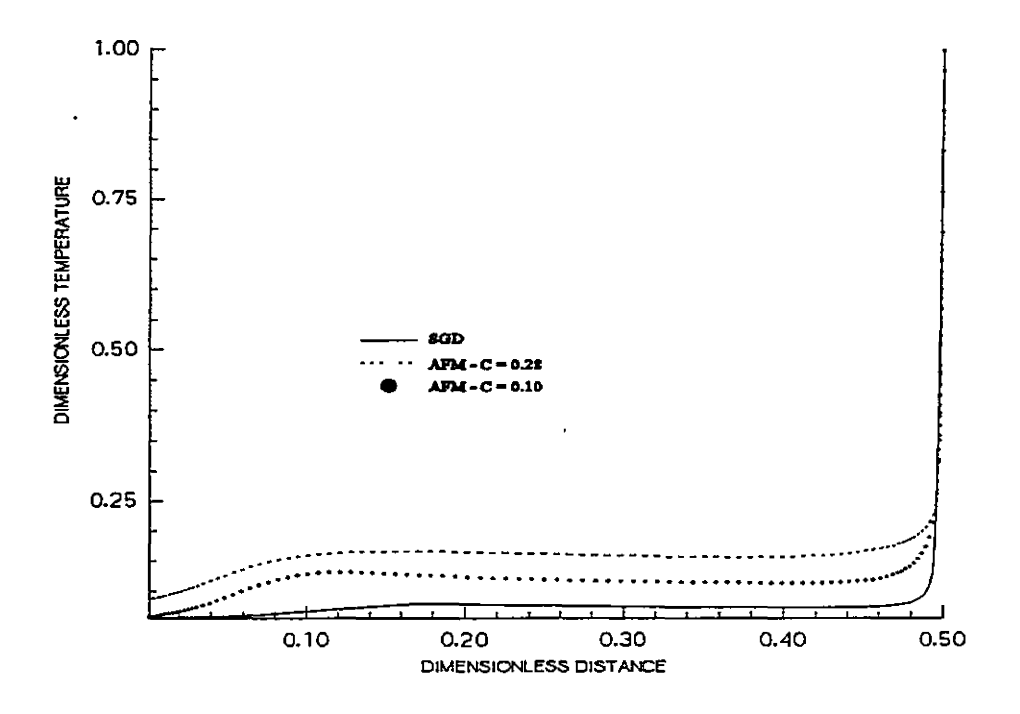


Figure 5.21 - AFM Study (Case 3): Turbulent Heat Flux Profiles (Y = 0.5)



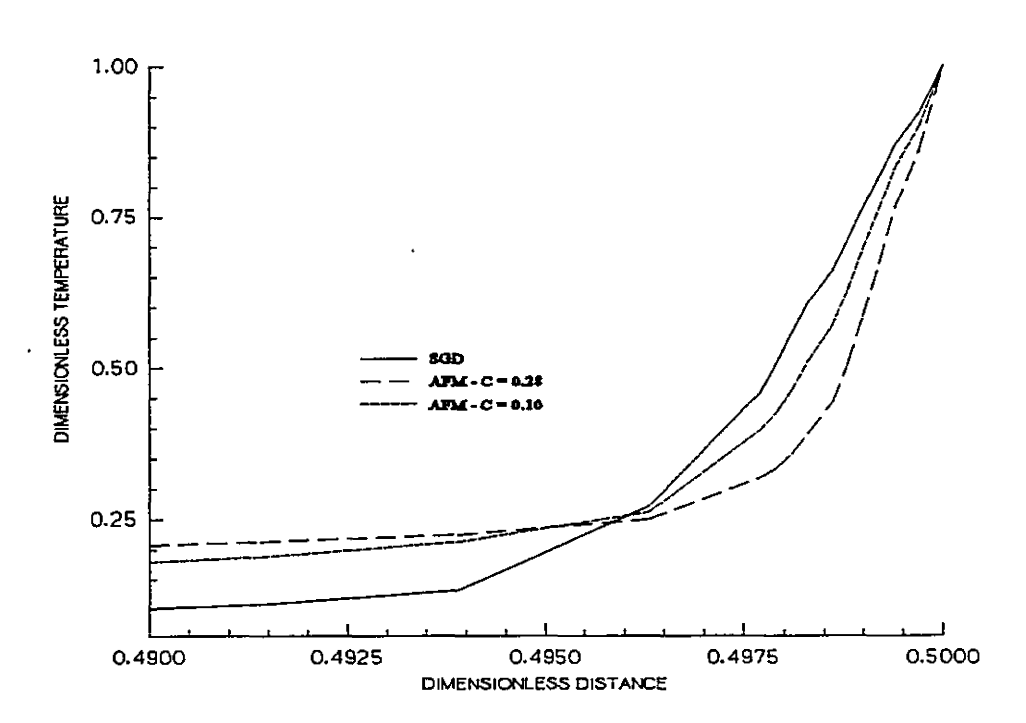


Figure 5.22 - AFM Study (Case 3): Dimensionless Temperature Profiles (Y = 0.5)

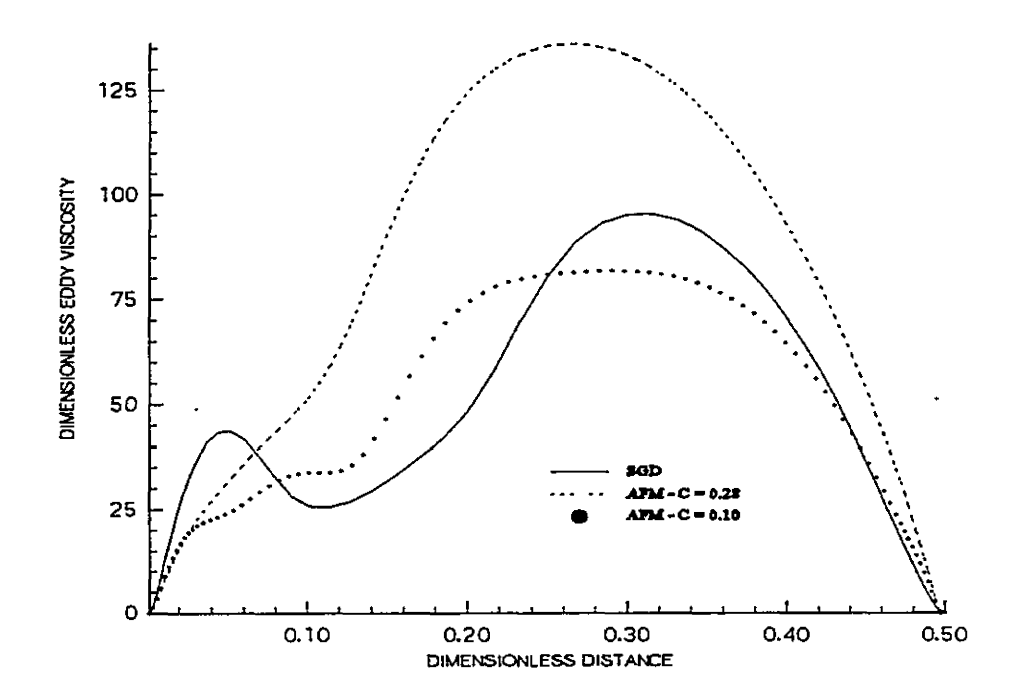


Figure 5.23 - AFM Study (Case 3): Turbulent Viscosity Profiles (Y = 0.5)

Model	Model Constant C	Penetration Depth
SGD	-	0.02290
AFM	0.28	0.01987
AFM	0.10	0.02222

Table 5.6 - AFM Study (Case 3)

Figure 5.21 shows the horizontal and vertical heat flux distributions at the cavity midheight. The AFM model, with C=0.28, predicts levels as much as three times larger than the SGD model for the horizontal component. The vertical SGD component, based only upon the vertical temperature gradient (see Equation 5.3), is essentially non-existent when compared with the AFM predictions.

Temperature profiles at the cavity midheight are shown in Figure 5.22. The increased horizontal heat flux associated with the AFM models leads to steeper temperature gradients or higher heat transfer rates near the heated wall.

Turbulent viscosity profiles are shown in Figure 5.23. When compared to the SGD model, the increase in vertical turbulent heat flux leads to significantly higher levels of turbulent viscosity for C=0.28 while only minor differences arise for C=0.10.

The effect of model constant R was also studied in conjunction with this case. As R is lowered, the fluctuating temperature variance decreases leading to a smaller vertical component of turbulent heat flux. This results in lower turbulent viscosity near the heated wall but only slightly lower heat transfer rates. Significant changes in the mean flow field were not detected.

5.3.3 Case 4

Figure 5.24 shows the predicted streamlines associated with the AFM study for Case 4. Again, much greater buoyant recirculation occurs when the AFM model is employed. This is especially evident when model constant C=0.28.

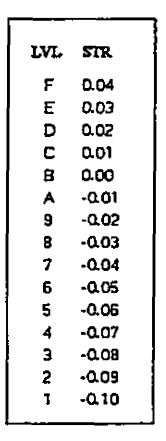
The turbulent heat flux profiles appear in Figure 5.25. As with the previous cases, the heat flux components predicted by the AFM model are significantly greater than those predicted by the SGD model. The difference in predicted values for C = 0.28 and C = 0.10 is not as great as in the other cases. This is probably due to the large difference in the predicted SGD and AFM results.

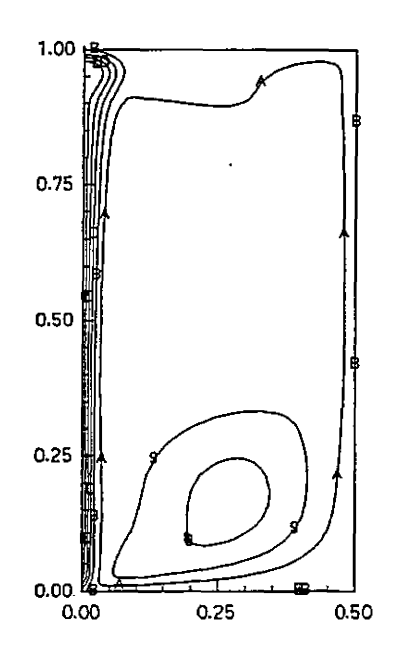
Dimensionless temperature profiles are shown in Figure 5.26. Once again the AFM model, with C=0.28, has the steepest temperature gradient near the wall and, therefore, the highest rate of heat transfer. This high rate of heat transfer accounts for the large buoyant contribution to the flow.

Finally, Figure 5.27 shows turbulent viscosity profiles at the cavity midheight. The viscosity levels are once again significantly higher for the AFM models due to the large increase in vertical turbulent heat flux.

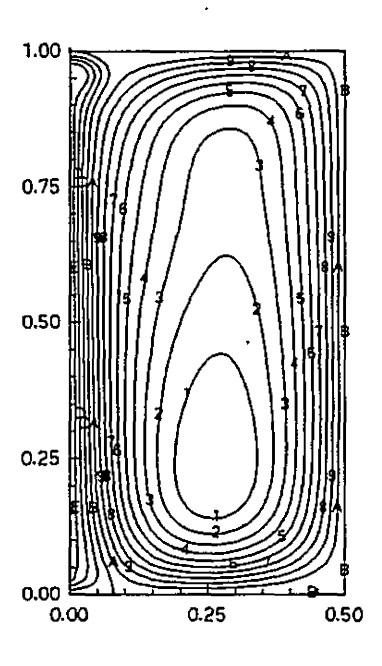
5.3.4 AFM Study Summary

The incorporation of the algebraic heat flux model leads to higher levels of both components of turbulent heat flux. This results in higher heat transfer rates and higher levels of turbulent viscosity for all cases studied. This effect is more pronounced as the

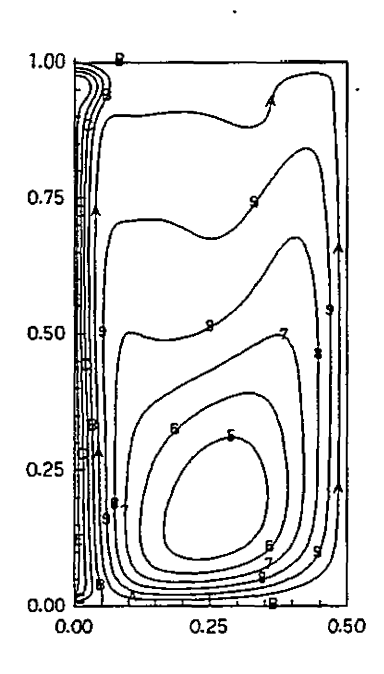




SGD Model

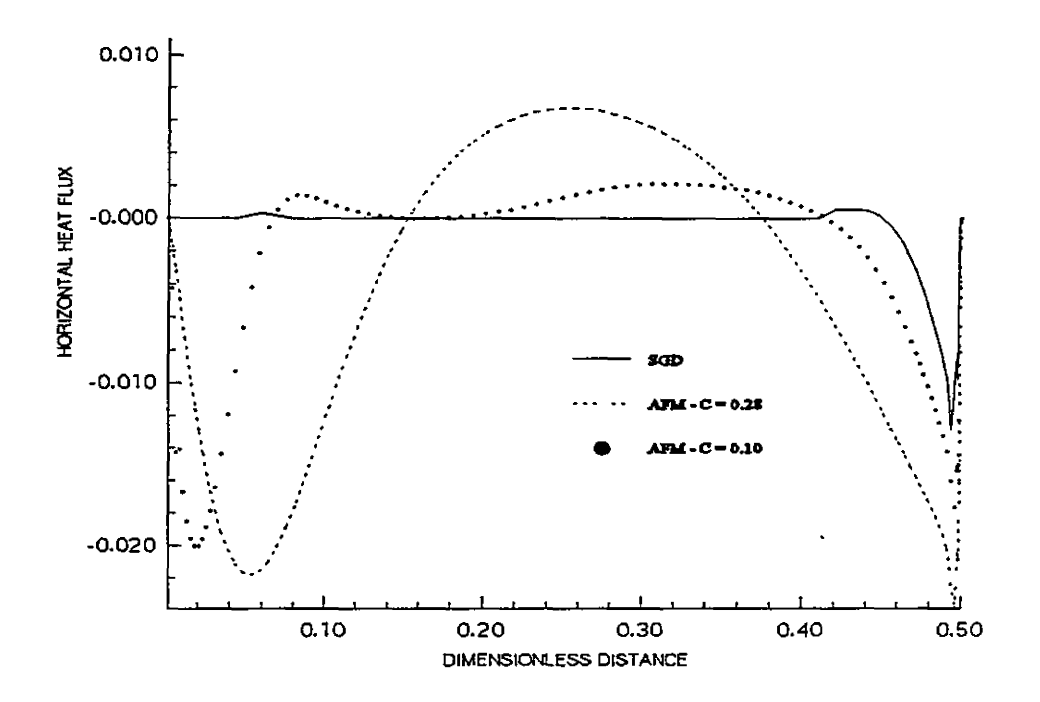


AFM - C = 0.28



AFM - C = 0.10

Figure 5.24 - AFM Study (Case 4): Streamlines



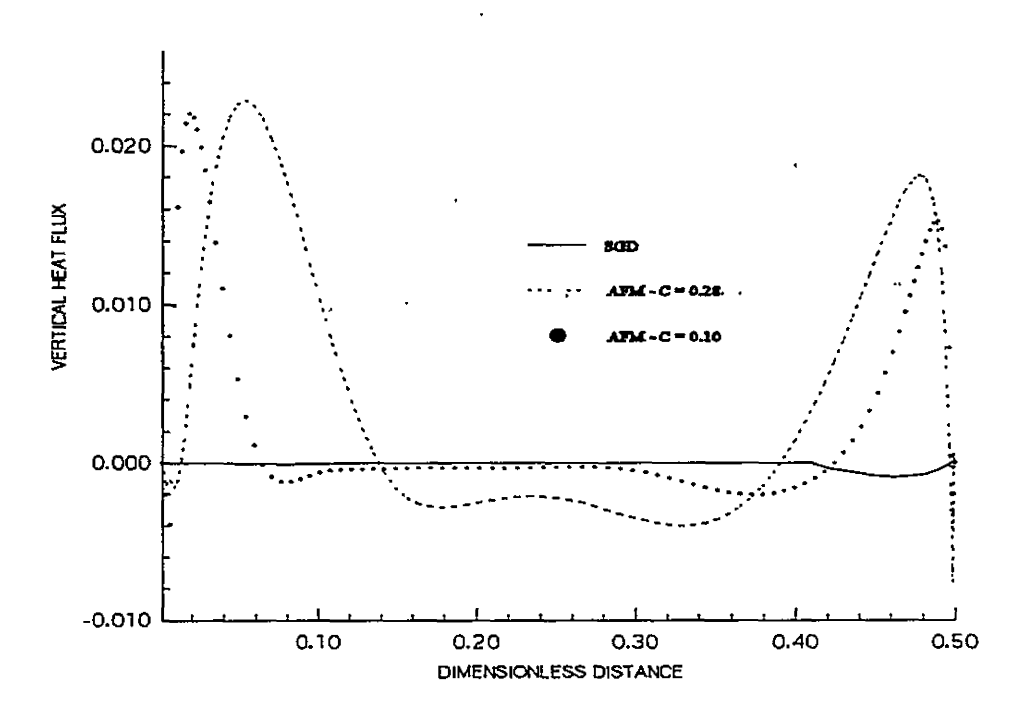
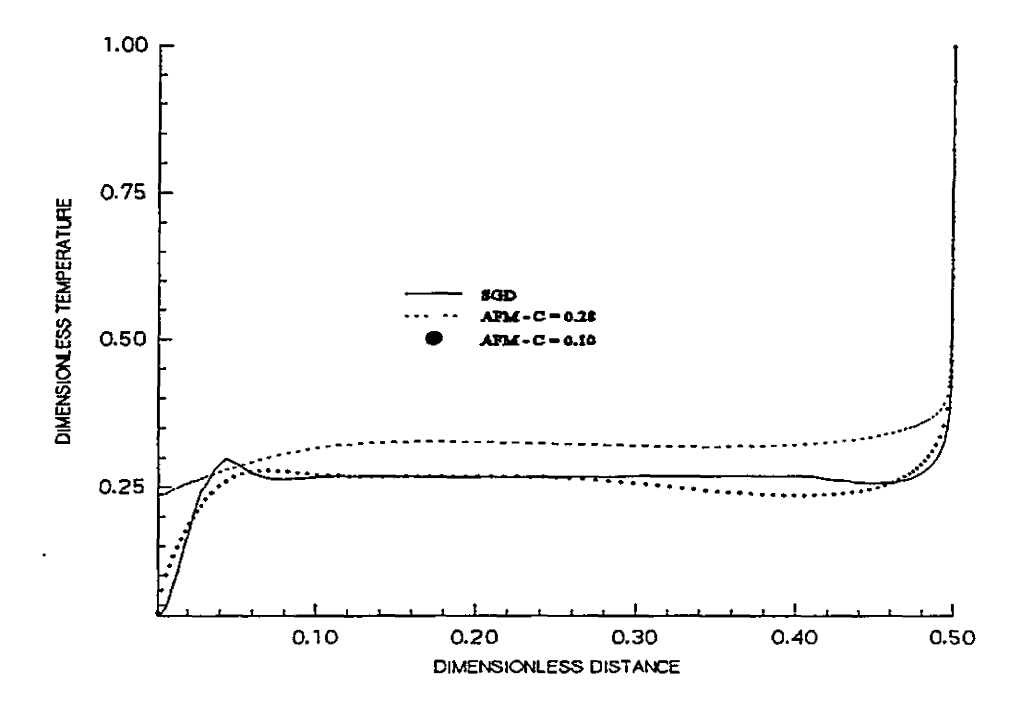


Figure 5.25 - AFM Study (Case 4): Turbulent Heat Flux Profiles (Y=0.5)



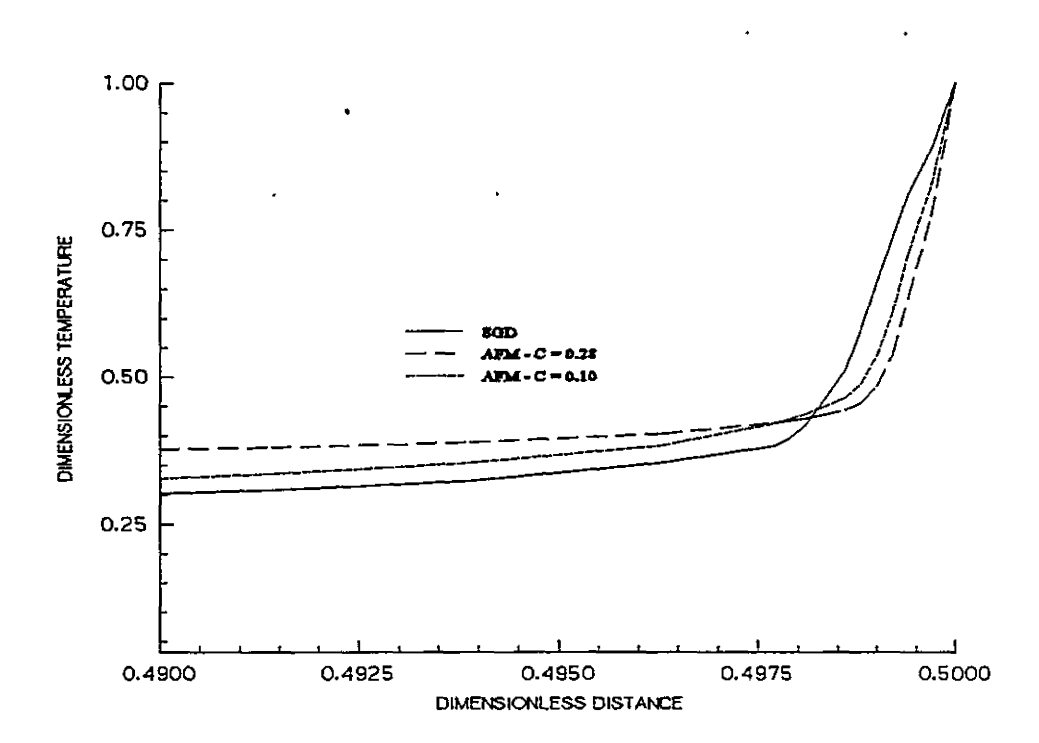


Figure 5.26 - AFM Study (Case 4): Dimensionless Temperature Profile (Y=0.5)

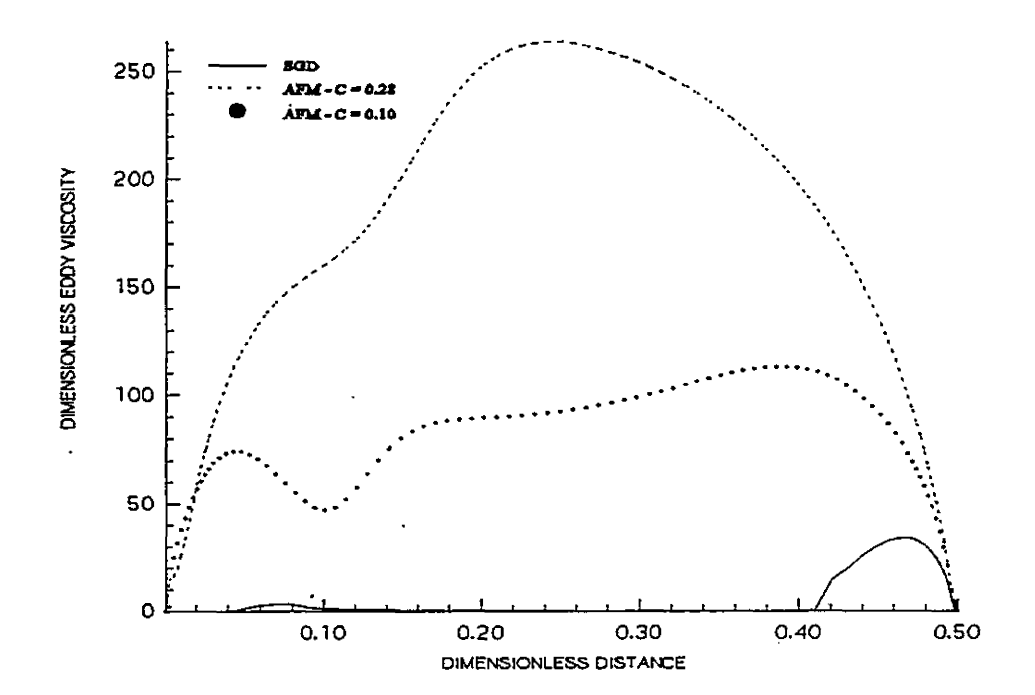


Figure 5.27 - AFM Study (Case 4): Turbulent Viscosity Profiles (Y=0.5)

model constant C is increased.

It appears that the use of an AFM model, by itself, is not the solution to the modelling problem associated with this mixed convection flow field. It is possible that a higher level of turbulent heat flux modelling involving transport equations for fluctuating temperature variance and dissipation of temperature variance could improve the results. However, it is hard to imagine this fine tuning of model accuracy leading to the much lower required levels of heat transfer.

5.4 Final Results

The previous two studies have shown that the predicted results can be significantly affected by two factors, the inlet turbulence conditions and the turbulent heat flux representation. The combination of modified inlet turbulence levels and the AFM model will be presented as a final study. The purpose is to determine the net effect of including both factors and to compare these results to the experimental findings.

The inlet turbulence conditions employed in this study are summarized in Table 5.7. As in all of the previous tests, an inlet turbulence intensity of 10% was specified. The inlet dissipation rate of 0.20 was chosen because this value produced the furthest penetration depth into the cavity for Case 3 in Section 5.2. The inlet turbulent length scale and turbulent viscosity change depending on the Reynolds number for each case.

Case	Red	k*	ε*	v ,*	1*
1	973.	0.015	0.20	1.30	0.0109
2	1283.	0.015	0.20	2.18	0.0139
3	808.	0.015	0.20	0.904	0.00915
4	950.	0.015	0.20	1.24	0.0107

Table 5.7 - Final Results: Inlet Turbulence Conditions

The AFM model, employing the algebraic relationship for fluctuating temperature variance, was used to model the turbulent heat flux. Based on the results of the AFM study, model constant C was set to 0.10 while the time-scale ratio R was set to 0.25.

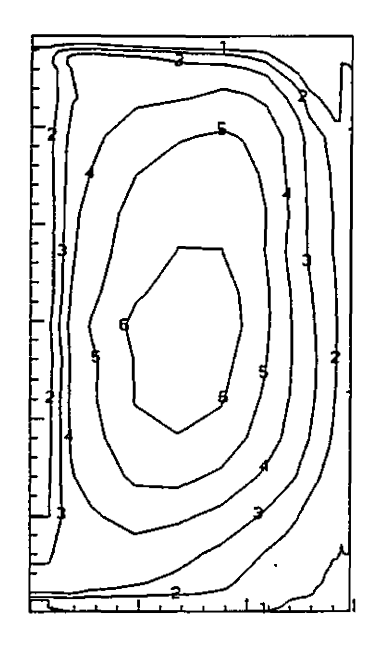
These values represent an attempt to minimize the overprediction of the heat transfer rates.

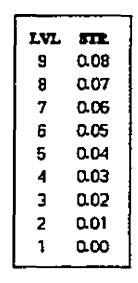
Comparison with the experimental results is based on streamline plots and Nussult number data. Predicted turbulent viscosity contours are also presented.

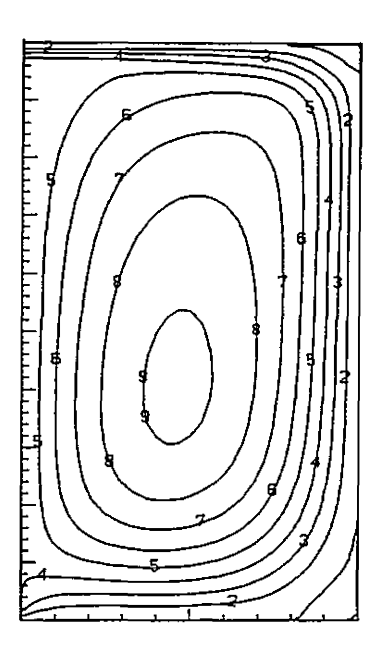
5.4.1 Case 1

Due to the isothermal nature of Case 1, the present results are basically an extension to the inlet viscosity study presented in Section 5.2.1. The earlier findings showed decreased separation height due to increased mean flow momentum as the inlet dissipation rate was decreased.

Predicted streamlines for the current inlet conditions are shown in Figure 5.28 while the predicted turbulent viscosity distribution appears as Figure 5.29. The







Experimental

Predicted

Figure 5.28 - Final Results (Case 1): Streamline Comparison

LVI. VES
O 220.0
N 210.0
M 200.0
L 190.0
K 180.0
J 170.0
I 160.0
H 150.0
G 140.0
F 130.0
E 120.0
D 110.0
C 100.0
B 90.00
A 90.00
9 70.00
8 60.00
7 50.00
6 40.00
5 30.00
4 20.00
3 10.00
2 2.00
1 0.00

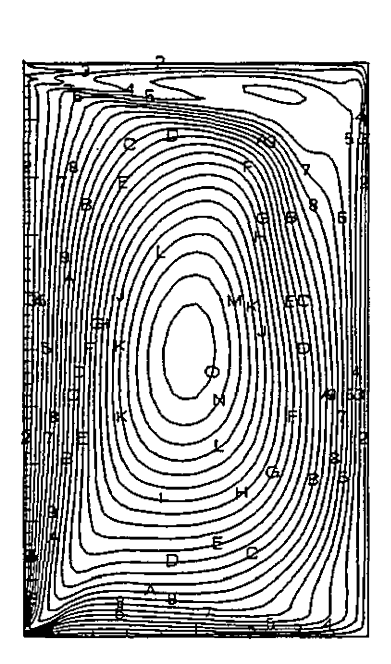


Figure 5.29 - Final Results (Case 1): Predicted Turbulent Viscosity Contours

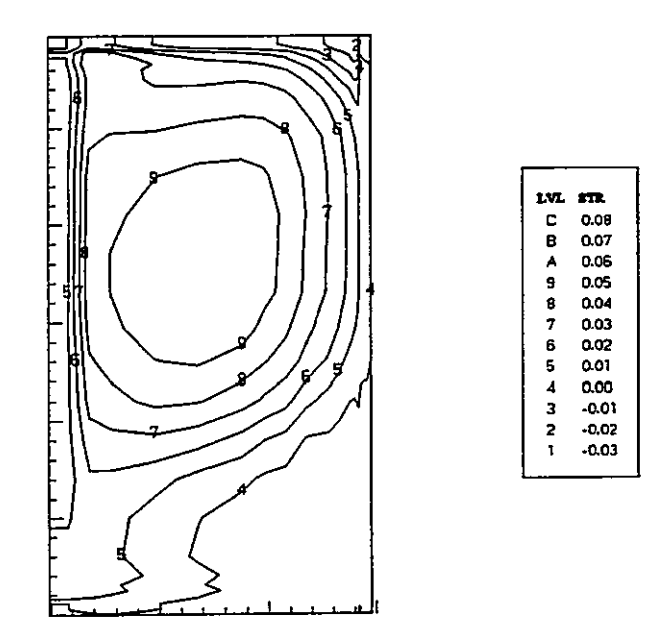
experimental and predicted flow fields are qualitatively similar but the predicted streamline levels are higher in the centre of the cavity due to higher velocities near the right vertical wall. As discussed earlier, the increase in velocity is presumably the result of the increase in mean flow momentum which results from a decrease in the original dissipation rate.

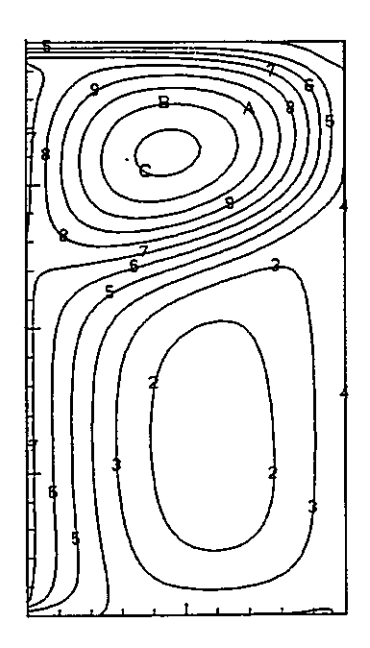
5.4.2 Case 2

The inlet viscosity study for Case 2 showed increased separation height for decreased inlet dissipation rate. This effect was attributed to increased turbulent viscosity throughout the cavity which led to higher rates of heat transfer and, therefore, more buoyancy. It is believed that this increase in the buoyant force overcomes the corresponding increase in momentum resulting in the higher separation location. The application of the AFM model resulted in increased heat transfer rates and stronger buoyant recirculation.

Predicted and experimental streamlines for the present study are compared in Figure 5.30, while the predicted turbulent viscosity distribution is shown in Figure 5.31. It is apparent from the streamline comparison that the predicted ratio of buoyant to inertial forces is still too high. The predicted buoyant cell is much larger and stronger than in the experiment resulting in a predicted separation height which is significantly higher than the experimental location.

Figure 5.32 compares the predicted and experimental Nusselt number distributions along the heated wall. The predicted Nusselt numbers are calculated from the dimensionless temperature gradient at the heated wall while the experimental Nusselt





Experimental

Predicted

Figure 5.30 - Final Results (Case 2): Streamline Comparison

ENG. 188

1 150.0

H 150.0

G 140.0

F 130.0

E 120.0

D 100.0

9 20.00

A 20.00

9 70.00

9 50.00

6 40.00

5 30.00

4 20.00

3 10.00

2 2.00

1 0.00

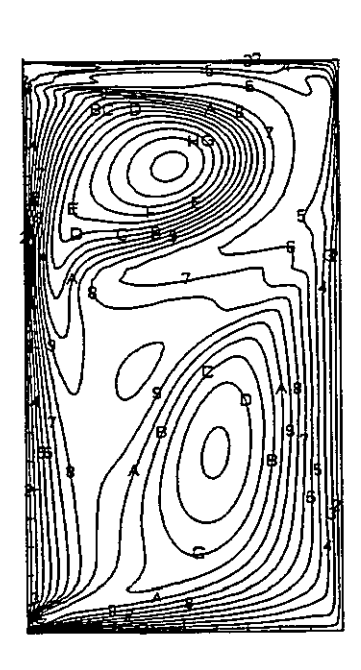


Figure 5.31 - Final Results (Case 2): Predicted Turbulent Viscosity Contours

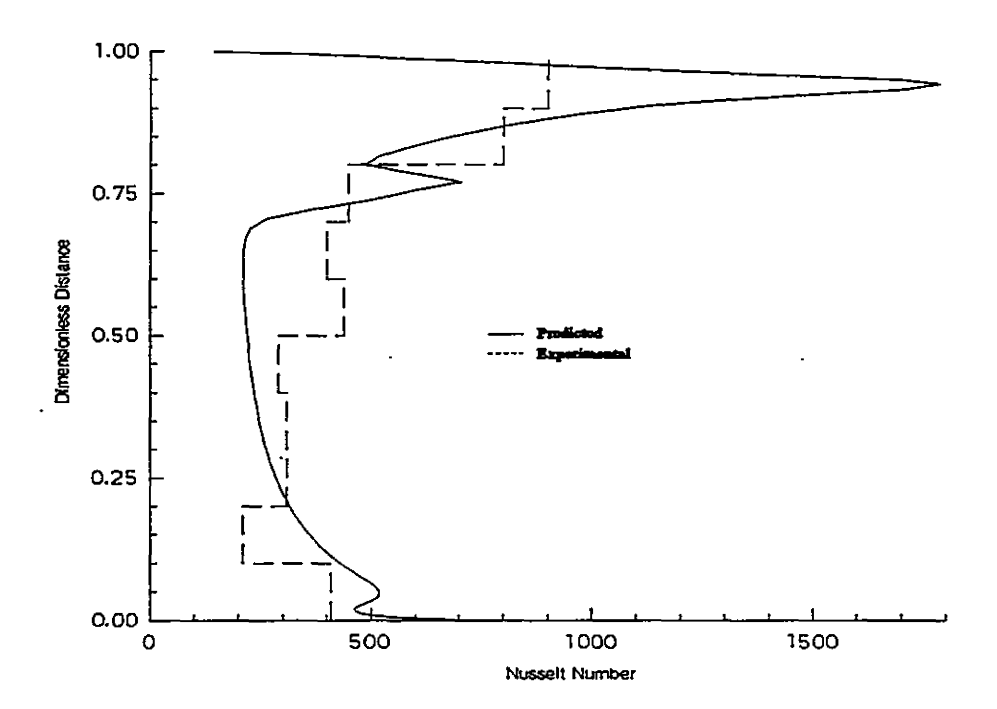


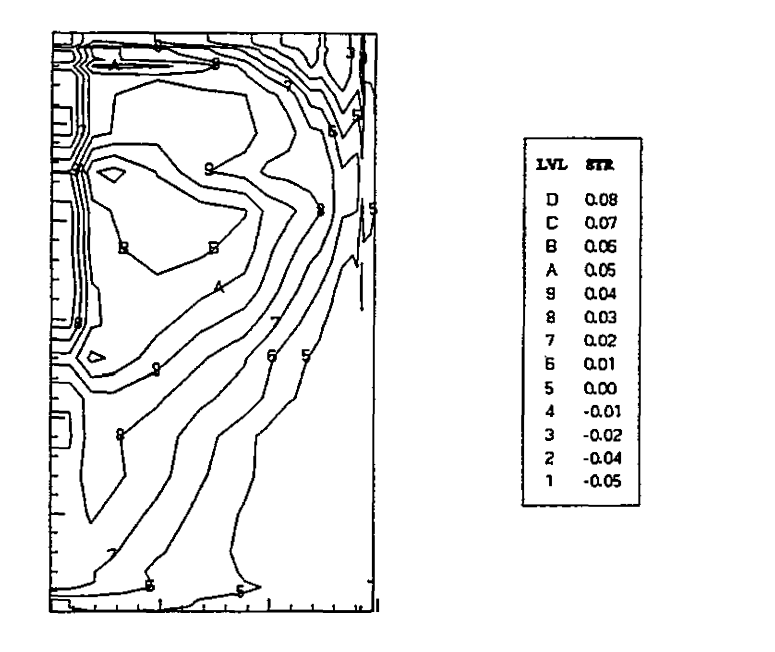
Figure 5.32 - Final Results (Case 2): Nusselt Number Comparison

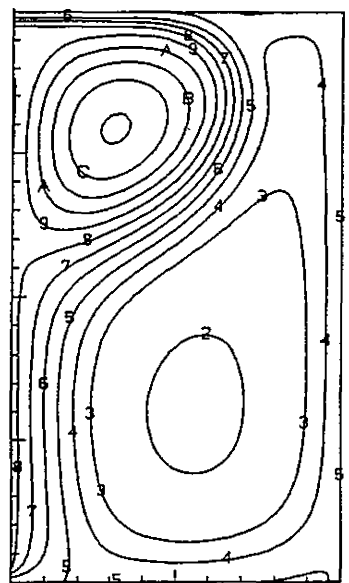
number is calculated from the electrical power input to the heaters [28]. Both profiles show the highest levels of heat transfer occurring above the respective separation points. This is the result of the cold inlet jet impinging on the heated surface. The model predicts higher rates of heat transfer than the experiment within this region. This would indicate lower fluid temperatures in the predicted impingement zone probably due to less interaction with the hotter recirculating buoyant cell. Below the separation location, heat transfer occurs as the fluid rises along the heated wall. The model correctly predicts a decrease in this heat transfer rate as the fluid rises and increases in temperature. The locally minimum heat transfer rate at the separation location is also correctly predicted.

5.4.3 Case 3

The inlet viscosity study for Case 3 showed increased penetration for initial decreases in inlet dissipation rate. Further decreases in the dissipation rate below 0.20 resulted in a regression of the fluid towards the inlet. This is the result of counteracting increases in mean flow momentum and heat transfer due to the modified turbulent viscosity levels. The addition of the AFM model also resulted in higher heat transfer rates. The combination of the two factors is now discussed.

The streamline comparison for Case 3 appears as Figure 5.33 while the predicted turbulent viscosity contours appear in Figure 5.34. The size of the buoyant cell is once again overpredicted drastically. The inlet turbulent viscosity study shows the fluid nearly reaching the heated wall for an inlet dissipation rate of 0.20. The subsequent addition of the AFM model leads to increased heat transfer and, thus, decreased penetration as the





Experimental

Predicted

Figure 5.33 - Final Results (Case 3): Streamline Comparison

EVE VXX

E 120.0
D 110.0
C 100.0
B 90.00
A 80.00
9 70.00
8 50.00
7 50.00
6 40.00
5 30.00
4 20.00
3 10.00
2 2.00
1 0.00

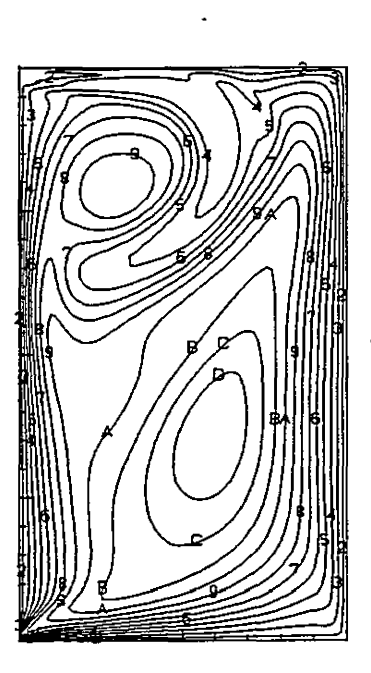


Figure 5.34 - Final Results (Case 3): Predicted Turbulent Viscosity Contours

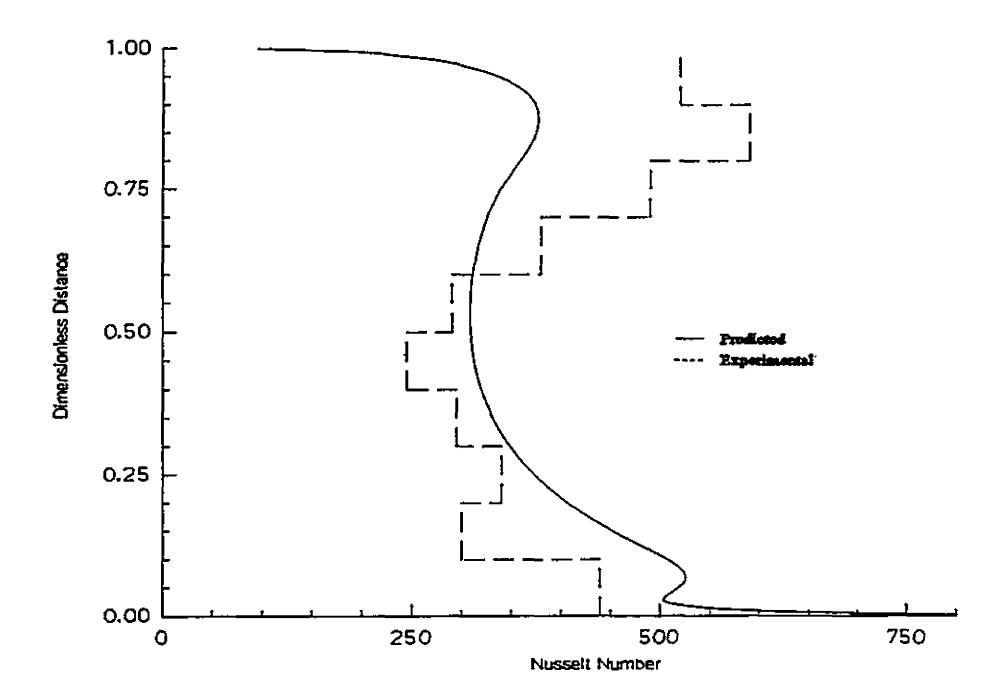


Figure 5.35 - Final Results (Case 3): Nusselt Number Comparison

fluid is driven back from the heated surface. The present results do represent some improvement over previous predictions where higher inlet turbulent viscosity was employed and the flow was nearly entirely dominated by buoyancy.

A comparison between predicted and experimental Nusselt numbers is presented in Figure 5.35. The experimental profile is very similar to that seen in Case 2. The highest heat transfer rates occur above the separation location and the Nusselt number decreases as the fluid rises within the buoyant cell. The predicted profile is similar with a local minimum occurring at the separation point. However, the predicted maximum heat transfer rate does not occur in the upper part of the cavity as in the experiment. This is the result of the cold inlet jet not reaching the heated wall which leads to smaller temperature differences and lower heat transfer rates in this region.

5.4.4 Case 4

The inlet viscosity study for Case 4 showed increased buoyant recirculation due to higher heat transfer rates as the inlet dissipation was decreased. The AFM study found that heat transfer was greatly enhanced when the turbulent heat flux representation was modified.

Streamline results for the combined model are compared with experiment in Figure 5.36. Predicted turbulent viscosity contours are shown in Figure 5.37. The predicted flow field is buoyancy-dominated with one large recirculating cell. These results are consistent with the experimental findings. The decrease in time-scale ratio R from 0.5 to 0.25 has had a noticeable weakening effect on the strength of the buoyant cell (compare

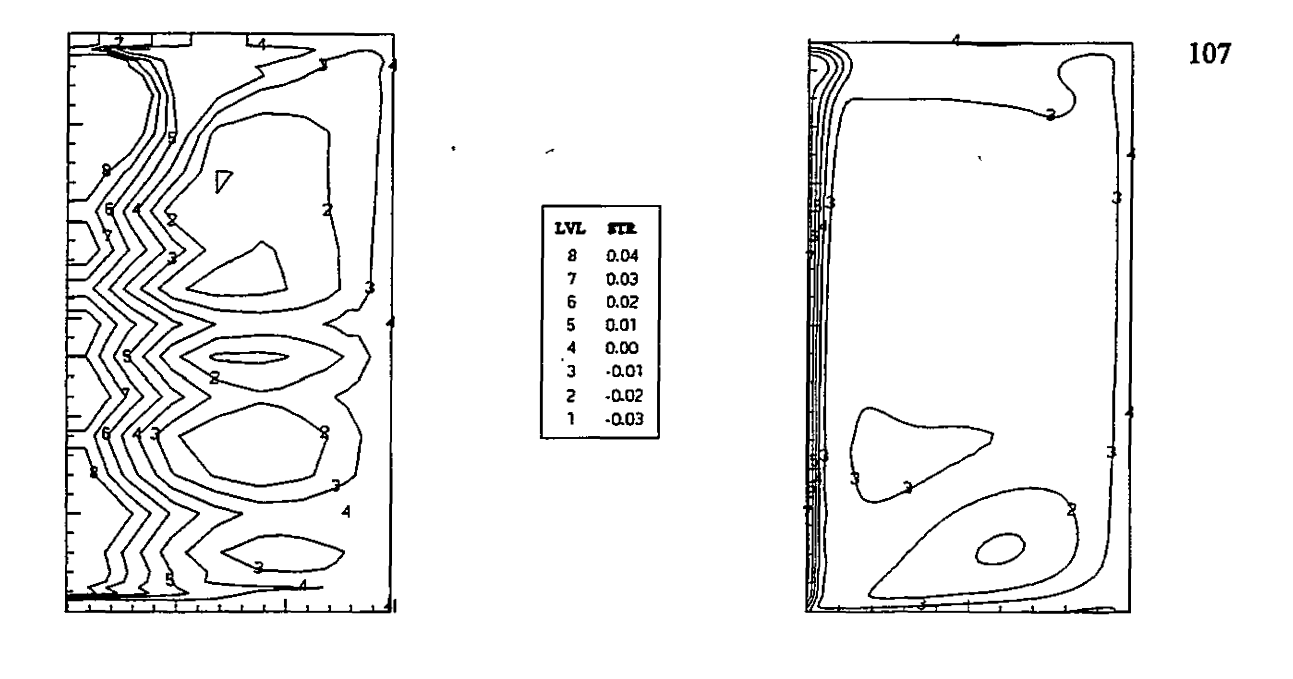
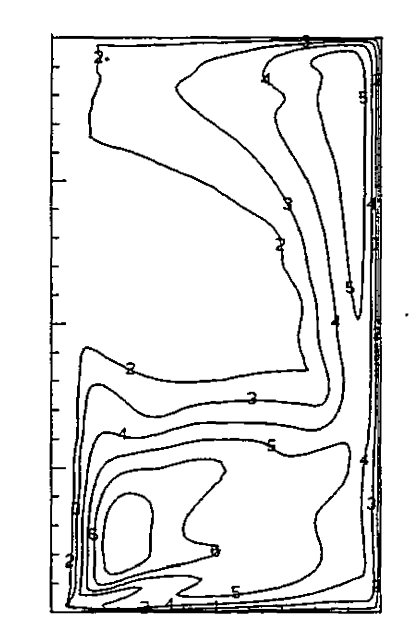


Figure 5.36 - Final Results (Case 4): Streamline Comparison



Predicted

EVL VIS
9 70.00
8 50.00
7 50.00
6 40.00
5 30.00
4 20.00
3 10.00
2 2.00
1 0.00

Experimental

Figure 5.37 - Final Results (Case 4): Predicted Turbulent Viscosity Contours

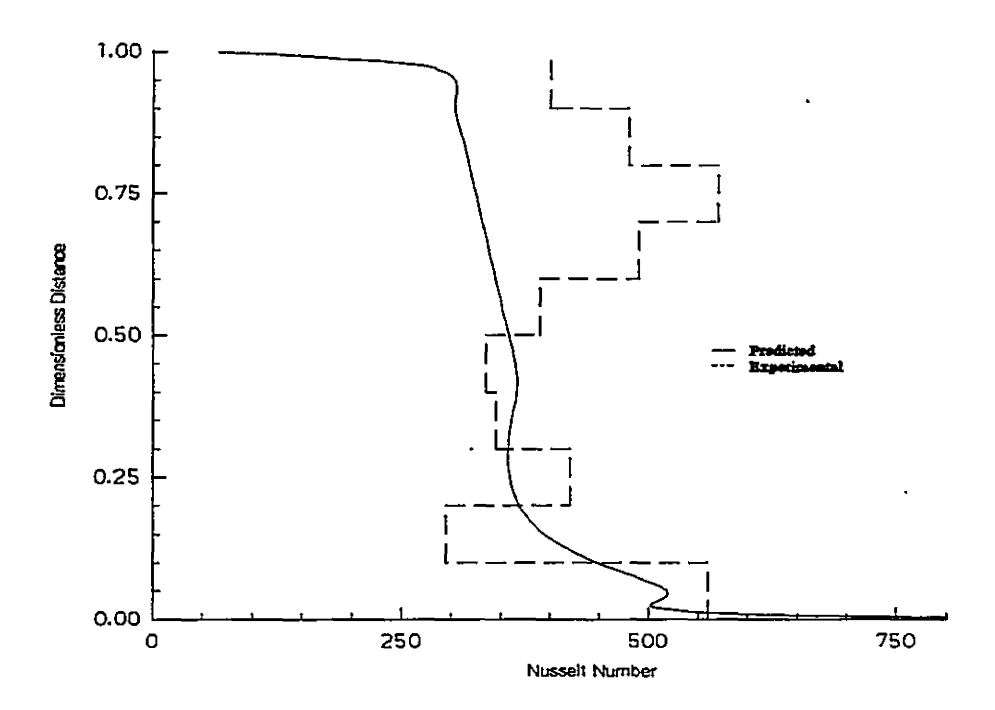


Figure 5.38 - Final Results (Case 4): Nusselt Number Comparison

with Figure 5.24). This would indicate that the fluctuating temperature variance plays an important role in determining the heat transfer rate for this case.

Nussult number profiles are compared in Figure 5.38. The predicted profile shows decreased heat transfer as the fluid rises along the heated wall. The experimental data shows a similar profile in the bottom of the cavity but not in the top half where the heat transfer rate increases as the fluid rises. This could be the result of the separated flow which occurs in the top corner of the cavity.

5.4.5 Final Results Summary

As expected, the combination of modified inlet turbulence conditions and the algebraic flux model still results in flow fields which are representative of overpredicted heat transfer rate and buoyant recirculation. Despite the obvious changes in predicted turbulence parameters, the mean flow results are qualitatively similar to those obtained in previous modelling attempts. However, some improvement is evident in Case 3 where the predicted flow penetrates further into the cavity and therefore agrees more closely with the experiment. This result is encouraging as it was this case which previously presented the most difficulty.

CHAPTER SIX

CONCLUSIONS AND RECOMMENDATIONS

6.1 Purpose

The main focus of this study involved the implementation and testing of an algebraic heat flux representation used in conjunction with a low-Reynolds number k- ε turbulence model. This approach has been employed in the past by researchers hoping to exploit the greater physical accuracy inherent within the AFM model. In most circumstances, the effect on the mean flow has been limited despite very noticeable differences in the predicted turbulent quantities. The purpose here was to determine if the the algebraic flux model would have a significant effect on the predicted flow field when dealing with mixed convection conditions.

As a secondary study, the effect of varying the prescribed inlet turbulence parameters was also examined. Although this topic is rarely discussed within the literature, it is believed that the predicted results are sensitive to the selection of these parameters when certain flows and flow conditions are involved.

6.2 Conclusions

The use of the algebraic heat flux model leads to significant increases in the

magnitudes of both components of turbulent heat flux near the heated surface. Although the larger vertical component results in increased buoyant source terms for both the k and ϵ equations, the combined effect is higher levels of turbulent viscosity. The increased horizontal component and corresponding increase in the horizontal gradient of this quantity leads to enhanced heat transfer rates and stronger buoyant recirculation for all cases.

The sensitivity of the predicted results to two of the model constants associated with the AFM model was also studied. Lowering model constant C directly decreases both components of turbulent heat flux resulting in lower rates of heat transfer and buoyant recirculation. The reduction of time-scale ratio R translates to smaller fluctuating temperature variance and, thus, smaller vertical turbulent heat flux. Although the turbulent viscosity levels decrease slightly, the mean flow is not significantly affected.

The incorporation of the algebraic flux model, on its own, is not the solution to the problem associated with this flow field. The buoyant effects are already overpredicted compared to the available data when the simple gradient diffusion model is employed, and increase in strength when the AFM model is added. However, the use of the AFM model is appropriate and necessary if the predicted turbulent heat flux field is more accurate than that which results when the simpler model is employed. If this is the case, some other factor is responsible for the discrepencies between the predicted results and the experimental findings.

The study of the sensitivity of the predicted results to the choice of inlet turbulence conditions showed that this factor is an important consideration when dealing with this

type of flow. Two effects were noticed as the inlet dissipation rate was decreased while holding the turbulence intensity constant. The first involves an increase in mean flow momentum resulting from a reduction of energy removal from the mean flow through the decreased dissipation rate. This effect was predominant in the isothermal Case 1 and also in Case 3 where the inlet jet was shown to penetrate further into the cavity for a reduced inlet dissipation rate. The second effect involves the increase in heat transfer rates and buoyant recirculation due to increased levels of turbulent viscosity throughout the cavity. This effect was noticed primarily in Case 2, where the separation location increased, and in Case 4, where noticeably stronger buoyant recirculation occurred, as the inlet dissipation rate was decreased. Although both effects are present for all cases involving heat transfer, · it seems that the relevant strength of these effects is dependent on the flow conditions involved. One such factor may be the inlet Reynolds number which is not constant for all of the cases. Case Three is the least turbulent at the inlet and therefore may benefit most from a reduction in dissipation rate. Nevertheless, until the exact turbulence conditions at the inlet are known, prescription of these values and any further discussion must be considered pure speculation.

6.3 Recommendations

To successfully predict this specific flow it is necessary to accurately predict the turbulent heat flux components. Experimental evidence must be secured which can provide the researcher with the confidence that these parameters are being represented accurately. If it is then determined that the turbulent heat flux is not being treated

properly, the extension of the model to a higher order can then be considered.

With respect to the inlet turbulence conditions, experimental data regarding these parameters is also necessary to avoid speculation regarding their specific value. It would also be very useful to conduct further experimental and numerical studies involving higher inlet Reynolds numbers. The fact that the current studies involve relatively low inlet Reynolds numbers may account for some or all of the dependence on these inlet turbulence conditions.

Finally, the suggestion of Hanjaic and Vasic [21] that three-dimensional effects are a major source of inaccuracy when dealing with buoyancy-induced flows must be considered in connection with any further modelling effort.

REFERENCES

- 1. Rodi, W., <u>Turbulence Models and Their Application in Hydraulics</u>, International Association for Hydraulic Research, Netherlands, 1984.
- 2. Rodi, W., "Examples of Turbulence Models for Incompressible Flows", AIAA, Vol. 20, pp. 872-879, 1981.
- 3. Launder, B.E., and Spalding, D.B., "Lectures in Mathematical Modelling of Turbulence", Academic Press, 1972.
- 4. Jones, W.P., and Launder, B.E., "The Prediction of Laminarization with a Two-Equation Model of Turbulence", Int. J. of Fluid Mechanics, Vol. 15, pp. 301-314, 1972.
- Launder, B.E., and Sharma, B.I., "Application of the Energy-Dissipation Model of Turbulence to the Calculation of Flow Near a Spinning Disc", Letters in Heat and Mass Transfer, Vol. 1, pp. 131-138, 1974.
- 6. Lam, C.K.G., and Bremhorst, K.A., "Modified Form of the k-ε Model for Predicting Wall Turbulence", J. Fluids Engineering, Vol. 103, pp. 456-460, 1981.
- 7. Patel, V.C., Rodi, W., and Scheurer, G., "Turbulence Models for Near-Wall and Low Reynolds Number Flows: A Review", AIAA, Vol. 23, pp. 1308-1319, 1984.
- 8. Rodi, W., Turbulent Buoyant Jets and Plumes, Pergammon Press, 1982.
- Plumb, O.A., and Kennedy, L.A., "Application of a k-E Turbulence Model to Natural Convection From a Vertical Surface", J. Heat Transfer, Vol. 99, pp. 79-85, 1977.
- Markatos, N.C., and Pericleous, K.A., "Laminar and Turbulent Natural Convection in an Enclosed Cavity", Int. J. Heat Mass Transfer, Vol. 27, pp. 755-772, 1984.

- 11. Humphrey, J.A.C., and To, W.M., "Numerical Simulation of Buoyant Turbulent Flow II. Free and Mixed Convection in a Heated Cavity", Int. J. Heat Mass Transfer, Vol. 29, pp. 593-610, 1986.
- 12. Ince, N.Z., and Launder, B.E., "On the Computation of Buoyancy Driven Turbulent Flows in Rectangular Enclosures", Int. J. Heat and Fluid Flow, Vol. 10, pp. 110-117, 1989.
- 13. Yap, C. "Turbulent Heat and Momentum Transfer in Recirculating and Impinging Flows", Ph.D. Thesis, University of Manchester, U.K., 1987.
- 14. Henkes, R.A.W.M., Van der Vlugt, F.F., and Hoogendoorn, C.J., "Natural-Convection Flow in a Square Cavity Calculated with Low-Reynolds Number Turbulence Models", Int. J. Heat Mass Transfer, Vol. 34, pp. 377-388, 1991.
- Davidson, L., "Calculation of the Turbulent Buoyancy Driven Flow in a Rectangular Cavity Using an Efficient Solver and Two Different Low-Reynolds Number k-ε Models", Numer. Heat Transfer, Part A, Vol. 18, pp. 129-147, 1990.
- 16. Cheesewright, R., King, K.J., and Ziai, S., "Experimental Data for the Validation of Computer Codes for the Prediction of Two-Dimensional Buoyant Cavity Flows", Significant Questions in Buoyancy Affected Enclosure or Cavity Flows, Vol. HTD60, pp. 75-81, 1986.
- 17. To, W.M., and Humphrey, J.A.C., "Numerical Simulation of Buoyant Turbulent Flow I. Free Convection Along a Heated, Vertical, Flat Plate", Int. J. Heat Mass Transfer, Vol. 29, pp. 573-592, 1986.
- 18. Silva, D.J., and Emery, A.F., "A Preliminary Comparison of the k-\varepsilon and Algebraic Stress Models for Turbulent Heat Transfer in a Square Enclosure", Proc. of the National Heat Transfer Conference, Vol. 110, pp. 193-200, 1989.
- Davidson, L., "Second-order Corrections of the k-ε Model to Account for Nonisotropic Effects Due to Buoyancy", Int. J. Heat Mass Transfer, Vol. 33, pp. 2599-2608, 1990.
- 20. Shabbir, A., and Taulbee, D.B., "Evaluation of Turbulence Models for Predicting Buoyant Flows", J. Heat Transfer, Vol. 112, pp. 945-951, 1990.
- 21. Hanjalic, K., and Vasic, S., "Computation of Turbulent Natural Convection in Rectangular Enclosures with an Algebraic Flux Model", Int.J. Heat Mass Transfer, Vol. 36, pp. 3603-3624, 1993.

- 22. Hanjalic, K., "Achievements and Limitations in Modelling and Computation of Buoyant Turbulent Flows and Heat Transfer", Special Keynote Lecture, 10th International Heat Transfer Conference, Brighton, U.K., 1994.
- 23. Murakami, S., Kato, S., and Ooka, R., "Comparison of Numerical Prediction of Horizontal Nonisothermal Jet in a Room with Three Turbulence Models k-ε, EVM, ASM, and DSM", ASHRAE Transactions, pp. 697-704, 1994.
- Kato, S., and Murakami, S., and Kondo, Y., "Numerical Simulation of Three-Dimensional Room Airflow With and Without Buoyancy by Means of ASM", ASHRAE Transactions, pp. 238-255, 1994.
- Kenjeres, S., and Hanjalic, K., "Prediction of Turbulent Thermal Convection in Concentric and Eccentric Horizontal Annuli", Int. J. Heat and Fluid Flow, Vol. 16, pp. 429-439, 1995.
- 26. So, R.M.C., and Sommer, T.P., "An Explicit Algebraic Heat-Flux Model for the Temperature Field", Int. J. Heat Mass Transfer, Vol. 39, pp. 455-465, 1996.
- 27. Sommer, T.P., and So, R.M.C., "On the Modeling of Homogeneous Turbulence in a Stably Stratified Flow", Phys. Fluids, Vol. 7, pp. 2766-2777, 1995.
- 28. Numberg, G., "An Investigation of Mixed Convection in Enclosures", Ph.D. Thesis, McMaster University, Hamilton, Canada, 1994.
- 29. Patankar, S.V., <u>Numerical Heat Transfer and Fluid Flow</u>, Hemisphere Publishing Corp., U.S.A., 1980.
- 30. Tennekes, H., and Lumley, J.L., <u>A First Course in Turbulence</u>, MIT Press, Cambridge, MA, 1972.
- 31. Gebhart, B., Jaluria, Y., Mahajan, R.L., and Sammakia, B., <u>Buoyancy Induced</u>
 <u>Flows and Transport</u>, Hemisphere Publishing Corp., New York, NY, 1988.